UNIVERSITY OF PRETORIA

DEPARTMENT OF CIVIL ENGINEERING

OPTIMISED MIX COMPOSITION AND STRUCTURAL BEHAVIOUR OF ULTRA-HIGH-PERFORMANCE FIBRE REINFORCED CONCRETE

M. WEYERS

OPTIMISED MIX COMPOSITION AND STRUCTURAL BEHAVIOUR OF ULTRA-HIGH-PERFORMANCE FIBRE REINFORCED CONCRETE

MEGAN WEYERS

A dissertation submitted in partial fulfilment of the requirements for the degree of

MASTER OF ENGINEERING (STRUCTURAL ENGINEERING)

in the

FACULTY OF ENGINEERING

UNIVERSITY OF PRETORIA

2020

ABSTRACT

OPTIMISED MIX COMPOSITION AND STRUCTURAL BEHAVIOUR OF ULTRA-HIGH-PERFORMANCE FIBRE REINFORCED CONCRETE

M. WEYERS

Supervisor:	Professor E.P. Kearsley
Department:	Civil Engineering
University:	University of Pretoria
Degree:	Master of Engineering (Structural Engineering)

The overall objective of this study was to develop an optimised Ultra-High-Performance Concrete (UHPC) matrix based on the modified Andreasen and Andersen optimum particle packing model by using available South African materials. The focus of this study was to determine the optimum combined fibre and superplasticiser content for UHPC by using a response surface design.

The UHPC was appropriately designed, produced and tested. Various changes in mechanical properties resulting from different combinations of steel fibre and superplasticiser contents was investigated. The flowability, density and mechanical properties of the designed UHPC were measured and analysed. Both the fibre and superplasticiser content play a significant role in the flowability of the fresh concrete. The addition of fibres significantly improved the strength of the concrete. The results show that the superplasticiser content can be increased if a more workable mix is required without decreasing the strength significantly. The statistical analysis of the response surface methodology confirms that the designed models can be used to navigate the design space defined by the Central Composite Design. The optimum combined fibre and superplasticiser content depend on the required mechanical properties and cost. Using the modified Andreasen and Andersen particle packing model and surface response design methodology, it is possible to efficiently produce a dense Ultra-High-Performance Fibre

Reinforced Concrete (UHPFRC) with a relatively low binder amount, low fibre content and good workability.

The effect of heat curing on the mechanical properties was investigated. It was concluded that heat curing is not recommended when considering the long-term strength development. The estimated strength development of concrete obtained by using the *fib* Model Code 2010 (2013) does not incorporate the detrimental effect of high curing temperatures on long-term strength and therefore overestimate the long-term strengths. The strength estimates for both early and long-term ages can be improved by considering this effect in the strength development functions obtained from *fib* Model Code 2010 (2013).

The effect of specimen size on the compressive and flexural tensile strength of UHPFRC members were established. It was found that the specimen size has a significant effect on the measured cube compressive strength. Smaller beam specimens showed higher ductility compared to those of the larger beam specimens. The crack width decreased as the beam's depth decreased. A lower variability was experienced in the beams with limited depth (< 45 mm). Further testing is required to determine whether a span-to-depth ratio of 10 would yield optimum results.

The utilisation of by-products, such as undensified silica fume and fly ash, as cement replacement materials makes UHPFRC sustainable, leading to a reduced life-cycle cost. The calculated Embodied Energy per unit strength (EE/unit strength) and Embodied Carbon per unit strength (EC/unit strength) values for the UHPFRC mixture yield lower values compared to that of the 30 MPa concrete mixture, indicating that UHPFRC can be used to reduce the environmental footprint of the concrete industry.

The inverse analysis method used was successful in providing an improved simplified stress-strain response for the UHPFRC. The analysis provided valuable information into the stress-strain, load-deflection and moment-curvature responses of the UHPFRC. Standard material test results were used to theoretically calculate moment-curvature responses and were then compared to the experimental results obtained.

The study demonstrated that it is possible to efficiently produce a dense and workable UHPFRC with relatively low binder amount and low fibre content. This can result in more cost-effective UHPFRC, thus improving the practical application thereof.

DECLARATION

I, the undersigned, do hereby declare that:

- I understand what plagiarism is and I am aware of the University's policy in this regard.
- The work contained in this project report is my own original work.
- I did not refer to work of current or previous students, lecture notes, handbooks or any other study material without proper referencing.
- I have not allowed anyone to copy any part of my project report.
- I have not previously, in its entirety or in part, submitted this project report at any university for a degree.

MWeyers

Megan Weyers

14118565

February 2020

ACKNOWLEDGEMENT

I wish to express my sincere gratitude to my supervisor, Prof Elsabe Kearsley for her advice, guidance, and support throughout this study. Your inputs were a major factor in reaching the completion of this research. Thank you for your time and all the opportunities provided throughout these past two years.

I also wish to express my gratitude to Mr Derek Mostert for his advice, help and assistance with the casting and testing of concrete samples.

I would also like to thank the following laboratory staff at the University of Pretoria:

i) Mr Johan Scholtz for his advice and logical aid in the concrete laboratory,

ii) Mr Jaco Botha for his preparation of the testing floor and help during testing of concrete samples,

iii) Mr Rikus Kock for his technical help,

iv) Mrs Vanessa Doman for her help with the analysis of PSD and the determination of RD of the various materials,

v) The concrete laboratory staff: Mr Jonas Selwadi, Mr Richard Nchabeleng, Mr Samuel Nkadimeng and Mr Daniel Motloung, without whom this work would not have been possible. Thank you for your assistance in the preparation, manufacturing and casting of all the concrete samples,

vi) The Microscopy and Microanalysis laboratory staff: Mrs Erna van Wilpe and Miss Charity Maepa for their expert assistance with the SEM.

Finally, to my family, thank you for your endless encouragement, reassurance and support during these past two years.

TABLE OF CONTENTS

LIST OF TABLES

PAGE

LIST OF FIGURES

PAGE

LIST OF SYMBOLS

Symbol	Description	Units
ARD	Absolute relative deviation	%
b	Sample width	mm
CoV	Coefficient of Variance	%
D	Particle size	µm
D_{max}	The maximum particle size	µm
D_{min}	The minimum particle size	µm
d	Sample diameter	mm
d_0	Base diameter of the cone	mm
d_1	Maximum dimension of the concrete spread, parallel to one edge of the table	mm
d_2	Maximum dimension of the concrete spread, parallel to the other edge of the table	mm
E	Modulus of elasticity	GPa
f	Flow value	mm
f_b	Flexural tensile strength	MPa
f_{cu}	Characteristic cube strength	MPa
f_{cm}	Mean compressive strength	MPa
$f_{cm}(t)$	Mean compressive strength in MPa at an age of 28 days	MPa
f_s	Splitting tensile strength	MPa
f_{sk}	Factor for shear	
h	Sample depth or height	mm

I	Second moment of area	mm^4
k	Number factors	mm
L	Sample length	mm
L_{span}	Span length	mm
M_L	Moment due to a actual load	Nmm
M_u	Moment due to a unit load	Nmm
n	Number of points between D_{min} and D_{max}	
P	Failure load	N
$P(D)$	A fraction of the total solids being smaller than size D	
q	Distribution modulus	
R^2	Coefficient of determination	
SD	Standard Deviation	
S	A coefficient which depends on the strength class of cement	
T	Temperature	°C
T_b	Flexural toughness	N/m
TF	Flexural toughness factor	N/mm^2
$T(\Delta t_i)$	Mean temperature during the time period Δt_i	°C
t	Concrete age	Days
t_T	Temperature-adjusted concrete age	Days
V_u	Shear force due to a unit load	N
V_L	Shear force due to an actual load	N
Δt_i	Number of days where a temperature T prevails	Days
$\beta_{cc}(t)$	A function to describe the strength development with time	
$\beta_0, \beta_i, \beta_{ii}, \beta_{ij}$	Regression coefficients	

γ	Shear strain	
δ	Total deflection	mm
δ_{cr}	Displacement corresponding to the matrix strength	mm
δ_f	Maximum displacement that causes pull-out of the fibres	mm
δ_M	Deflection due to moment	mm
δ_0	Value when the separation of the matrix specimen into two halves occurs	mm
δ_{pc}	Displacement corresponding to the post-peak strength	mm
δ_{tb}	Deflection of 1/150 of span	mm
δ_V	Deflection due to shear	mm
ε	Random error	
ε_{co}	Maximum linear elastic strain	
ε_{cu}	Ultimate compressive strain	
ε_{to}	Cracking elastic strain	
ε_{t1}	Residual strain	
ε_{tu}	Ultimate tensile strain	
ξ_p	Relative slump	
σ_{cr}	First peak stress	MPa
σ_{cu}	Maximum linear elastic stress	MPa
σ_{pr}	Post-peak strength	MPa
σ_{to}	Cracking strength	MPa
σ_{t1}	Residual stress	MPa
φ	Curvature	1/m

LIST OF ABBREVIATIONS

Abbreviation	Description
AD	Adequate Precision
ANOVA	Analysis of variance
C	Cement
CCD	Central Composite Design
CoV	Coefficient of Variance
CPM	Compressible Packing Model
D-A	Dolomite Stone
D-S	Dolomite Sand
DEF	Delayed Ettringite Formation
EC	Embodied Carbon
EE	Embodied Energy
FA	Fly Ash
LOP	Limit of Proportionality
LPDM	Linear Packing Density Model
LVDT	Linear Variable Differential Transformer
MOR	Modulus of Rupture
NSC	Normal Strength Concrete
PSD	Particle Size Distribution
RD	Relative Density
RSM	Response Surface Methodology

RSS	Residual Sum of Squares
SD	Standard Deviation
SEM	Scanning Electron Microscope
SSF	Short Straight Fibres
SP	Superplasticiser
S-S	Silica Sand
SSM	Solid Suspension Model
UHPC	Ultra-High-Performance Concrete
UHPFRC	Ultra-High-Performance Fibre Reinforced Concrete
USF	Undensified Silica Fume
W	Water
w/b	water-to-binder ratio
w/c	water-to-cement ratio
XRD	X-Ray Diffraction
XRF	X-Ray Fluorescence

1 INTRODUCTION

1.1 BACKGROUND

Ultra-High-Performance Concrete (UHPC) is described as concrete with a minimum compressive strength of 150 MPa (Habel et al., 2008). When fibres are added, the term Ultra-High-Performance Fibre Reinforced Concrete (UHPFRC) is used. Abbas et al. (2016) state that UHPC is a construction material that demonstrates enhanced durability and mechanical properties. Economic construction can be promoted through decreasing the cross-section dimensions of members, thereby reducing materials used and lowering the installation costs as well as reducing the maintenance and increasing the lifespan (Richard & Cheyrezy, 1995; Tang, 2004; Wille & Boisvert-Cotulio, 2015).

Sustainable development is currently a critical global issue and construction industries need to save energy and lower the environmental impact. The use of UHPFRC in the construction industry has been limited due to its high initial material cost, perceived CO_2 emission and energy consumption (Habert et al., 2013; Wille & Boisvert-Cotulio, 2015). Meng et al. (2017) and Yu et al. (2014) state that supplementary cementitious materials can be used to reduce the cost and environmental impact of UHPFRC. These materials include silica fume, ground granulated blast-furnace slag and fly ash. According to Yu et al. (2015b), the published mix compositions for UHPFRC are mostly given without any detailed explanation. To date, questions regarding optimising the concrete mix composition for UHPFRC and using binders efficiently remain unanswered.

An optimal particle packing of granular ingredients of concrete is the key to a durable and sustainable concrete (Hüsken, 2010). A reduction in the cement content should be possible by using filler materials. These filler materials must be included in the entire grading of the mix together with the binding materials, in order to achieve the densest possible packing. The optimised particle packing of granular ingredients in concrete can result in a denser granular structure, with enhanced mechanical properties and improved porosity.

Besides the design of the concrete matrix, the efficient use of steel fibres is also crucial (Kim et al., 2011). The steel fibres are added to the mix, without considering the efficiency of the amount of fibres used. Kahanji et al. (2017) recommend reducing the unit cost of UHPFRC by reducing the steel fibre content. According to Graybeal (2007), tensile properties are greatly enhanced by the addition of steel fibres; however, the steel fibres have a significant effect on the flowability of the fresh concrete. According to Abbas et al. (2016), the effective addition of superplasticiser can improve the workability of UHPFRC. An optimum fibre content is required to balance the workability and mechanical performance (Wille et al., 2011a; Meng et al., 2017). According to Li et al. (2016), it is necessary to investigate the effect of steel fibres on the flowability of UHPC before their utilisation.

Consequently, the objectives of this study were to efficiently develop an optimised concrete matrix based on the modified Andreasen and Andersen optimum particle packing model (Funk & Dinger, 1980) by using available South African materials. The focus of this study was to determine the optimum combined fibre and superplasticiser content for UHPC by using a response surface design, after which a material model was developed that can be used to design UHPFRC structural members. As part of this project, the actual structural behaviour of experimental UHPC beams was compared to numerically predicted behaviour by using the developed material model.

1.2 PROBLEM STATEMENT

Cement production represents 7 % of the total anthropogenic CO_2 emissions (UNSTATS, 2010). One of the key sustainability challenges for the next decade is to design and produce concrete with less clinker and lower CO_2 emissions than traditional concrete, while providing the same durability (Yu et al., 2014). By applying the modified Andreasen and Andersen particle packing model, it is possible to produce a dense and homogeneous skeleton of UHPFRC with a relatively low binder content. Due to the denser granular structure, the porosity would reduce while the mechanical properties of the final product should be improved. Response Surface Methodology (RSM) was used to optimise the combined fibre and superplasticiser content for UHPC, while achieving good workability together with high strength and minimised cost.

There is a need to determine an optimised mix design for UHPFRC by using optimum particle packing for South African materials. By using this optimised mix design, a material model can be developed that can be used to design UHPFRC structural members. As part of this project, the actual structural behaviour of experimental UHPC beams was compared to numerically predicted behaviour by using the developed material model.

1.3 OBJECTIVES OF THE STUDY

The primary objectives of the study include:

- Developing an optimised UHPC matrix, based on optimum particle packing of South African materials.
- Establishing the optimum combined fibre and superplasticiser content for UHPC.
- Developing a material model to determine the tensile stress-strain relationship for UHPFRC.
- Comparing the experimental flexural tensile strength results to the theoretically calculated moment-curvature and load-displacement responses.

The secondary objectives of the study include:

- Determining the fresh and mechanical properties of the optimised mix design, which include flowability, compressive strength, tensile strength and modulus of elasticity.
- Investigate the effect of heat curing on the mechanical properties of UHPFRC.
- Establishing the effect of specimen size on the compressive and flexural tensile strength of UHPFRC members.

1.4 SCOPE OF THE STUDY

The scope of the study was limited to physical testing of UHPC containing locally available materials. Only optimum particle packing was considered as a technique to optimise the mix composition. Materials easily available in South Africa were utilised and only one source of binder, aggregate and superplasticiser was considered. Short straight steel fibres were used as fibre reinforcement. No other fibre types or shapes were considered. The effect of mixing procedures and casting direction on the mechanical properties were standardised. Curing regimes considered were conventional water bath curing and thermal (80 °C) water bath curing. Setting time, autogenous shrinkage, chloride penetration, freeze-thaw and thermal expansion fall outside the scope of this study. Behaviour of the experimental beams (100 x 100 x 500 mm) was compared to the developed material model to determine the tensile stress-strain relationship for UHPFRC by using hand calculations.

1.5 METHODOLOGY

Research can be performed by using qualitative, quantitative or mixed methods of research. Quantitative research is described as the systematic, empirical investigation of numerical or scientific data via statistical, mathematical or computational techniques. The data can be collected through experiments, data analysis and measurements. According to Brynard et al. (2016), quantitative methodology is associated with analytical research and its purpose is to arrive at a universal statement. By counting and measuring "things" or "objects", data is produced. The method could include techniques such as observation, preliminary investigations, a quantitative analysis and laboratory experiments. This study used the quantitative method of research since it comprises scientific research, which is conducted by using other research and experiments to gain knowledge of the different assumptions, methodologies, practices and theories that are necessary for research.

Particle Size Distribution (PSD) of all materials were determined, whereafter an optimised UHPC matrix was developed by using the modified Andreasen and Andersen particle packing model. Microstructure studies were also conducted on various materials using a Scanning Electron Microscope (SEM). Response Surface Methodology (RSM) was used for the mixture design, statistical analysis, analysis of data and optimisation of the superplasticiser content and steel fibre amount. The influence of parameters was investigated by using an analysis of variance (ANOVA) and the quality of the model was determined by the coefficient of determination R^2. In this study, the cost, flow, compressive strength, modulus of elasticity and splitting tensile strength denote the responses. Two parameters, namely, superplasticiser content and steel fibre amount were selected to describe this model. A final optimised mixture was then determined from the results and conclusions obtained. The mechanical properties of the final optimised mixture were also investigated and compared to that of the predicted values as obtained from the RSM. Cost, flow, compressive strength, modulus of elasticity, splitting tensile strength, direct tensile strength, flexural tensile strength, specimen size effect, shrinkage and creep for the final optimised mixture were determined. The effect of curing regime on the material properties was also investigated. The flexural performance of small experimental UHPC members (beams) and their maximum load capacity were determined. The cost for the experimental precast beams were compared to Normal Strength Concrete (NSC) (30MPa). The results obtained were then compared to the numerically predicted behaviour.

1.6 ORGANISATION OF REPORT

The report consists of the following chapters:

- Chapter 1 serves as the introduction to the dissertation, outlining the objectives, scope, methodology and organisation of the dissertation.
- Chapter 2 contains the literature review.
- Chapter 3 includes the optimised mixture composition design and results.
- Chapter 4 provides the detailed description of the experimental set-up for the optimised mixture.
- Chapter 5 includes the results obtained for the optimised mixture.
- Chapter 6 includes the developed material model.
- Chapter 7 concludes with a summary of the addressed research objectives. Recommendations on future research activities is summarised.
- Appendix A contains graphs of measured load-displacement behaviour of beams tested.

2 LITERATURE REVIEW

2.1 INTRODUCTION

This chapter presents a theoretical framework on UHPC that is based on decades of research. The objective of this chapter is to provide insight and understanding into the material characteristics and development of UHPC. Some of the available methods for determining optimised mixture proportions were reviewed.

2.1.1 Background

According to Richard & Cheyrezy (1995), UHPC represents the highest development of High-Performance Concrete (HPC). UHPC is an advanced building material, consisting of high-performance concrete matrix and fibre reinforcement (Yu et al., 2014).

UHPC has enhanced mechanical properties, improved fatigue behaviour, low porosity, excellent durability, non-brittle behaviour and excellent environmental resistance (Richard & Cheyrezy, 1995; Tang, 2004; Wille et al., 2011a; Aldahdooh et al., 2013; Ghafari et al., 2014; Abbas et al., 2016). Therefore, UHPFRC members require less maintenance which leads to reduced life-cycle costs (Blais & Couture, 1999; Racky, 2004). According to Abbas et al. (2016), this material can lead to sustainable construction by reducing the cross-sectional dimensions of structural members which, in effect, reduces the self-weight of the structure with less materials used, thus reducing transportation and installation costs and lowering labour costs. Wille et al. (2012) state that, in the construction industry, the design of cementitious materials with enhanced material properties, durability and ductility, while maintaining small crack width under tensile loading, has become a priority for the construction of longer span bridges and taller buildings as well as sustainable and durable structures. Since the material properties of concrete becomes more and more important with time, questions arise on how to develop new types of concrete that can meet the technical and architectural demands (Fennis et al., 2009).

UHPC is a more complex system compared to Normal Strength Concrete (NSC) which contains a high content of cementitious materials, low water-to-binder (w/b) ratio and a high dosage of superplasticiser. The fibre content in UHPC, which can be up to 6 % by volume, is much higher compared to normal reinforced concrete. The prediction of behaviour of UHPC is more difficult compared to that of conventional concrete, due to the higher number of mixture ingredients and their combinations and proportions (Ghafari et al., 2015b). UHPC has compressive strength and tensile strength, exceeding seven times and three times respectively, that of conventional concrete (Graybeal & Hartmann, 2003). UHPC matrix properties are influenced by various parameters such as the cement content, quantity of admixtures, particle size, fibre content, w/b ratio, size effect of specimens, curing regime and the rate of loading (Savino et al., 2019). Relatively high binder and fibre content are used in UHPC mixture proportions; however, the addition of these materials into the concrete mixture takes place without any detailed explanation or theoretical support (Yu et al., 2014). Furthermore, the material cost, production cost, energy consumption and embodied CO_2 emissions of UHPC are significantly higher than that of conventional concrete (Habert et al., 2013; Ghafari et al., 2015b; Yoo et al., 2018). Therefore, an optimised mix composition is of great importance.

2.1.2 History of UHPC

Cementitious materials with a compressive strength of over 150 MPa and a tensile strength of over 7 MPa have attracted the attention of researchers around the world (Ahlborn et al., 2008; Habel et al., 2008; Wille et al., 2011a, 2011b; Yoo et al., 2018). Research efforts since the 1980s have focussed on obtaining higher strength by reduced w/b ratio and decreased aggregate size, leading to compact material microstructure with excellent mechanical performance. As early as the 1970s, Yudenfreund et al. (1972a; 1972b) obtained a compressive strength of 230 MPa by using low porosity cement paste, low water-to-cement (w/c) ratio of 0.2, a vacuum mixing process and fine ground cement. Pre-treatment was first applied by Roy et al. (1972), who obtained compressive strength of 510 MPa by using pressure and temperatures of up to 250 °C. Bache (1981) introduced Densified Small Particles (DSP). This led to compressive strengths between 120 MPa and 270 MPa. Reactive Powder Concrete (RPC) was developed by Richard & Cheyrezy (1995). The concrete is heat cured for three days, starting twenty-four hours after casting at 90 °C. RPC exhibit compressive strengths of up to 230 MPa and flexural strengths of up to 60 MPa. RPC is now more generally known as UHPC. According to Wille et al. (2011a), the term Ultra-High-Performance Concrete was first used by De Larrard & Sedran (1994). The mechanism for this method is illustrated in **Figure 2-1**.

The first precast, heat treated RPC footbridge was constructed in 1997 in Sherbrooke, Quebec (Blais & Couture, 1999; Aïtcin et al., 2000). The bridge that spans 60 m over the Magog River is a post-tensioned truss containing no conventional steel reinforcement. The Mediterranean Culture Museum in Marseille, France, the Gärtnerplatz bridge in Kassel, Germany, the Stade Jean-Bouin rugby stadium in Paris, France, the Sakata Mirai footbridge in Sakata, France, the Shepherds creek road bridge in Australia and the Wapello country bridge in the United States of America are just a few examples of the successful application of UHPC (Habert et al., 2013; Hiremath & Yaragal, 2017b; Yu et al., 2017). Very thin architectural shell structures can be designed due to the design flexibility of UHPC (Vicenzino et al., 2005). According to Yoo et al. (2018), UHPC or UHPFRC is mostly used for thin plate structures which include bridge decks, roofs and walls.

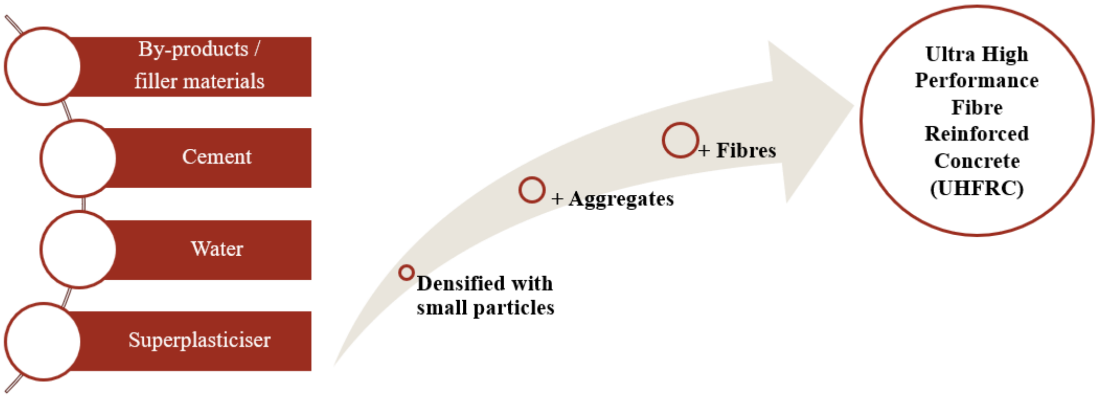

Figure 2-1: Typical DSP approach mechanism (adapted from Ghafari et al., 2015c)

2.1.3 Sustainability and environmental impact

Over the last few decades, the cement industry has been engaged in efforts to reduce the environmental impact by researching various sustainable eco-friendly solutions. Fennis & Walraven (2012) stated that, in 2011, an estimated 3.4 billion tons of Portland cement production was responsible for about 7% of the total anthropogenic CO_2 emissions. Promoting sustainable construction approaches is not only critical for the environment but could also contribute greatly to cost savings and the sustainability of buildings and other infrastructures such as tall structures, buildings, bridges and military structures, whilst at the same time enhancing the architectural and aesthetical appeal. Therefore, innovative design of concrete structures and mixture designs, to reduce this environmental impact, is of great importance (Habert et al., 2013).

The application of UHPC in the construction industry is limited due to its high material cost, high energy consumption, high embodied CO_2 emissions and increased quality control requirements compared to that of Normal Strength Concrete (NSC) (Habert et al., 2013; Yu et al., 2014; Binard, 2017; Savino et al., 2019). The high material cost can be attributed to the high cement content and addition of fibres. Filho et al. (2012) state that the sustainability of UHPC still needs to be evaluated regarding the use of higher dosages of binder compared to that of regularly used mixtures. According to Wille & Boisvert-Cotulio (2015), the cost of fibre reinforcement represents almost half the cost of the UHPFRC composite, while supplementary materials and aggregates have an insignificant effect on the total cost. However, UHPC exhibits enhanced mechanical and durability properties, which lead to reduced cross-sectional dimensions of structural members. Consequently, material cost can be reduced compared to that of NSC member with a larger cross-section, as the overall cost of structures is directly linked to the cross-sectional dimensions of the structural elements (Filho et al., 2012; Yoo & Yoon, 2016). Yu et al. (2017) reported that UHPFRC L-shaped wall elements required 73 % less material compared to ordinary steel reinforced L-shaped wall elements.

Furthermore, by-products can be utilised as cement replacement materials, which will make UHPC more sustainable (Soutsos et al., 2005; Yazici, 2006; El-Dieb, 2009; Fennis et al., 2009; Filho et al., 2012; Yu et al., 2014, 2017). The utilisation of these filler materials will not only reduce the embodied CO_2 emissions, but residual products from other industries are re-used and this leads to less materials being dumped as landfill (Fennis et al., 2009). Nevertheless, it is possible to reduce cement content by more than 50 % and CO_2 emissions by 25 % when particle packing models for optimisation of concrete mixture design are utilised (Fennis & Walraven, 2012). Yu et al. (2017) state that using particle packing models for the design of UHPFRC mixtures, without incorporating industrial by-products in the mixture design, is ineffective in reducing the environmental impact. The inclusion of industrial by-products is currently the most common method to reduce UHPFRC’s economic and environmental disadvantages (Yu et al., 2015a). Concrete mixture designs should incorporate more and more mineral components and lower w/b ratios to ensure sustainable and environmental development, that can increase the life cycle of concrete structures (Aïtcin, 2000). Yu et al. (2017) reported about 30 % lower embodied CO_2 emissions when industrial by-products are utilised as filler materials in UHPFRC. Therefore, the effective utilisation of industrial by-products is a sustainable method to the development of UHPC or UHPFRC.

Due to improved durability characteristics, when using UHPC members, maintenance cost and life cycle cost are reduced (Blais & Couture, 1999; Aïtcin, 2000; Racky, 2004). According to Abbas et al. (2016), UHPC provides a viable and long-term solution for improved sustainable construction. Producing UHPC by using locally available materials under normal curing conditions will make UHPC more cost-effective and sustainable (Abbas et al., 2016). Moreover, according to Habert et al. (2013), applications of UHPC over the past 10 years have demonstrated that it is a fast, efficient and cost-effective method for the rehabilitation and repair of existing structures. The use of UHPC can have a positive impact on the reduction of greenhouse gas emissions in certain building projects. Habert et al. (2013) reported that eco-UHPFRC has been implemented successfully for bridge rehabilitation. Rehabilitation with UHPFRC, and even more for eco-UHPFRC, has a lower impact over the life cycle compared to that of conventional concrete (Habert et al., 2013). Binard (2017) concluded that for UHPC to become cost-effective and widely implemented in the precast industry, a method for standard production with local materials and larger placements should be researched.

2.2 MATERIALS

UHPC has been investigated in recent years, focusing on various material parameters (Kahanji et al., 2017). UHPC is characterised by its high content of cementitious material, very low w/b ratio, elimination of coarse aggregates, high superplasticiser dosage and the addition of steel fibre reinforcement in the concrete matrix (Chan & Chu, 2004; Habel et al., 2008; Yu et al., 2017; Yoo et al., 2018).

Yu et al. (2014) stated that a large amount of binders and other constituents are poorly utilised in UHPC. The improvement of the micro and macro properties of the mixture is a key factor in the production of UHPC. This will ensure maximum particle packing density, mechanical homogeneity and minimum flaw sizes (Shah & Weiss 1998; Vernet 2004; Schmidt & Fehling, 2005; Wille et al., 2011a; Shi et al., 2015). To effectively improve flowability, mechanical properties, durability and cost of UHPFRC, cementitious materials, sand gradation, fibre reinforcement and superplasticiser must be combined appropriately (De Larrard & Sedran, 1994; Wille & Boisvert-Cotulio, 2015). **Table 2-1** shows an example of the range of UHPFRC mixture ingredients used in various studies for the effective production of UHPC (Schmidt et al., 2004; Talebinejad et al., 2004; Fehling et al., 2008; Abbas et al., 2016; Schmidt et al., 2012).

Table 2-1: Typical composition of UHPFRC

UHPFRC constituents	Range
Cement	27 - 40 *(% by weight)*
Silica Fume	*15 - 30 (% by cement weight)*
Fly Ash	*10 - 30 (% by volume)*
Sand	35 - 45 *(% by weight)*
Superplasticiser	0.5 - 3 *(% by weight)*
Water	4 - 10 *(% by weight)*
Steel Fibres	0 - 8 *(% by weight)*

2.2.1 Binders

High cement contents are used in the production of UHPC and UHPFRC (normally more than 1000 kg/m^3) compared to that used in normal-strength concrete (NSC) (Schmidt & Fehling, 2005; Yu et al., 2014). An increase in compressive strength was observed by Talebinejad et al. (2004), with an increase in cement content. Cement content and type of cement play a significant role in UHPC mixture regarding strength development and workability (Habel et al., 2008; Yu et al., 2014). However, the compressive strength tends to decline beyond an optimum cement content of 1700 kg/m^3 (Talebinejad et al., 2004). Most of the cement particles just act as filler material, as only about 40% by volume of the cement in UHPC mixtures hydrates (Neville, 1995; Yu et al., 2014). This can be attributed to the very low w/b ratio of UHPC.

Therefore, up to 40% by volume of cement can be replaced with cheaper filler materials such as fly ash, silica fume or ground granulated blast furnace slag without sacrificing the material properties of UHPC (Soutsos et al. ,2005; Yazici, 2006; El-Dieb, 2009; Fennis et al., 2009; Filho et al., 2012; Yu et al., 2014). Literature shows that these powders have different effects on the properties of concrete such as cement hydration (Yang et al., 2016), mechanical properties development (Kang et al., 2010) and sustainable properties (Yang et al., 2015). According to Fennis et al. (2009), an ecological concrete can be designed by replacing cement with these by-products. Filler materials can be added to the UHPC mix, individually or in various combinations (Mazloom et al., 2004). The inclusion of by-products in UHPC can lead to a reduced unit cost of UHPC, increased ultimate compressive strength, improved durability and better workability (Zain et al., 2000; Wille et al., 2011a; Yu et al., 2014). The binder amount can further be reduced by achieving an improved particle packing density (Yu et al., 2014).

Habert et al. (2013) reported on an original concept called eco-UHPFRC which includes a high dosage of additions, a low cement content and the utilisation of local materials. With low cement content, it is of vital importance to control the water demand of the concrete mixture (Fennis et al., 2009). Ghafari et al. (2015b) reported that UHPC mixtures with low cement content can still reach compressive strengths exceeding 150 MPa, even without applying thermal curing. It is worthwhile to investigate how to produce UHPC with relatively low cement content while keeping a reasonable and practical balance between the binder amount, unit cost and mechanical properties (Yu et al., 2014; Ghafari et al., 2015b; Meng et al., 2017).

2.2.1.1 Silica Fume

Silica fume is collected by filters as a by-product of the manufacturing of silicon metal and ferro-silicon alloys and does not only enhance the strength properties of the UHPC mixture through its high pozzolanic reactivity, but as a binder, it will improve the workability of the mixture by filling voids between coarser particles due to its much finer particle size (Richard & Cheyrezy, 1995; Wille et al., 2011a; Abbas et al., 2016). It can be supplied as collected from the filters which is known as undensified silica fume (bulk density typically 150 kg/m^3 to 350 kg/m^3) or after treatment to increase its bulk density typically above 500 kg/m^3 (densified silica fume). Silica fume has long been used as a cement replacement material and was found to be the most effective addition (De Larrard, 1989).

Additional calcium silicate hydrates (C-S-H) are formed when silica fume reacts with calcium hydroxide released from the cement paste (Kahanji et al., 2017). A lower water demand and thus better flowability can be obtained with a finer silica fume or with silica fume with a lower carbon content (Wille & Boisvert-Cotulio, 2015). Silica fume is typically used in combination with a plasticiser and/or superplasticiser (SANS 53263-1:2011). Silica fume has a median particle size of approximately 0.5 µm to 1.2 µm (Wille et al., 2011a) and consists of mainly spherical particles. However, silica fume particles have a high tendency towards agglomeration (see **Figure 2-2**) due to their high surface energy (Ghafari et al., 2015b). Van der Putten et al. (2017) concluded that the ideal technique to measure the PSD of silica fume is after mixing, in order to determine how many agglomerates are really in the mixture. According to various authors (Habel et al., 2008; Wille et al., 2011a), a larger mean particle size of silica fume results in a reduction in water demand and it has no effect on the compressive strength.

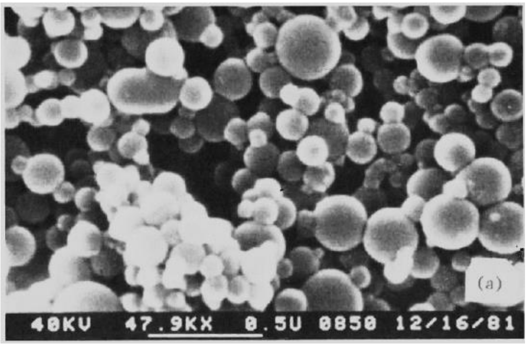

Figure 2-2: Silica fume (Mantel, 1991)

Bhanja & Sengupta (2005) reported that the mechanical properties of concrete increased when incorporating silica fume in the mixture. According to El-Dieb (2009), the addition of silica fume in the UHPC mixture can increase compressive strength gain at later ages. Different researchers recommended different silica fume dosages ranging from 10 % to 30 % of the total binder material to obtain denser particle packing and higher strength properties (De Larrrard, 1989; Richard & Cheyrezy, 1995; Chan & Chu, 2004; Habel et al., 2008; Aldahdooh et al., 2013). Bhanja & Sengupta (2005) concluded that the optimal replacement percentage is not constant but depends on the w/c ratio of the mix. According to their research, the optimum silica fume replacement percentage is around 15 % when using a 0.26 w/b ratio.

2.2.1.2 Fly Ash

Fly ash, a coal combustion by-product that is composed of the particulates that are driven out of coal-fired boilers (Shi et al., 2015), improves the workability, strength and durability of concrete due to very small particles that make the concrete highly dense and reduces permeability. Different types of coal and the type of boiler used produce different fly ashes (SANS 50450-1:2014). The pozzolanic reaction of fly ash normally begins at the age of three days after mixing with cement and water (Yu et al., 2017). This pozzolanic reaction is significantly slower compared to ordinary Portland cement hydration, thus the mechanical properties of concrete containing fly ash are significantly improved at later stages. Soutsos et al. (2018) reported that the 28-day compressive strengths of concrete containing 30 % fly ash (replacement) were higher than the strength of the corresponding concrete with 100 % Portland Cement. Fly ash has a median particle size of approximately 10 µm (Wille & Boisvert-Cotulio, 2015). Fly ash enhances flowability due to its spherical particle shape. This spherical shape can be seen in **Figure 2-3**. Fly ash is abundantly available and has a positive environmental impact when used as a cement replacement material.

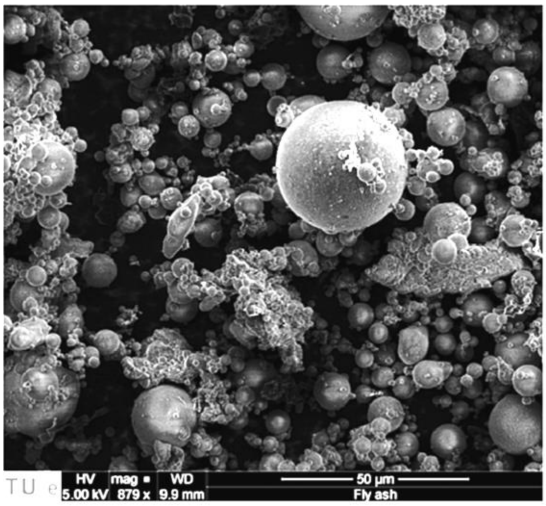

Figure 2-3: SEM picture of fly ash (Yu et al., 2017)

2.2.2 Water/Binder ratio

From the early 1970's, it is well known that decreasing the w/b ratio decreases the porosity of the cement paste, which in effect increases the strength of the concrete (Yudenfreund et al., 1972a). As mentioned earlier, a very low w/b ratio is used in UHPC mixtures. Both the fresh and hardened properties of concrete are influenced by w/b ratio (Droll, 2004). Compressive strength decreases with an increase in w/b ratio (Wille et al., 2011a; Yoo et al., 2018). Rossi (2013) stated that a UHPC matrix with an extremely low w/b ratio will continue to develop and experience additional densification over time.

Various studies recommended an optimum w/b ratio between 0.13 to 0.20 to achieve maximum particle density (De Larrard & Sedran, 1994; Richard & Cheyrezy, 1995; Shi et al., 2015). However, compressive strengths higher than 150 MPa were reached in experiments performed by various researchers (Droll, 2004; Wille et al., 2011a) when using a w/b ratio of 0.25. Filho et al. (2012), on the other hand, recommend using a w/b ratio of 0.17, which leads to outstanding performance of the cementitious composite. Wille et al. (2011a) concluded that a w/c ratio ranging from 0.16 to 0.27 is recommended.

Wille et al. (2012) stated that the w/c ratio can be reduced while still maintaining the same flowability when the rheological behaviour of the UHPC paste is improved. Abbas et al. (2016) stated that the w/b ratio is not the only role player in UHPC's strength; the curing regime, properties of mixture ingredients, mixing procedures and mixer type are also of great importance. Aldahdooh et al. (2013) reported that the compressive strength is independent of the binder content for a given w/b ratio and superplasticiser/cement ratio. They concluded that an increase in binder content did not improve the strength compared with the required design strength. This was attributed to the rise in capillary porosity with an increase in cement content.

2.2.3 Superplasticisers

Due to the very low w/b ratio used in UHPC mixtures, the reduced flowability can be resolved by the addition of superplasticisers; also known as high range water reducers (De Larrard, 1989; Habel et al., 2008; Abbas et al., 2016; Meng et al., 2017). Superplasticisers are chemical admixtures used to control the workability of concrete, making it possible to reduce the water demand.

The dispersing effect of superplasticiser, used at its optimum value, improves the rheology of the cement paste (Bonneau et al., 2000). Extremely high dosages of superplasticiser are undesirable (Smit, 2015). The mixture is likely to experience segregation, retardation and air entrapment if excessive dosages of superplasticiser are added to the mixture (Domone & Illston, 2010). To determine the required superplasticiser dosage, the compatibility between the mixture ingredients and the type of superplasticiser must be defined. Common problems that can arise as a result of incompatibility between cement and superplasticiser are rapid loss of workability, excessive quickening of setting and low rates of strength gain. Moreover, high performance concretes almost always incorporate additions or fillers which further complicate the chemical behaviour of the cement-based system.

According to Tue et al. (2008), workability and a more efficient use of superplasticiser can further be enhanced by adding the superplasticiser stepwise, rather than adding all at once, resulting in an improved dispersing effect. Concrete with a dense packing is achieved by using a large quantity of superplasticiser (Bache, 1981). Van der Putten et al. (2017) reported that, due to the addition of fine particles in UHPC, agglomeration can occur. Therefore, superplasticiser should be added to achieve a fully dispersed mixture. Superplasticiser gathers onto the cement particles to decrease agglomeration and reduces the water demand by releasing the water caught between the agglomerates (Van der Putten et al., 2017). Wille & Boisvert-Cotulio (2015) mixed one third of the superplasticiser into the water and then added that to the mix. Afterwards, all the remaining superplasticiser was added. Wille et al. (2011a) found that a polycarboxylate ether-based superplasticiser was very effective. Numerous studies used superplasticiser dosages ranging between 1 % and 8 % by cement weight (Bache, 1981; Fehling et al., 2008; Habel et al., 2008; Wille et al., 2011a; Schmidt et al., 2012).

2.2.4 Aggregates

Aggregates are a wide range of coarse to medium grained particulate materials used in construction, including sand, gravel and crushed stone. The composition, shape and size of the aggregate all have a significant impact on the workability and mechanical properties of concrete. Damage at the interfacial transition zone (ITZ) between the cementitious matrixes and aggregates are the main reason for failure in conventional concrete (Jun et al., 2008; Shi et al., 2015). Cracks will typically form at the ITZ during loading (Afroughsabet et al., 2016). This weakness can be reduced by eliminating coarse aggregates in the UHPC mixtures (Aïtcin, 2000). However, Fehling et al. (2004) reported that UHPC that contains coarse aggregates reached a slightly higher compressive strength than the UHPC with only fine aggregates. This was confirmed by Collepardi et al. (1997), who reported that no significant difference in compressive strength was observed (see **Figure 2-4**) and the amount of drying shrinkage and creep strain was reduced when coarse aggregate was added to the mixture. However, lower flexural strength was obtained in the mixtures containing coarse aggregate (Collepardi et al., 1997; Orgass & Klug, 2004).

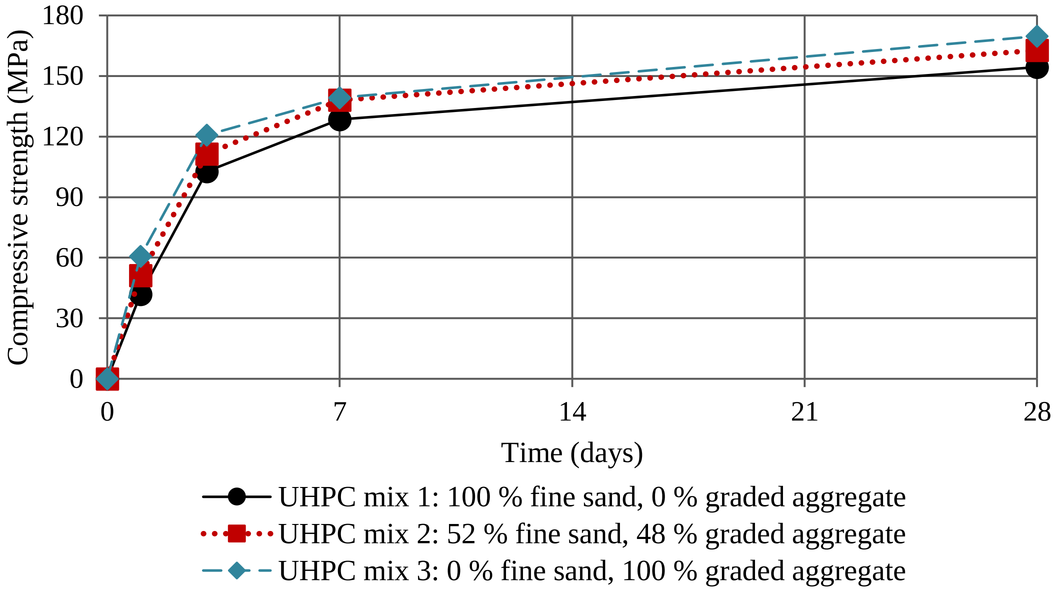

Figure 2-4: Effect of replacement of fine sand with graded aggregate (adapted from Collepardi et al., 1997)

UHPC does not normally contain coarse aggregates larger than 7 mm in size (Binard, 2017; Kahanji et al., 2017). Yoo et al. (2018), reported that a lower production cost can be achieved when utilising coarse aggregates in the UHPC mixture. Park et al. (2008) recommend an optimum aggregate-to-cement ratio of 1:1. However, Wille et al. (2011a) increased this ratio of aggregate-to-cement to 1.4:1 in order to ensure that the amount of cement and, therefore, shrinkage is as low as possible. An aggregate-to-cement ratio of 2:1 by weight is suggested by Wille & Boisvert-Cotulio (2015). Since aggregates are less expensive than the materials used in the paste, the higher the aggregate-to-cement ratio can be, without significantly losing workability and strength, the more cost-effective the UHPC would be.

2.2.5 Steel Fibres

UHPC can be very brittle due to its high strength and homogeneity; it is, therefore, reinforced with a small percentage, normally 1 % to 6 % by mixture volume of different lengths and diameters of steel fibres (Bindiganavile et al., 2002; Graybeal, 2006; Abbas et al., 2015; Aoude et al., 2015; Wang et al., 2015; Wille & Boisvert-Cotulio, 2015). Yu et al. (2015b) concluded that short straight steel fibres can considerably improve the homogeneity of the UHPC mixture and Orgass & Klug (2004) reported that short straight steel fibres can increase the mechanical properties such as compressive and tensile strength. Short straight steel fibres will improve fibre distribution and orientation, thus improving the structure of the uncracked concrete (Orgass & Klug, 2004). The proper addition of steel fibres will not only make UHPC more ductile, but it will also enhance the compressive strength, tensile behaviour, toughness, post-cracking strength, durability and energy absorption capacity (Yu et al., 2014; Wille et al., 2011b; Hassan et al., 2012; Cadoni et al., 2019). According to Abbas et al. (2015), the addition of steel fibres in UHPC matrix is mainly to enhance the tensile properties and toughness, not to increase the compressive strength. Due to the addition of steel fibres in UHPC, the fibres can effectively bridge microcracks and delay crack propagation in the hardened concrete (Bayard & Plé, 2003; Yu et al., 2014; Afroughsabet et al., 2016). According to Cattaneo & Biolzi (2009), formation of microcracks is caused by internal stresses in the hardened concrete. The addition of randomly distributed steel fibres allow the stress within the concrete microstructure to transfer, which prevents the propagation of the cracks. This causes improvement in the post-cracking behaviour and toughness of UHPC (Li & Maalej, 1996). Naaman (2003) stated that the tensile strength of the hardened concrete is lower than that of the steel fibres. Therefore, the failure of the bonding between the fibres and concrete paste is largely the reason for failure.

Another parameter influencing the mechanical properties of UHPFRC is fibre orientation with respect to crack formation. Afroughsabet et al. (2016) reported that fibre alignment has a significant influence on the mechanical properties of UHPC. Crack openings are normally limited to half the length of the longest fibres in the matrix (Hassan et al., 2012). When the fibres are aligned perpendicular to the crack openings, the effect of fibres on the performance of UHPFRC is maximised. However, it is nearly impossible to align all the fibres in the ideal direction (Yu et al., 2015b). According to Wille et al. (2014), fibre orientation can be affected by various parameters, such as fresh-state properties, casting method, vibration, flow direction and formwork geometry.

The required fibre content depends on various parameters which include fibre strength, length-to-diameter ratio, fibre orientation and bond behaviour between fibre and surrounding matrix (Wille & Boisvert-Cotulio, 2015). In many investigations, steel fibres were added to the UHPC matrix, seemingly randomly (sometimes with large volumetric amounts), without considering the effectiveness of the fibre dosage and efficiency of the used fibres. Often no explanation was provided for the chosen fibre type or content.

Straight steel fibres with a length of 13 mm and a diameter of 0.20 mm are the most commonly used type of steel fibre in UHPFRC (Collepardi et al., 1997; Bayard & Plé, 2003; Schmidt et al., 2004; Fehling et al., 2008; Kang et al., 2010; Wille et al., 2011b; Prem et al., 2013; Yu et al., 2014; Kahanji et al., 2017; Meng et al., 2017). Wille & Boisvert-Cotulio (2015) reported that these fibres outperformed other types of fibres in tensile strength and workability tests. Abbas et al. (2015) reported that mixtures containing short steel micro fibres showed enhanced flexural performance compared to that of mixtures containing longer steel fibres at similar volumes. According to single fibre pull-out tests conducted by Wille et al. (2011b), these fibres exhibit excellent load-versus-slip behaviour up to about the full embedded length. Fibre pull-out behaviour is dependent on the matrix strength and length of the fibres (Hassan et al., 2012). Rossi (2013) reported that fibre length-to-diameter ratio (aspect ratio) influences the mechanical efficiency of the fibres. Savino et al. (2019) state that the length-to-diameter ratio significantly influences the post-cracking behaviour of UHPFRC. The fibre content in UHPFRC mixtures can be reduced by using steel fibres with a higher aspect ratio (Bornemann & Faber, 2004). Wille & Boisvert-Cotulio (2015) state that a high packing density UHPC matrix allows for improved performance of smooth high strength steel fibres, normally with a length-to-diameter ratio of 65 and a fibre diameter of 0.2 mm. However, Yu et al. (2015b) observed that hybrid fibre reinforced concrete yields higher flowability compared to UHPFRC containing only straight steel fibres.

For an economical and workable mixture, various researchers recommend using 2 % by mixture volume of steel fibres (Meng et al., 2017; Yu et al., 2017). Wille et al. (2011b) stated that the mechanical properties improved when adding straight steel fibres up to 2.5 % by volume in replacement of the equivalent volume of sand. However, Yu et al. (2017) reported a sharp decrease in the UHPFRC flowability with the addition of 2.5 % steel fibres by volume. This may be caused by the cross-over of steel fibres which increased the resistance of the flow of the fresh UHPFRC as illustrated in **Figure 2-5** (Yu et al., 2017). Savino et al. (2019) stated that fibre dosages higher than 3 % caused fibre balling in the fresh mixture. Fibre balling affects the mechanical properties of the UHPFRC and creates honeycombing which reduces the quality of the UHPFRC (Savino et al., 2019). Habel et al. (2008), on the other hand, reported that self-consolidating behaviour of the fresh mixture was kept, until the addition of 5.5 % by volume of fibres. UHPFRC mixtures containing higher steel fibre dosages exhibit improved durability (Abbas et al., 2015). However, Wille et al. (2011a) stated that reducing steel fibre content is crucial in reducing the unit cost. An optimum steel fibre content should be implemented to balance workability, mechanical properties and cost (Wille et al., 2011b). Limited information is available regarding the influence of the fibre length and fibre dosage on the mechanical properties, especially for UHPFRC cured under conventional curing conditions (Abbas et al., 2015). Yu et al. (2015b) reported that a practical method for efficiently utilising steel fibres is of great importance and needs further investigation.

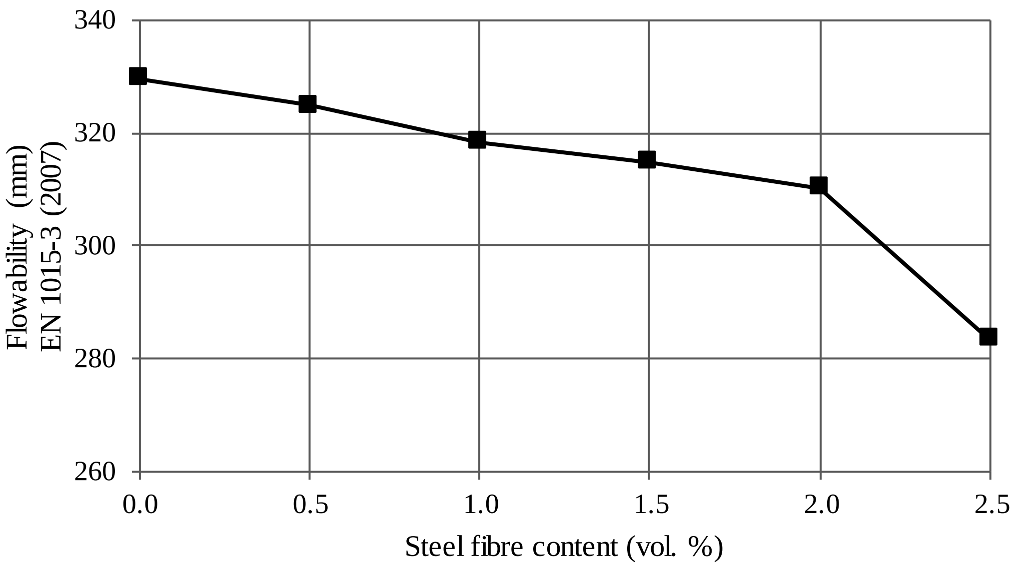

Figure 2-5: Flowability of the fresh UHPFRC with different steel fibre content (adapted from Yu et al., 2017)

2.3 MIXTURE DESIGN

Abbas et al. (2016) emphasise the importance of economical and sustainable mix designs to achieve a denser matrix, reduced porosity and improved internal microstructure. De Larrard & Sedran (2002) state that, mathematically, the mixture design for UHPC involves more unknowns, variables and dimensions than ever before. Modern concrete is more than just a mixture of cement, water and aggregate. It contains mineral and chemical admixtures and fibres (Aïtcin, 2000). There are various approaches to design concrete – especially so for UHPC.

According to Wille & Boisvert-Cotulio (2015), workability, strength and durability can be controlled by the particle packing density of aggregates. Wille et al. (2012) stated that, without increasing the particle packing density, reducing the w/b ratio will lead to a decrease in flowability, an increase in entrapped air and no improvement of compressive strength. High particle packing density is an important property of UHPC (Wille et al., 2011b). Increasing the particle packing density causes a decrease in the porosity of the paste, resulting in improved durability performance. Focusing material design on particle packing optimisation could thus simplify the research activities (Wille & Boisvert-Cotulio, 2015). Furthermore, statistical methods have also been proposed for designing UHPC mixtures (Abbas et al., 2016). The efficiency of this method to predict properties of concrete has been widely reported. For example, Ghafari et al. (2014) used RSM for predicting the maximum flexural strength of self-compacting steel-fibre reinforced UHPC with varying steel fibre contents.

Yu et al. (2014) stated that, in most cases, UHPC mix proportions are specified without any detailed explanation or theoretical validation. It is, therefore, questionable whether the concrete matrix was optimal, with the binder and fibres used effectively (Yu et al., 2015b). An effective mix design method predicting the properties of concrete in fresh and hardened states is of great importance (Ghafari et al., 2015b; Yu et al., 2015b; Meng et al., 2017) Wille et al. (2011a) and De Larrard & Sedran (2002) state that “à la carte" mixture designs should be developed that require no special heat or pressure treatment, a standard mixer and that use available materials at minimum cost, while still achieving ultra-high compressive strength.

2.3.1 Particle packing theory

Some studies put emphasis on the importance of the right number of particles of different sizes in optimising UHPC mixture composition (De Larrard & Sedran, 1994; Droll, 2004; Yu et al., 2014). As already stated, an optimum particle packing density of the concrete matrix is the key for good and durable concrete (Wille & Boisvert-Cotulio, 2015). Fine components play a key role in high performance concrete (Droll, 2004). The addition of fine particles into the concrete matrix help to fill voids which leaves limited space for water and, in effect, reduces the water requirement (Fennis & Walraven, 2012). Furthermore, the increased particle packing of aggregates will improve the strength of the concrete if all voids are filled with cement paste. According to Fennis & Walraven (2012), particle packing methods can be divided into three groups:

- Optimisation curves – the most accurate fit between the overall PSD of the mixture and an optimum curve is obtained.

- Particle packing models (analytical models) - the total packing density of the mixture based on the geometry of the combined group of particles is calculated.

- Discrete element models – a virtual packing structure is generated from a given PSD.

De Larrard (1989) proposed a Linear Packing Density Model (LPDM) based on properties of multimodal, discretely sized particles. However, the LPDM model did not focus on the relationship between materials proportioning and packing density and, therefore, a new improved model known as the Solid Suspension Model (SSM) was developed (De Larrard & Sedran, 1994). Thereafter, De Larrard & Sedran (2002) proposed the Compressible Packing Model (CPM) which is based on the compaction index concept and virtual packing density. However, the CPM still uses the packing of monosized classes to predict the packing of the composed mixture. Fennis et al. (2009) then developed a concrete mix design method based on the concept of De Larrard & Sedran (1994). Although the design methods over the last 25 years show excellent rheological behaviour, mechanical properties and durability performance (Rossi, 2013; Wang et al., 2014), most of these design methods were based on the packing fraction of individual components such as cement and sand and their combination. As a result, it is difficult to incorporate very fine particles in these mix design methods (Yu et al., 2014).

Another approach to effectively design concrete is based on an integral PSD of continuously graded mixes. As early as the 1890s, Féret (1892) proposed that concrete strength is influenced by the choice of aggregate. Various researchers have tried to find the optimal grading curve (Fennis & Walraven, 2012). The most recognised curve in this field is the Fuller curve (Fuller & Thompson, 1907) and mix design calculations based on this curve are still used today. Fuller & Thomsen (1907) showed that the properties of concrete are affected by the packing of concrete aggregates. They concluded that a continuous grading of the aggregates in the concrete mixture can help to significantly improve the concrete properties. The Fuller curve is described in **Equation 2-1**.

$$P(D) = (\frac{D}{D_{max}})^{q} \qquad \textbf{Equation 2-1}$$

where $P(D)$ is the fraction of solids being smaller than size D, D is the particle size being considered, D_{max} is the maximum particle size in the mixture and q is the distribution modulus which adjusts the curve for fineness or coarseness. Andreasen & Andersen (1930) proposed using a q value ranging from 0.33 to 0.50. Funk & Dinger (1980) recognised that the minimum particle size was not considered and recommended that a finite lower size limit (D_{min}) is required so that the range of fine particles is better represented.

They proposed a modification to Andreasen and Andersen particle packing model, as indicated in **Equation 2-2**.

$$P(D) = \frac{D^{q} - D_{min}^{q}}{D_{max}^{q} - D_{min}^{q}}$$ **Equation 2-2**

where D_{min} is the minimum particle size in the mixture. Various other researchers used this model to optimise their concrete mixtures (Brouwers & Radix, 2005; Fennis & Walraven, 2012). By applying different q values, different types of concrete can be designed. Higher values of q lead to coarse mixtures and lower q values result in finer mixtures. Brouwers & Radix (2005) reported that a q value range of 0 to 0.28 would result in an optimal packing, while Yu et al. (2014) suggested a q value of 0.23 for the large amount of fine particles in UHPC mixtures. The mass proportions (%) of each individual material in the concrete mix are adjusted until the deviation between the target curve and the composed mix, expressed as the sum of squares of the residuals (*RSS*) at defined particle sizes, is minimised (see **Equation 2-3**) The composition of the concrete is then considered to be optimal.

$$RSS = \frac{\sum_{i=1}^{n} (P_{mix}(D_i^{i+1}) - P_{tar}(D_i^{i+1}))^2}{n}$$ **Equation 2-3**

where P_{mix} is the composed mix, the P_{tar} is the target grading calculated from **Equation 2-2** and n is the number of points (between D_{min} and D_{max}) used to calculate the deviation.

Figure 2-6 illustrates the ideal packing curves for a Fuller curve (**Equation 2-1**; $q = 0.5$), an Andreasen and Andersen particle packing model (**Equation 2-1**; $q = 0.37$) as well as Funk and Dinger's modified Andreasen and Andersen Particle Packing Model (**Equation 2-2**; $q = 0.37$). The maximum particle size is 32 mm and the minimum particle size is 63 µm. The figure shows that Funk and Dinger's modified Andreasen and Andersen Particle Packing Model takes larger and smaller particle sizes into account. The finer particles are better presented when considering Funk and Dinger's modified Andreasen and Andersen Particle Packing Model. This is in contrast to the Fuller curve. For the above-mentioned reason, it was concluded that the modified Andreasen and Andersen particle packing model is the best option for optimisation of the composition of granular materials. By adjusting the q value from 0.5 to 0.37, a finer ideal size distribution is observed. Thus, the assumption that a lower q value results in finer mixtures is valid.

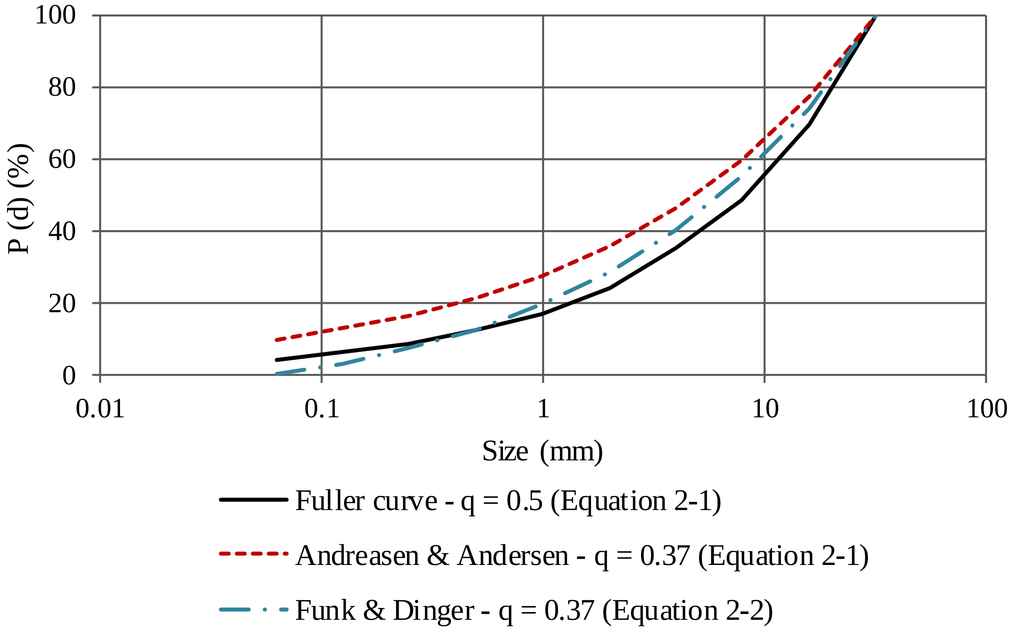

Figure 2-6: Ideal packing curves according to Fuller curve, Andreasen and Andersen Particle Packing Model (q = 0.37) and Funk and Dinger's modified Andreasen and Andersen Particle Packing Model for a maximum particle diameter of 32 mm and a minimum particle diameter of 63 µm (adapted from Fennis & Walraven, 2012)

The modified Andreasen and Andersen particle packing model was used by Yu et al. (2014) to optimise the UHPC matrix. Filler materials as well as binding materials should be included in the entire grading of the mix in order to achieve the densest possible packing. In order to obtain the best fit to the target curve as proposed by the modified Andreasen and Andersen particle packing model, the binder combinations and sand gradations should be adjusted. According to Yu et al. (2014), it is possible to produce UHPFRC with a dense granular structure and relatively low binder amounts (about 650kg/m^3) by using the modified Andreasen and Andersen optimum particle packing model. However, besides the proper design of the UHPC matrix, the effective application of steel fibres is also crucial and a practical method to successfully utilise steel fibres is still required (Yu et al., 2015b).

2.3.2 Response Surface Methodology

RSM is a well-known approach based on statistical and mathematical methods that assists in the analysis and optimisation of responses that are influenced by several variables (Montgomery, 2001; Aldahdooh et al., 2013; Ghafari et al., 2014). This technique ensures that valid results are effectively obtained with minimum effort, time and resources. RSM can shorten the experimental program, analyse interactions between mixture ingredients and provide optimal proportions to improve several responses in parallel (Ghafari et al., 2015b). The objective of RSM is the optimisation of the response. RSM has a variety of response surface designs that can be used. Central Composite Design (CCD) was used in this study. CCD is an augmented version of the factorial design with centre and axial points (Montgomery, 2001). CCD is useful in response surface modelling because it makes it possible to efficiently develop first-order and second-order models. To model curvature, a second-order model is required. **Equation 2-4** is the general form of the second order polynomials.

$$y = \beta_0 + \sum_{j=1}^{k} \beta_j x_j + \sum_{i<j} \sum_{i<j} \beta_{ji} x_i x_j + \sum_{j=1}^{k} \beta_{jj} x_j^2 + \epsilon$$

Equation 2-4

where $\sum_{j=1}^{k} \beta_{jj} x_j^2$ is the quadratic effect of a single variable, $\sum_{i<j} \sum_{i<j} \beta_{ji} x_i x_j$ is the interaction effect between two variables, β_0, β_i, β_{ii}, β_{ij} is the regression coefficients, x_i, x_j is the investigated factors, k is the number factors and ϵ is the random error. CCD consists of $2k$ axial points, 2^k factorial points and n number of centre runs. The number of independent variables is represented by k in this context. The three different types of points that define the region of interest for a two-factor design are illustrated in **Figure 2-7**. The factorial points are positioned on the corners of the square, the axial points are positioned a distance alpha (α) away from the centre point in the positive and negative sides of each axis and the centre points are positioned at the intersection of the two axes. Alpha (α) and the number of centre points specify whether a response surface design is rotatable. The response surface design has an improved quality of prediction when it is rotatable (α = ±1.414). RSM normally involves three phases. Phase one focusses on the experimental study, phase two develops the response surface models and phase three uses the statistical models for optimisation (Smit, 2015). The RSM approach was found to be efficient in predicting the performance of UHPC and effectively optimising the mixture ingredients (Aldahdooh et al., 2013; Ghafari et al., 2015a, 2015c).

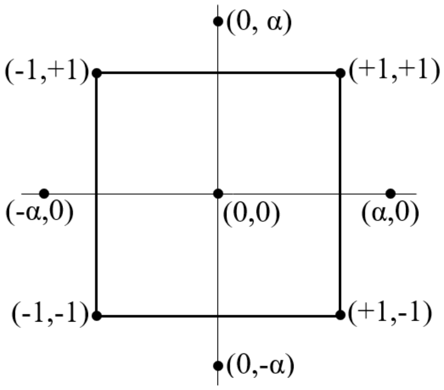

Figure 2-7: Central Composite Design for two variables

2.4 MIXING AND CASTING PROCEDURES

In a UHPC or UHPFRC mixture, the fineness of the filler particles is smaller compared to that of NSC. The uniform distribution of particles is important, especially the very fine particles, as very fine particles tend to agglomerate. According to Wille & Boisvert-Cotulio (2015), the key factor for attaining high particle packing density and improved material utilisation is to minimise particle agglomeration. In order to minimise particle agglomeration, Wille et al. (2011a) recommended mixing all the dry materials first (for five minutes) before adding the water and superplasticiser. Improved flowability can be obtained when gradually adding the superplasticiser (Pfeifer & Landgren, 1982; Tue et al., 2008), and not adding it all at once. Wille et al. (2011a) reported that only after approximately five minutes of adding the water and superplasticiser did the UHPC mixture become fluid. Fibres were then added during the following five minutes. Savino et al. (2019) stated that the use of an appropriate mixer is important to ensure that no fibre balling or honeycombing occurs.

The casting direction has no significant effect on the compressive strength of UHPC (Abbas et al., 2016). Steil et al. (2004) reported a difference of less than 2 % in compressive strength for UHPC cube specimens when loaded parallel and perpendicular to the casting direction. According to Steil et al. (2004), casting direction has no significant effect on the initial stiffness of UHPC beams subjected to bending. However, vertically cast beam specimens showed a decrease in flexural tensile strength compared to horizontally cast beam specimens due to the difference in fibre orientation (Steil et al., 2014). Fibre orientation for horizontally and vertically cast beams were perpendicular and parallel to the span of the beam, respectively. Yang et al. (2010) observed that the concrete pouring location is also a critical factor in achieving higher flexural tensile strength. Beams cast from the end of the mould experienced 16 % higher flexural tensile strength results compared to that of beams cast at the middle of the mould. Habel et al. (2008) reported a high scatter in results due to casting in different directions, which led to differences in the fibre distributions. According to Yu et al. (2017), two different casting methods are used to cast fresh UHPFRC:

1. Cast on one side of the mould to allow flowing process (see **Figure 2-8 (a)**), and
2. Cast randomly into the mould (see **Figure 2-8 (b)**).

The effect of different mixing procedures and casting directions on the mechanical properties falls outside the scope of this study and literature obtained was used as a guide for the mixing procedure as well as the casting directions used.

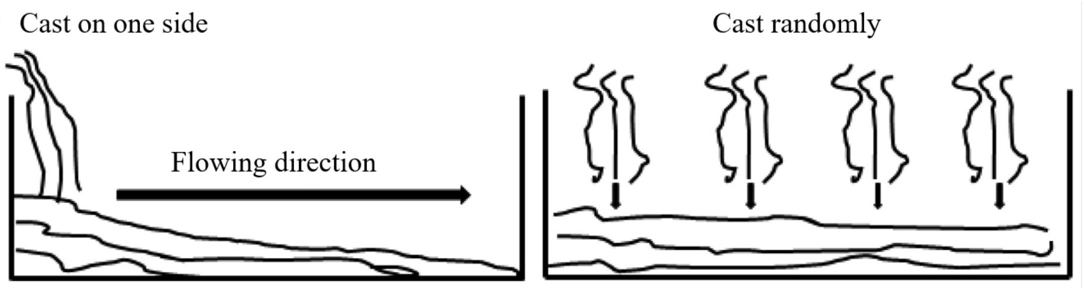

Figure 2-8: (a) Controlled casting and (b) random casting (adapted from Yu et al., 2017)

2.5 PRE-TREATMENT AND CURING PROCEDURE

The curing regime significantly influences the microstructure and mechanical properties of any concrete including UHPC (Shi et al., 2015; Kahanji et al., 2017). According to Prem et al. (2013), curing techniques play a major part in the full development of the concrete microstructure characteristics. The application of thermal curing on UHPC mixtures can increase the rate of hydration, advance the pozzolanic reactions which leads to the formation of additional calcium silicate hydrates (C-S-H) and thus, also increase early age strength development (Heinz & Ludwig, 2004; Habel et al., 2008; Müller et al., 2008; Soutsos & Kanavaris, 2018). Denser microstructures and higher mechanical properties are then obtained due to the C-S-H phases fitting into small pores (Collepardi et al., 1997; Fehling et al., 2004; Graybeal, 2006; Müller et al., 2008; Kahanji et al., 2017). According to Yoo et al. (2018), higher amounts of C-S-H and smaller pore sizes were observed for specimens that were steam-cured compared to that of the ambient-cured specimens.

Special curing regimes/techniques involve steam curing, hot water bath curing, hot air curing, autoclaving or compaction under high pressure (Shi et al., 2015; Hiremath & Yaragal, 2017b). These kinds of curing techniques are, however, expensive and unpractical to apply to bulk application (De Larrard & Sedran, 1994; Wille et al., 2012; Yoo et al., 2018), which then limit the wider use of UHPC (Shi et al., 2015). According to De Larrard & Sedran (1994), simple thermal curing (temperature rise) is feasible as well as available in ordinary precasting facilities. Hiremath & Yaragal (2017b) stated that thermal curing is used to decrease the curing time and increase the early age strength, which enables speedy construction. To shorten the construction time and accelerate the strength gain, UHPFRC should be cured in thermal curing conditions. The precast concrete industry requires high early age compressive strengths of up to 38 MPa at an age of 14 hours (Pfeifer & Landgreen, 1982). According to Yoo et al. (2018), curing UHPFRC under normal 25°C water conditions delays the construction period. However, looking at **Figure 2-9**, even though conventional water bath curing yielded the lowest strength, all four curing regimes can be used to reach 38 MPa after only 12 hours, which would be suitable for the precast industry. Nevertheless, special arrangements for thermal curing should be explored for use on construction sites and precast facilities (Abbas et al., 2016). Pfeifer & Landgren (1982) reported that thermal curing should start as soon as possible after the initial set time of the concrete to ensure optimum early-age and long-term strengths. However, Ahlborn et al. (2008) stated that UHPC attained compressive strength of over 200 MPa and modulus of elasticity of 55 GPa, regardless of when the thermal curing was applied. According to Prem et al. (2013), neither the physical nor the chemical structure of the hydration products was altered by a temperature of up to 45 °C.

According to Hiremath & Yaragal (2017b), curing for more than 12 hours is required to ensure complete hydration. The recommended heat curing applied to UHPC specimens range from 90 °C to 400 °C for 2 to 6 days (Richard & Cheyrezy, 1994; Heinz & Ludwig, 2004; Graybeal, 2006; Müller et al., 2008; Mahmud et al., 2013). However, Tracey et al. (2004) recommended that concrete should not be cured at temperatures higher than 60 °C. According to Heinz & Ludwig (2004), the application of heat curing raises a lot of questions regarding the negative effects thereof on the performance of UHPC components and their service life. Kahanji et al. (2017) suggested avoiding thermal curing as it may increase the brittleness of the concrete.

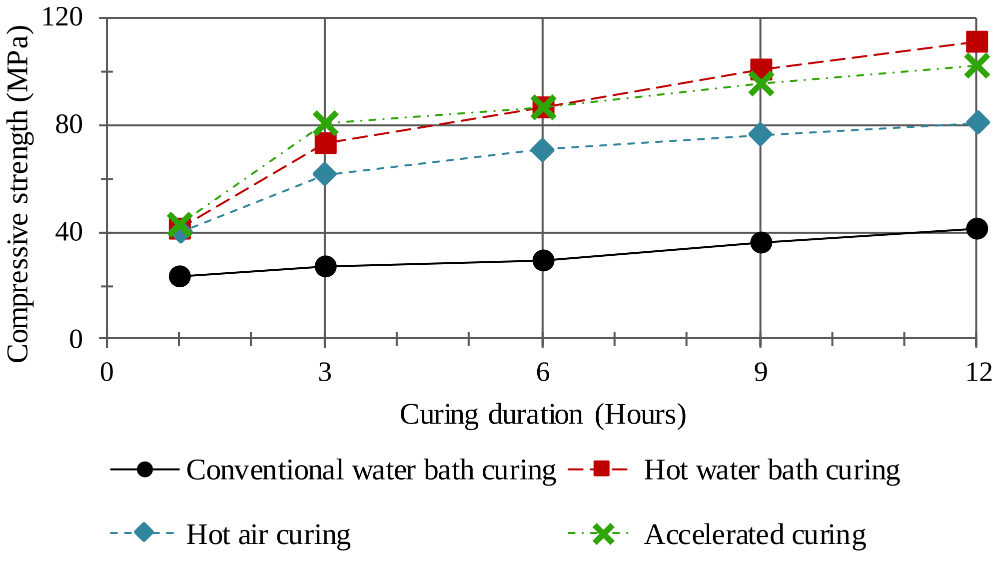

Figure 2-9: Early-age compressive strength variation of UHPC for different curing regimes (adapted from Hiremath & Yaragal, 2017b)

2.6 MICROSTRUCTURAL PROPERTIES

According to Aïtcin (2000), SEM have been a key factor in the progress achieved to better understand the microstructure of concrete. Macrostructural properties are linked to the microstructural properties (Müller et al., 2008). Hiremath & Yaragal (2017b) state that an important requirement in cementitious compositions is a quantitative understanding of C-S-H products. As mentioned earlier, C-S-H products are an important aspect of strength development in UHPC. They represent up to 70 % of the fully hydrated UHPC paste. Cheyrezy et al. (1995) state that the microstructure of UHPC depends on the heat curing condition applied before and during setting and that an increase in temperature changes the microstructure of C-S-H hydrates. The arrangement of these hydrated products in the microstructure is different for different curing regimes (Hiremath & Yaragal, 2017b).

2.6.1.1 Delayed Ettringite Formation

Ettringite ($C_6AS_3H_{32}$) forms during the initial hydration stage (Heinz & Ludwig, 2004) and is a strength-reducing compound. As the curing period continues, ettringite compounds become smaller and ultimately disappear. Ettringite particles have the appearance of small needle-like structures. According to Heinz & Ludwig (2004), it is well known that curing temperature above 70 °C can cause Delayed Ettringite Formation (DEF) as a disruptive process during the service life of the concrete. This late formation produces forces that can lead to expansive distress, cracking of the concrete and reduced strength. The expansion normally occurs after 1 to 4 months under laboratory conditions. Conventional concrete experiences expansion only when there are stages of adequate water intake through direct water contact (Heinz & Ludwig, 2004). Lower w/b ratios lead to dense microstructure with low porosity. This prolongs the initiations of DEF. Heinz et al. (1999) state that with w/c ratio of as low as 0.4, DEF only started after two years where samples were heat treated at 90 °C and thereafter stored in a water bath.

Figure 2-10 illustrates results obtained by Tracey et al. (2004). The graph shows that the twenty-eight-day compressive strength decreases with an increasing curing temperature for different mix designs. All specimens exhibited expansion after being exposed to temperatures higher than 65 °C (Tracey et al., 2004). This was attributed to DEF. It is useful to limit the temperature to 65 °C during the hydration process to ensure DEF in hardened concrete is avoided (*fib* Model Code 2010, 2013).

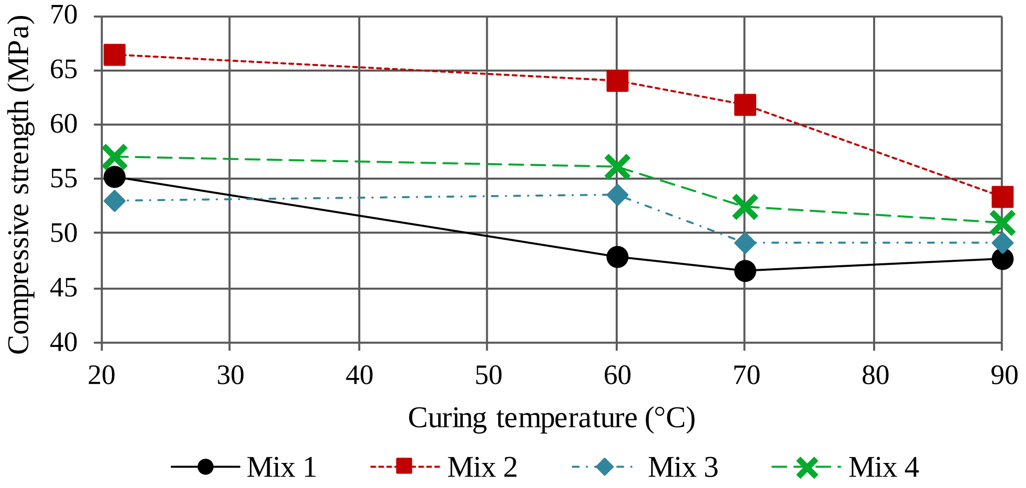

Mix 1: Cement = Type III; 11 % C_3A; Blaine fineness = 555 m^2/kg

Mix 2: Cement = Type III; 9 % C_3A; Blaine fineness = 566 m^2/kg

Mix 3: Cement = Type I; 7 % C_3A; Blaine fineness = 410 m^2/kg

Mix 4: Cement = Type III; 7 % C_3A; Blaine fineness = 514 m^2/kg

Figure 2-10: Twenty-eight-day compressive strength results with different curing temperatures for four different mixture designs (adapted from Tracey et al., 2014)

2.6.1.2 Phase Composition

Cement phase composition and the effect of heat curing was investigated by Heinz & Ludwig (2004) by using X-Ray Diffraction (XRD). The relative changes in phase composition caused by different heat-treatments are shown in **Figure 2-11** (C_2S, C_4AF, monosulphate, calcite included but not shown).

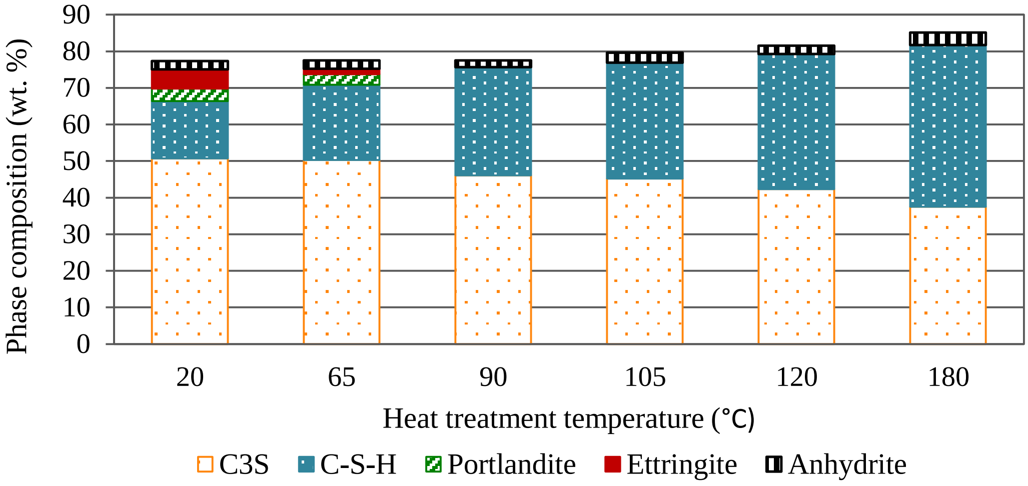

Figure 2-11: Phase composition of hardened UHPC that was heat treated at various temperatures (adapted from Heinz & Ludwig, 2004)

The ettringite phase can only be seen for samples cured at 20 °C and 65 °C. However, the data shown was tested on twenty-eight-day samples and, as stated earlier, DEF in UHPC can start as late as 4 months after casting. The graph also indicates that all specimens still contained high quantities of unhydrated clinker (phases C_3S, C_2S, C_4AF). The amount of unhydrated clinker did, however, reduce with an increase in heat curing temperature.

2.7 FRESH PROPERTIES

2.7.1 Flowability

According to Wille et al. (2012), increased flowability/workability is one of the most important conditions to achieve an UHPC. The low w/b ratio, reduced flowability and the effect of steel fibres are some of the problems that exist during the casting and handling of UHPC. The consistency of UHPC at low w/b ratios is influenced by the choice of cement, cement content, additions, water dosage and admixtures (Droll, 2004; Aldahdooh et al., 2013). Yu et al. (2014) state that workability of UHPC can be influenced by frictional or cohesive forces between the fibre and concrete matrix. Mixtures containing fibres with a smaller aspect ratio are more workable than mixtures containing fibres with a larger aspect ratio, even at higher fibre dosages (Wille et al., 2011a). Habel et al. (2008) reported that the introduction of steel fibres in the UHPC mix significantly reduced the flowability. This is shown in **Figure 2-12,** which clearly indicates that the relative slump flow value of UHPC mixes decreases linearly with the addition of steel fibres (this is true for all three mix designs). Bindiganavile et al. (2002) reported that a slump of 200 mm, before fibre addition, dropped to 120 mm after fibre addition. Fibre orientation is controlled by the flowability of the concrete, which in effect influences the mechanical properties (Zhou & Uchida, 2017). As stated earlier, the inclusion of cement replacement materials in UHPC can lead to significantly improved workability and this can be seen in **Figure 2-12**. Mixes with a higher cement content, meaning that less filler materials were utilised, show a reduced flowability. The appropriate utilisation of filler materials is thus required to improve the workability of UHPC. This should be treated as an effective method to reduce the negative influence of the addition of steel fibres in the concrete matrix (Yu et al., 2014). Wille & Boisvert-Cotulio (2015) reported that, due to the smaller total surface area of coarse aggregates, UHPC matrices containing coarse aggregates required less water to attain similar spread values in comparison to UHPC matrices containing only fine aggregates. UHPC mixtures containing no coarse aggregate showed better flow compared to mixtures containing coarse aggregate (Orgass & Klug, 2004). Fennis & Walraven (2012) stated that high particle packing density improved flowability of concrete mixtures. The strategy proposed by Wille et al. (2011a) to decrease the effort required to cast UHPC materials, is to first increase the particle packing of the mixture ingredients and then to improve the flowability.

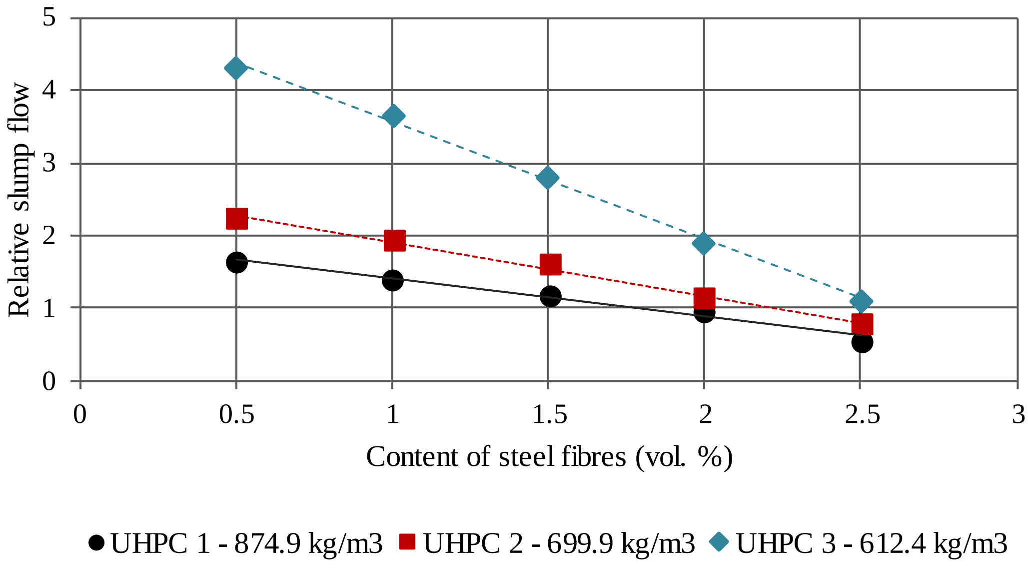

Figure 2-12: Variation of the relative slump flow of UHPFRC with different cement content as a function of steel fibre content (adapted from Yu et al., 2014)

2.7.2 Air content

Higher w/b ratio and superplasticiser dosages tend to increase the air content in UHPC mixture (Abbas et al., 2016). Compressive strength decreases with an increase in air content. According to Ingo et al. (2004), the total air content is highly dependent on the mixer used, for example, laboratory mixers with higher mixing speed lead to a sticky consistency of the paste and, as a result, increase the air content. Delayed addition of superplasticiser also decreases the viscosity of the mixture and reduces the air content (Tue et al., 2008). Air content in UHPC mixtures range from 0.3 % to 5.4 % (Ingo et al., 2004; Wille et al., 2011a; Magureanu et al., 2012; Abbas et al., 2016). According to Domone & Illston (2010), it is assumed that strength of concrete could be reduced by 5.5 % for each 1.0 % of air. With an increased air content, slump as well as the density of the concrete reduces.

2.7.3 Setting time

According to Habel et al. (2016), setting time can be defined as the time when the mixture attains a stiffness of 1 GPa and autogenous shrinkage starts. In general, the setting time of UHPC ranged from 6 hours to 12 hours depending on the mixture design (Yoo et al., 2013). Other studies also show that the setting time can be delayed for up to 40 hours due to the set retarding effect of high superplasticiser dosages and surface covering (Yoo et al., 2013). Delays in setting time could affect the early age strength development to such an extent that demoulding has to be delayed for days, which would have a significant cost implication as far as the number of moulds required in a factory is concerned. Setting time falls outside the scope of this study.

2.8 MECHANICAL PROPERTIES

UHPC is of interest not only for the enhanced mechanical strength, but also for the higher elastic modulus, lower creep and shrinkage, better durability, higher tensile strength and elastic post-cracking strength (De Larrard & Sedran, 1994; Filho et al., 2012; Magureanu et al., 2012; Habert et al., 2013; Mahmud et al., 2013). The addition of steel fibre in UHPC improves the tensile strength, flexural strength, ductility and durability performance (Habel et al., 2008; Magureanu et al., 2012; Astarlioglu & Krauthammer, 2014; Afroughsabet et al., 2016; Hiremath & Yaragal, 2017b). An increase in the mechanical properties is observed with an increase in fibre dosage (Abbas et al., 2015). Due to the improved mechanical properties and durability of UHPC, structures can be cast to be more slender when compared to NSC. Although the enhanced mechanical properties and durability of UHPC are very attractive for design purposes, the use of various element sizes might influence these properties. The size effect on mechanical properties, behaviour and structural strength of UHPC still requires further investigation (Mahmud et al., 2013; Nguyen et al., 2013)

2.8.1 Compressive strength

UHPC is defined by various researchers as concrete with a minimum specified compressive strength of 150 MPa with specified durability, tensile strength and toughness requirements (Fehling et al., 2004; Magureanu et al., 2012; Schmidt et al., 2012; Prem et al., 2013; Yoo et al., 2018). Fibres are usually required to achieve specified requirements. Extremely low w/b ratios and high cement contents are used in order to increase the compressive strength. Strength is, without any doubt, the most important single property of concrete since most concrete structures are designed for and must be capable of carrying imposed loads. Domone & Illston (2010) describe many factors that may have an influence on the strength of concrete. According to Abbas et al. (2016), the curing regime and fibre content are the main factors that influence the mechanical properties of UHPC. Although extensive research has been done on UHPC and its composition, obtaining compressive strengths of over 150 MPa without special treatment such as heat curing and/or special vibration, has been challenging (Wille et al., 2011a). This can be attributed to the large array of influencing parameters such as properties and the particle size of materials used, mixture proportioning, mixing procedures, specimen preparation and test method. It is crucial to design concrete mixtures that maintain or increase their twenty-eight-day compressive strength over the life of the structure (Aïtcin, 2000). Abbas et al. (2015) reported an average increase of 6 % in the fifty-six-day compressive strength compared to that at twenty-eight-days, due to continuous hydration of pozzolanic cementitious materials at a later age (see **Figure 2-13**). The increase in fibre content, from 3 % to 6 %, only caused a 4 % increase in compressive strength after twenty-eight days. This difference was deemed insignificant. Reducing steel fibre content is crucial in reducing the unit cost. From the graph, it was concluded that a steel fibre content of 3 % yielded adequate compressive strength. The twenty-eight-day compressive strength results obtained from various studies with similar specimen size and test set-up is tabulated in **Table 2-2**. The data confirms that various parameters influence the compressive strength of UHPC.

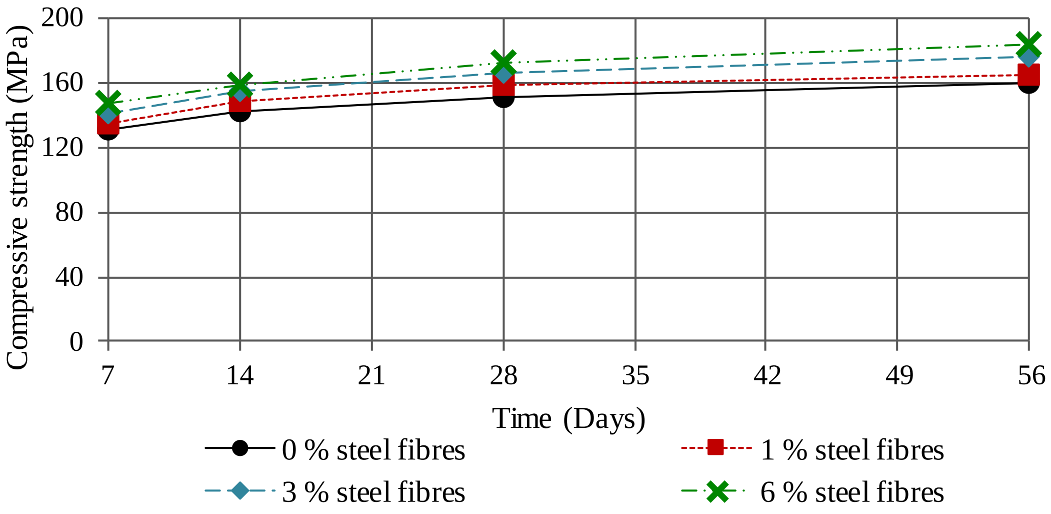

Figure 2-13: Effect of steel fibre dosage (L/D = 12/0.20) on the compressive strength development of UHPC (adapted from Abbas et al., 2015)

2.8.1.1 Effect of steel fibres

El-Dieb (2009) observed that the addition of steel fibres to the UHPC matrix changes the mode of failure of UHPC specimens. The specimens can remain intact with somewhat ductile behaviour. Some studies reported that the addition of high dosages of steel fibres have no influence on the compressive strength of UHPC (Reda et al., 1999; Schmidt et al., 2003). However, other studies show that the compressive strength increases with an increasing fibre dosage (Abbas et al., 2015; Savino et al., 2019). When proper heat curing is applied, a slight increase can be observed in compressive strength due to the addition of fibres (Bonneau et al., 1997; Soutsos et al., 2005; Jun et al., 2008). The effect of steel fibre dosage and length on the twenty-eight-day compressive strength is illustrated in **Figure 2-14**. The graph illustrates that fibre length had no significant influence on the compressive strength. The variability between the compressive strength of the different fibre lengths is more prominent with higher fibre dosages. No significant difference can be observed in the compressive strength with the addition of higher dosages of steel fibres. This confirms the findings of Reda et al. (1999) and Schmidt et al. (2003).

Table 2-2: Twenty-eight-day compressive strength results obtained from various studies

Compressive strength (MPa)		w/b ratio	Steel fibre content (vol %)	Binders (kg/m^3)		Reference
± 25 °C	Thermal curing			Cement	Filler material	
140.8	212.4	0.17	-	850	140	Müller et al. (2008)
101.6	213.4	0.13	-	650	210	Müller et al. (2008)
133.7	157.3	0.20	1 %	799.5	199.9	Yoo et al. (2018)
-	150.6	0.15	2 %	657.0	537.0	Hassan et al. (2012)
-	181.4	0.18	6 %	720.5	214.3	Aldahdooh et al. (2013)

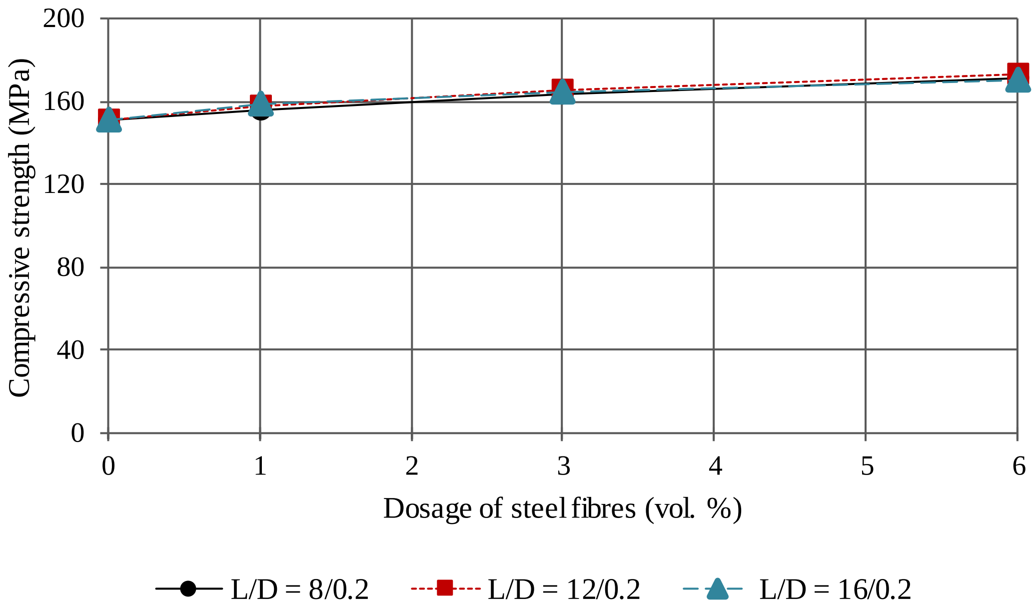

Figure 2-14: Effect of steel fibre dosage and length on the twenty-eight-day compressive strength of UHPC (adapted from Abbas et al., 2015)

2.8.1.2 Effect of specimen size

According to Abbas et al. (2016), specimen size has a significant effect on the measured compressive strength for UHPC (see **Table 2-3**). This can be attributed to the higher probability of larger size flaws in larger concrete specimens (Graybeal, 2006; Ahlborn et al., 2008) and the effect of confinement of the testing machine platens (Graybeal & Davis, 2008; Kazemi & Lubell, 2012). According to Kazemi & Lubell (2012), a conversion factor of 1.09 can be used when considering 50 mm cube specimens to 100 mm cube specimens (50/100) when working with UHPC.

Table 2-3: Effect of specimen size on the compressive strength of UHPC (Kazemi & Lubell, 2012)

Fibre content (%)	Specimen size (mm)	Compressive strength (MPa)
0.0	100 x 100 x 100	127.5
	50 x 50 x 50	139.0
2.0	100 x 100 x 100	144.0
	50 x 50 x 50	150.0
4.0	100 x 100 x 100	144.0
	50 x 50 x 50	165.5

2.8.1.3 Effect of pre-treatment

According to Wille et al. (2011a), in order to attain compressive strengths of more than 150 MPa, a treatment, such as heat curing or pressure or extensive vibration, is normally needed. Wille et al. (2011a) acknowledge that the development of concrete with a compressive strength of more than 150 MPa, without heat or pressure treatment, is an obstacle due to a large group of determining factors. These include not only the mixture proportions, but also mixture composition, mixing procedure and test methods (Hwang et al., 2012). An average increase in compressive strength of 40 % was observed for specimens cured in a 90 °C heat curing compared to untreated control specimens (Bonneau et al., 1997; Soutsos et al., 2005; Yoo et al., 2018). According to De Larrard & Sedran (1994), the seven-day compressive strength of concrete increased from 121 MPa to 236 MPa by changing the curing regime from normal 25 °C water curing to thermal curing at 90 °C for four days. From **Figure 2-15,** it can be observed that UHPC samples cured under thermal curing conditions show a significant increase in early-age strength development compared to the ambient and water cured UHPC samples. The early-age strength obtained for the thermally cured samples reached a strength equal to that of the twenty-eight-day strength of the conventional curing regime samples, namely, ambient air curing and water curing. There is no significant difference in strength development results for the conventional curing regimes. The long-term effect of the thermal curing was, however, not investigated and the strength results were only tested up until seven days.

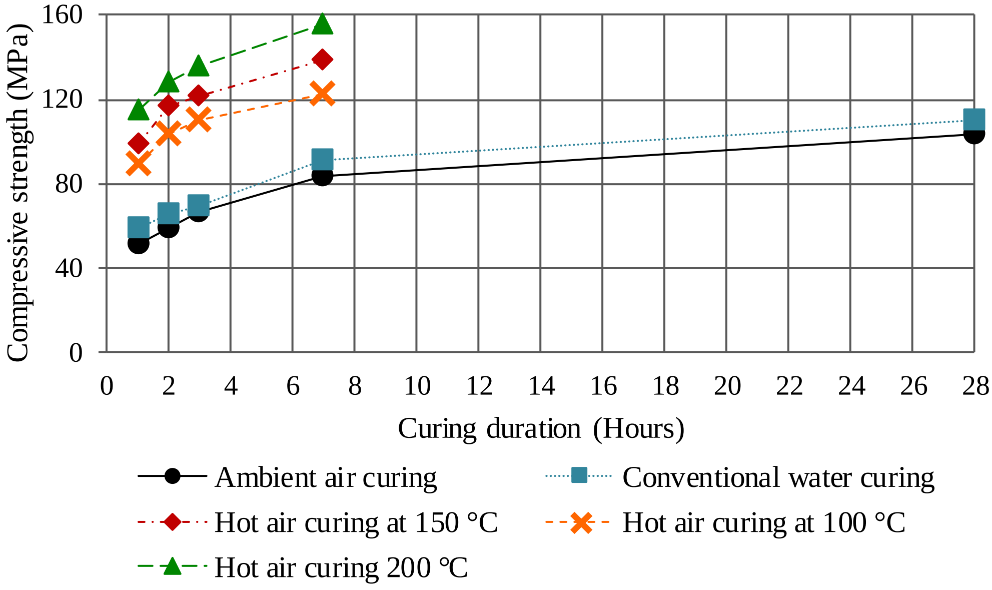

Figure 2-15: Compressive strength variation of UHPC for different curing regimes (adapted from Hiremath & Yaragal, 2017)

Long-term strength tests are required for samples cured under thermal curing conditions to evaluate the long-term effects on strength development. Kahanji et al. (2017) observed that the compressive strength for hot cured specimens peaked at twenty-eight days, whereas the compressive strength for the cold cured specimens continued to increase. Ahlborn et al. (2008) state that UHPC attained compressive strength of over 200 MPa regardless of when the thermal curing was applied (see **Figure 2-16)**. The thermally cured specimens show no significant strength gain after curing, even when the thermal curing was delayed. The compressive strength of ambient air cured samples showed significant strength development as they continued to cure.

The long-term strength development rate for conventional cured specimens is higher compared to the specimens cured in hot water (Kahanji et al., 2017). This was also confirmed by Yoo et al. (2018), who observed that the compressive strength development for ambient cured specimens increases with age, whereas no increase was observed for the thermal cured specimens. Kang et al. (2017) stated that specimens that experienced a 90 °C heat curing tended to maintain or decrease their strength after twenty-eight-days. According to Pfeifer & Landgren (1982), curing methods must be able to maintain a high early-age and long-term compressive strength, while utilising less energy. Tracey et al. (2004) observed that specimens cured at an elevated temperature (90 °C) yielded lower compressive strength results compared to that of specimens cured at conventional curing temperatures (21 °C). Wille et al. (2011a) developed a concrete mix design by using commercially available materials while still achieving strength in excess of 200 MPa without any special heat or pressure treatment. Domone & Illston (2010) state that a higher temperature maintained throughout the life of a concrete specimen will result in higher short-term strengths, but lower long-term strengths. Soutsos & Kanavaris (2018) reported that high early age curing temperatures have a negative effect on the long-term strengths of concrete. According to Kahanji et al. (2017), contradicting literature makes it difficult to compare different curing regimes and their influence on mechanical properties.

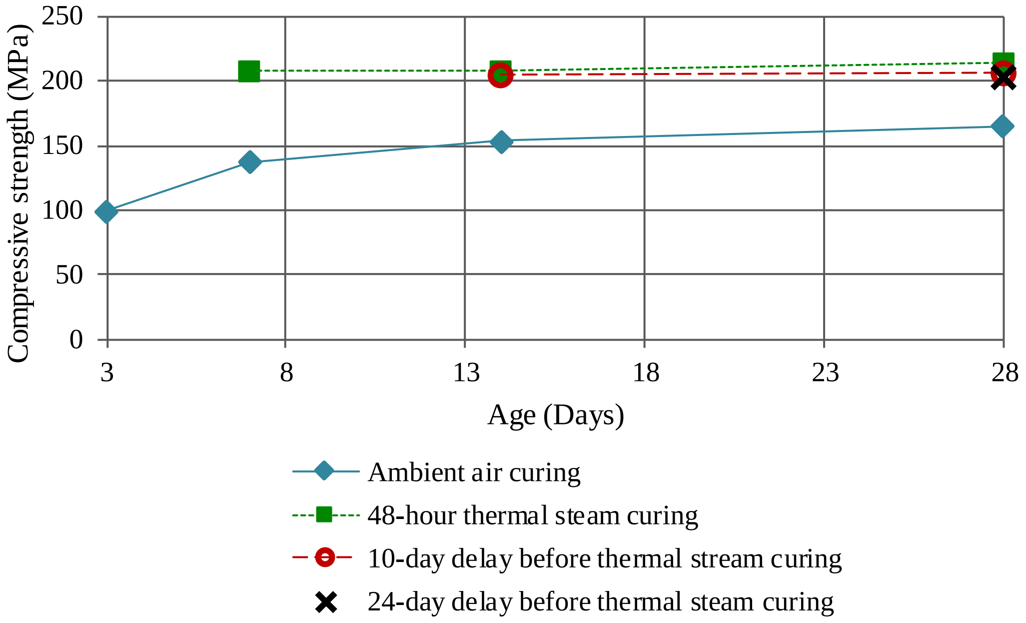

Figure 2-16: Effect of timing of thermal curing on the compressive strength of UHPC specimens (adapted from Ahlborn et al., 2008)

2.8.2 Modulus of elasticity

The modulus of elasticity is the relationship between stress and strain and is also known as Young’s modulus. The elastic modulus of concrete is a function of many variables, including type and amounts of the ingredients used in making the concrete as well as the manner and duration of curing the concrete, age at the time of loading, rate of loading and other factors. According to Afroughsabet et al. (2016), the density, modulus of elasticity of the primary ingredients and the characteristics of the transition zone determine the modulus of elasticity for heterogeneous materials such as concrete. Some researchers reported that the addition of steel fibres in the UHPC matrix cause an increase in the modulus of elasticity, while other researchers did not agree (Bonneau et al., 1996; Hassan et al., 2012; Abbas et al., 2016). The twenty-eight-day modulus of elasticity ranged from 45 GPa to 52 GPa, depending on the UHPC mixture constituents (Vicenzino et al., 2005; Meng et al., 2017). Abbas et al. (2015) reported an increase of 8 % in the fifty-six-day modulus of elasticity compared to that at twenty-eight days, due to continuous hydration of pozzolanic cementitious materials at a later age.

2.8.2.1 Effect of steel fibres

No significant influence was observed in the modulus of elasticity when fibres were added (Abbas et al., 2015). Bonneau et al. (1996) reported a 7 % increase in the modulus of elasticity when 2 % by mixture volume of steel fibres were added compared to that of the control specimen without fibres.

2.8.2.2 Effect of pre-treatment

Richard & Cheyrezy (1994) reported that the modulus of elasticity increased from 57 GPa to 70 GPa when specimens were subjected to heat curing and, therefore, it can be said that the modulus of elasticity is a function of heat curing. However, Ahlborn et al. (2008) state that there is no significant difference between the modulus of elasticity regardless of curing regime or when curing is applied (see **Figure 2-17**).

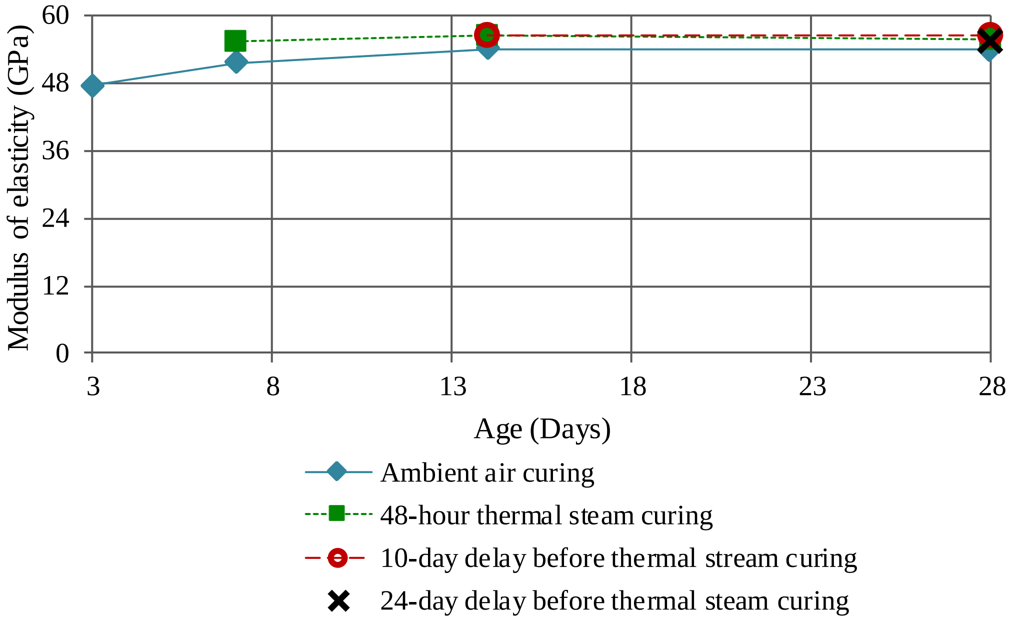

Figure 2-17: Effect of timing of thermal curing on the modulus of elasticity of UHPC specimens (adapted from Ahlborn et al., 2008)

2.8.3 Direct tensile strength

Figure 2-18 illustrates the typical stress-displacement curve of UHPFRC tested in direct tension. The first peak stress (σ_{cr}) corresponds to the cracking process and σ_{pr} is the post-peak strength. The value δ_{cr} in the graph represents the displacement corresponding to the matrix strength, δ_0 is the value when the separation of the matrix specimen into two halves occurs, δ_{pc} is the displacement corresponding to the post-peak strength and δ_f is the maximum displacement that causes pull-out of the fibres.

According to Cadoni et al. (2019), UHPC can be classified as:

- strain-hardening when $\sigma_{pr} \geq \sigma_{cr}$
- strain-softening when $\sigma_{pr} < \sigma_{cr}$

Cadoni et al. (2019) state that UHPFRC is normally categorised as a function of its tensile behaviour (strain-hardening or strain-softening) depending on whether the stress increases or decreases after the first crack occurs. Strain-hardening behaviour is characterised by UHPFRC's ability to continue to increase in tensile capacity due to multiple cracking and beneficial fibre orientation, whereas strain-softening behaviour is where fibres continue to transfer forces across the crack while avoiding brittle failure, which lead to gradual post-peak strength reduction (Wille et al., 2011b; Cadoni et a., 2019). A major factor leading to improved ductility and energy dissipation is the development of multiple cracks. High content of fibres may enhance the tensile strength beyond the matrix strength, but this is conditioned by the shape of the fibres as well as by their distribution and orientation.

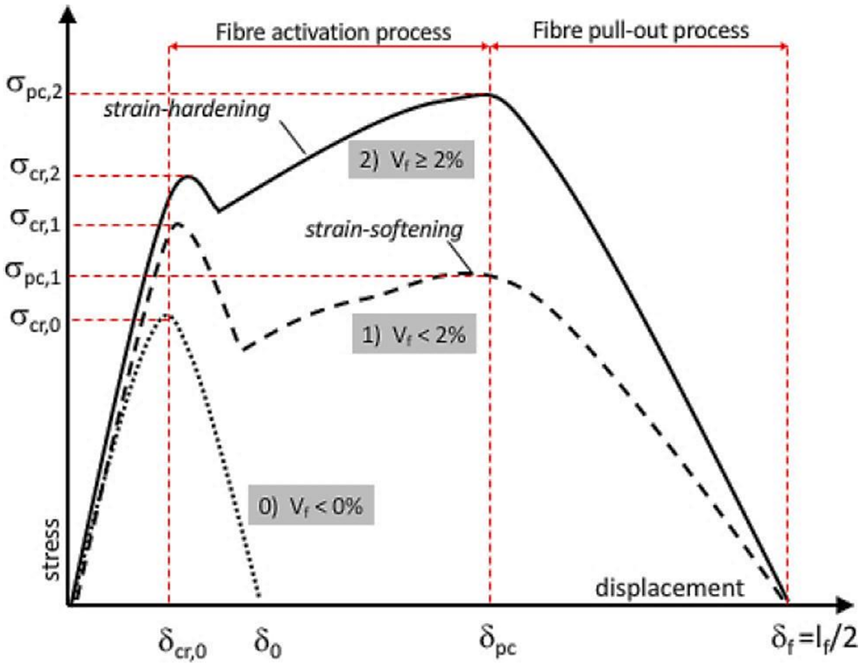

Figure 2-18: Behaviour of UHPFRC in direct tension (Cadoni et al., 2019)

Twenty-eight-day direct tensile strength results obtained from various studies are tabulated in **Table 2-4**. A direct tensile strength range of 9 MPa to 17 MPa is observed for UHPFRC, depending on the w/b ratio, fibre content and curing regime.

Table 2-4: Twenty-eight-day direct tensile strength results obtained from various studies

Direct tensile strength (MPa)		w/b ratio	Steel fibre content (vol %)	Binders (kg/m^3)		Reference
± 25 °C	Thermal curing			Cement	Filler material	
14.9	16.9	0.2	1 %	799.5	199.9	Yoo et al. (2018)
-	9.07	0.15	2 %	657.0	537.0	Hassan et al. (2012)
-	12.5	0.18	6 %	720.5	214.3	Aldahdooh et al. (2013)

2.8.3.1 Effect of steel fibres

Wille et al. (2011b) reported a direct tensile strength of 20 MPa when using 3% (volume fraction) small diameter, high strength, short, smooth steel fibres. Other researchers reported a direct tensile strength range of 7 MPa to 17 MPa (Behloul et al., 1996; Habel et al., 2008; Yoo et al., 2018). Hassan et al. (2012), stated that the tensile strength of UHPFRC was almost double that of UHPC (see **Figure 2-19**).

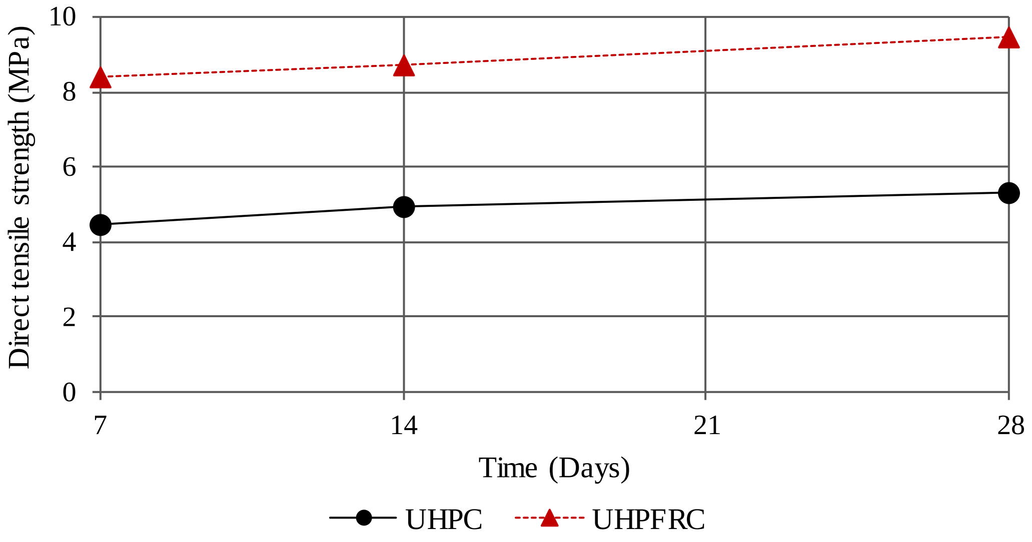

Figure 2-19: Effect of fibre on the direct tensile strength development (adapted from Hassan et al., 2012)

2.8.3.2 Effect of pre-treatment

An average increase in direct tensile strength of 49 % was observed for specimens cured in a 90 °C heat treatment compared to untreated control specimens (Yoo et al., 2018). Hassan et al. (2012) reported that UHPC reached its ultimate strength within seven days due to thermal curing and that no significant difference in strength was observed between seven days and twenty-eight days. Yoo et al. (2018) observed that the direct tensile strength development for ambient cured specimens increases with age, whereas no increase was observed for thermal cured specimens.

2.8.4 Splitting tensile strength

According to Abbas et al. (2015), the splitting tensile strength of UHPC increased with an increase in curing time and the addition of steel fibres significantly increased the splitting tensile strength (EL-Dieb, 2009). The splitting tensile strength increased as the steel fibre volume increased, indicating a more ductile failure (see **Figure 2-20**). The graph also illustrates that fibre length considerably influences the splitting tensile strength. UHPC mixtures incorporating short steel fibres (8 mm) show higher splitting tensile strength compared to mixtures incorporating longer steel fibres (12 mm and 16 mm). The difference in splitting tensile strength due to fibre length is more prominent with higher fibre dosages. Splitting tensile strength of UHPC ranges between 9 MPa and 40 MPa, depending on the mixture composition and type of fibres used (Bindiganavile et al., 2002; Abbas et al., 2015).

According to Olesen et al. (2006), the standard configuration for the splitting tensile test cannot be used to obtain the tensile strength of fibre reinforced concrete due to the ductility of the material. Denneman (2011) developed an adjusted tensile splitting test procedure to obtain a close estimate of the true tensile strength for concrete containing fibre reinforcement. The limit between linear elastic pre-crack behaviour and the ductile post crack behaviour is found by monitoring transversal deformation perpendicular to the load direction during the test. Rocco et al. (1999) found that the primary mode of failure (shown in **Figure 2-21 (a)**) is followed by secondary cracking (shown in **Figure 2-21 (b)**). According to Denneman (2011), after the tensile strength of the material is reached and the first crack has formed in the centre of the specimen (along the axis), the stresses redistribute and new highly stressed areas appear. Rocco et al. (1999) found that both the principal crack formation and secondary crack formation have a peak as shown in **Figure 2-22**. This can be found by measuring the transversal deformation during testing. The material type and specimen geometry would influence the position of the peaks. In a situation where the secondary peak load exceeds the principal peak load, the tensile strength recorded in the conventional splitting test method would be that of the secondary peak load. This would be the only value that would be recorded.

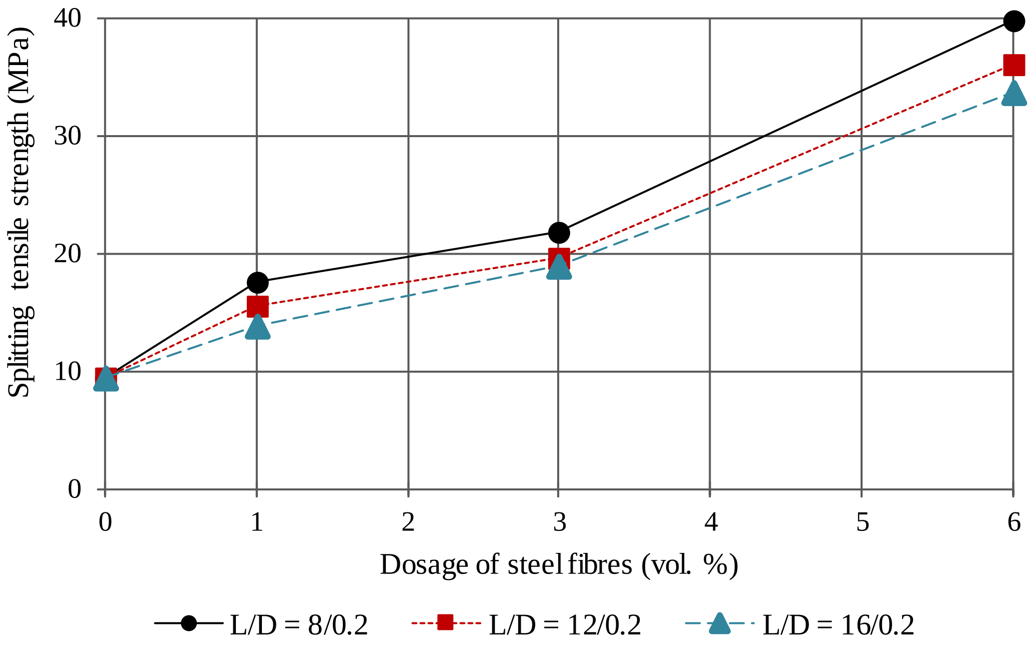

Figure 2-20: Effect of steel fibre dosage and length on the splitting tensile strength of UHPC (adapted from Abbas et al., 2015)

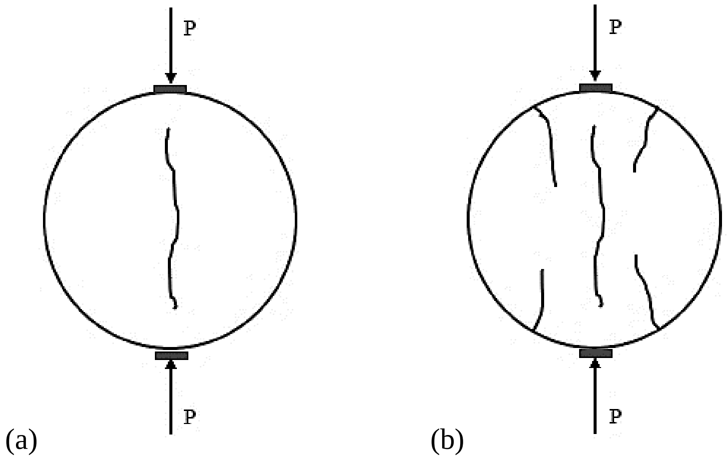

Figure 2-21: (a) Principal crack formation and (b) Secondary crack formation (adapted from Denneman, 2011)

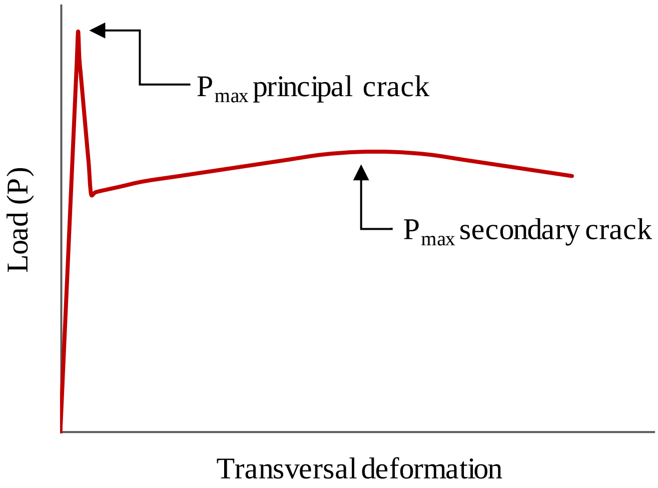

Figure 2-22: Schematic load-deformation curve (adapted from Denneman, 2011)

2.8.5 Flexural tensile strength

UHPFRC shows high flexural tensile strength and toughness due to the improved microstructural properties of the concrete matrix, dense particle packing and steel fibre addition (Vicenzino et al., 2005; Kim et al., 2008). The typical load-deflection behaviour of UHPFRC is shown in **Figure 2-23** (equivalent bending stress versus normalised deflection by span length). The Limit of Proportionality (LOP) was defined as the limit of the linear elastic region (Nquyen et al., 2013). This was defined by Yu et al. (2015b) as the point where initial cracking occurred (point A). Modulus of Rupture (MOR) was defined by Nguyen et al. (2013) as the point where maximum equivalent bending stress occurs. Yu et al. (2015b) described this as the point where the peak load occurs (point B). In this case, f_{MOR} is greater than f_{LOP} and, therefore, strain hardening behaviour occurred. The limit of proportionality of UHPFRC ranges between 15 MPa and 25 MPa (Vicenzino et al., 2005). **Table 2-5** shows twenty-eight-day flexural tensile strength results obtained from various studies with similar fibre types. UHPFRC mix designs with lower binder contents seem to be comparable to non-optimised UHPFRC mix designs which have higher binder contents. Habel et al. (2008) used the assumption of a linear-elastic stress state to determine the flexural tensile strength even though the stress state in UHPFRC after cracking would be highly nonlinear. The flexural tensile strength value does not reflect the reality but allow a comparison between different types of UHPFRC (Habel et al., 2008). The other references did however not state whether a linear-elastic stress state was assumed. Filho et al. (2012) reported a twenty-eight-day limit of proportionality of 18.2 MPa and a twenty-eight-day flexural tensile strength of 23 MPa which corresponds to Meng et al. (2017), who obtained a twenty-eight-day flexural tensile strength of 21 MPa. Filho et al. (2012)

reported enormous ductility when testing UHPFRC specimens. He observed strain softening behaviour after reaching the peak load. Habel et al. (2008) stated that fibre content and fibre distribution related to casting method and experimental set-up as well as the procedure used to characterise the materials, all influence the flexural tensile strength results obtained.

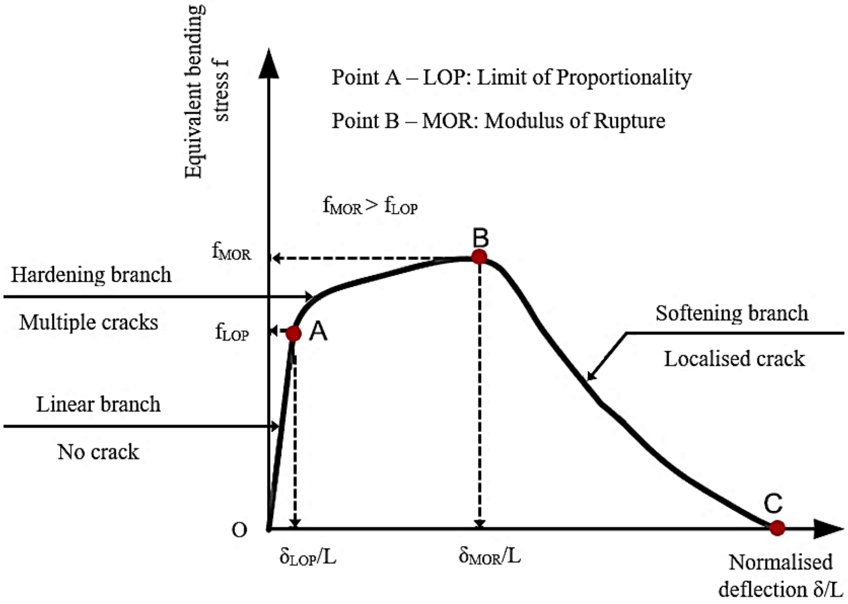

Figure 2-23: Typical load-deflection behaviour of UHPFRC (adapted from Nguyen et al., 2013)

Table 2-5: Flexural tensile strength results obtained from various studies

Flexural tensile strength (MPa)		w/b ratio	Steel fibre content (vol %)	Binders (kg/m^3)		Reference
± 25 °C	Thermal curing			Cement	Filler material	
23.0	-	0.15	2.0 %	1011	58.0	Filho et al. (2012)
21.3	-	0.16	2.0 %	663.0	409.0	Meng et al. (2017)
21.5	-	0.20	2.0 %	594.2	290.1	Yu et al. (2015b)
22.5	-	0.20	5.0 %	1087	163.0	Habel et al. (2008)
24.0	-	0.20	5.5 %	967.0	251.0	Habel et al. (2008)
-	30.3	0.18	6.0 %	720.5	214.3	Aldahdooh et al. (2013)

Yu et al. (2015b) stated that the toughness properties of UHPFRC are of great importance for UHPFRC elements exposed to a large energy release or impact loading rates. The dimensions of the specimen tested will influence the flexural toughness since it will influence the total flexural load the specimen can carry (Soutsos et al., 2012). Two standards are mainly used to determine the flexural toughness of UHPFRC, namely, ASTM C1018-97 and JSCE SF-4. However according to Yu et al. (2015b), the JSCE-SF4:1984 standard is more suitable to evaluate the flexural toughness of UHPFRC than ASTM C1018-97. Flexural toughness is defined as the area below the load-deflection curve up to a deflection of span/150 (δ_{tb}) as shown in **Figure 2-24** (JSCE-SF4:1984). Soutsos et al. (2012) obtained a maximum flexural toughness value of 80 Nm for 38 MPa fibre reinforced concrete with 50 kg/m^3 of hooked end steel fibres with a length of 60 mm.

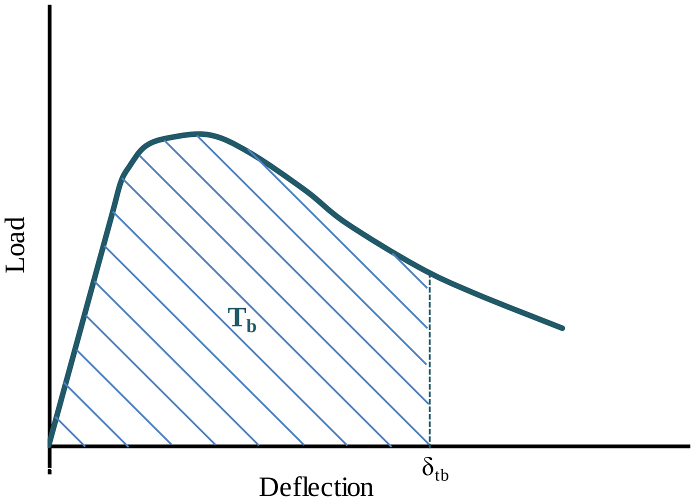

Figure 2-24: Flexural toughness (adapted from JSCE-SF4:1984)

During a flexural tensile strength test, the measured deflection of the UHPC specimens contains both deflection due to moment (δ_M) and deflection due to shear (δ_V) (Elsaigh, 2007; Nguyen et al., 2013). The effect of shear deflection is usually relatively small compared to that of the deflection due to moment (Gere & Timoshenko, 1991). However, both the deflection due to moment and shearing deflection must be considered if the span-to-depth ratio of the specimen is small (Nguyen et al., 2013). Case & Chilver (1971) stated that shearing deflection is important only for deep beams and that the influence of shear to the total deflection is equal to approximately $(h/L_{span})^2$ where h is the depth of the beam and L_{span} is the span length. According to Elsaigh (2007), shear stresses would contribute significantly to the total deflection of the beam with a span-to-depth ratio in a range of 3 to 4. The total deflection (δ) of a beam is estimated as the sum of the deflection due to moment and the deflection due to shear forces. The unit-load method was used by Elsaigh (2007) to obtain the total deflection by integrating curvature ($\varphi = M/EI$) and shear strain ($\gamma = V.f_{sh}/GA$) along the beam (see **Equation 2-5**).

$$\delta = \delta_M + \delta_V = \int_0^L \frac{M_u\, M_L .\, dx}{EI} + \int_0^L \frac{V_u\, V_L .\, dx}{GA/f_{sh}} \qquad \textbf{Equation 2-5}$$

where M_u is the moment due to a unit load and M_L is the moment due to actual load, EI is the flexural rigidity, V_u is the shear force due to unit load, V_L is the shear force due to actual load, GA/f_{sh} is the shearing rigidity of the beam and f_{sh} is the factor for shear. For a rectangular section, f_{sh} is equal to $6/5$ (Gere & Timoshenko, 1991). The deflection due to moment (δ_M) is calculated from the distribution of the curvature due to moment (φ) along the beam where φ replaces M_u/EI in **Equation 2-5**. The deflection due to shear force (δ_V) is calculated from the distribution of the shear strain (γ) along the beam (Elsaigh, 2007). The relationship between moment and curvature and shear force and shear strain is illustrated in **Figure 2-25**. The relationship between moment and curvature (**Figure 2-25 (a)**) is linear elastic up until the first crack formation (OA). Then, from the first crack to the post crack, hardening behaviour is observed (AB) and softening behaviour after the post crack (BC). Shear behaviour is always expressed as a linear relationship when the specimen experiences an applied load up until failure (Nguyen et al., 2013). Shear strains on the shear force-shear strain diagram (**Figure 2-25 (b)**) can be calculated using the measured load-displacement response by dividing the shear force by the shearing rigidity (GA/f_{sh}) (Elsaigh, 2007). The diagram for curvature and shear strain along a beam was set out by Nguyen et al. (2013) as shown in **Figure 2-26**.

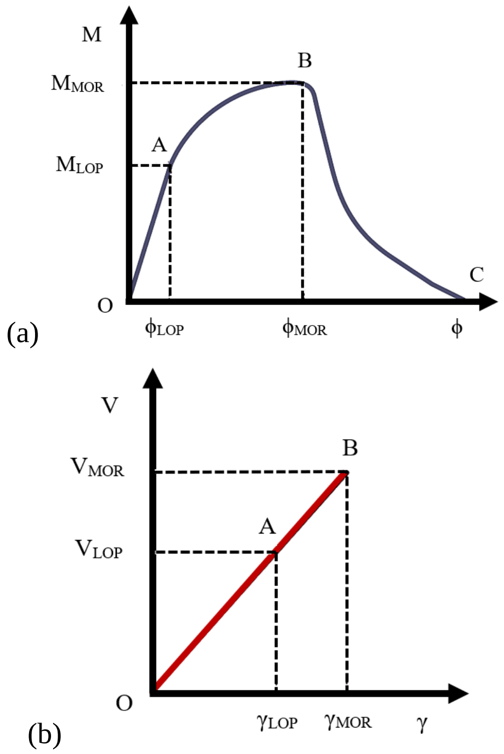

Figure 2-25: (a) Moment-curvature relationship and (b) shear force-shear strain relationship (adapted from Elsaigh, 2007)

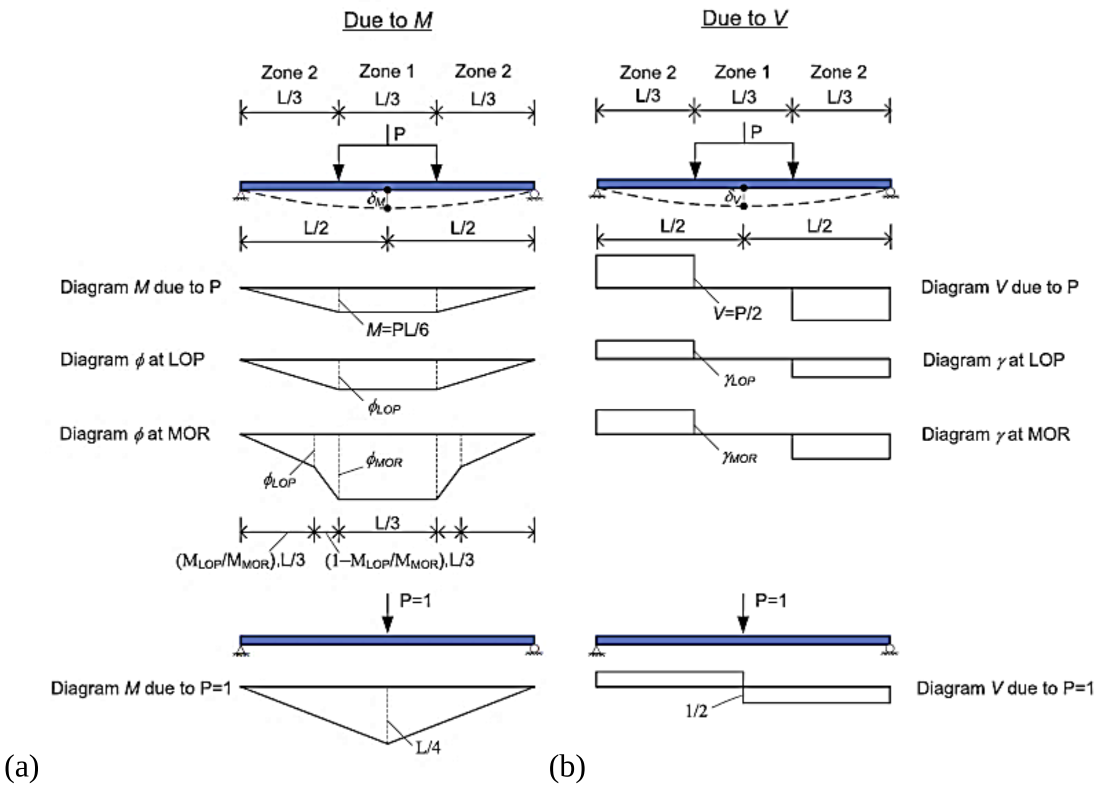

Figure 2-26: Distribution along the beam of (a) moment-curvature and (b) shear force-shear strain for an applied load P (Nguyen et al., 2013)

2.8.5.1 Effect of steel fibres

According to various authors, fibres significantly influence the flexural properties of UHPC (Kang et al., 2010; Kazemi & Lubell, 2012; Abbas et al., 2015). Kang et al. (2010) stated that the flexural tensile strength of UHPC increased linearly with increased fibre dosage (See **Table 2-6** and **Figure 2-27**). Yoo & Yoon (2016) reported that much higher post-cracking stiffness and ultimate load carrying capacity was obtained with UHPFRC beams (2 % by volume of steel fibres) compared to UHPC beams without fibres. Fibres prevent the intergrowth of micro-cracks by absorbing tensile stresses and, in effect, macro-cracks are prevented (Orgass & Klug, 2004). Kazemi & Lubell (2012) reported that UHPFRC beam specimens showed multiple cracks and experienced a steadier drop in load carrying capacity after the formation of the first crack. A single macro-crack with multiple micro-cracks characterised the failure of the UHPFRC beam specimen. Poon et al. (2004) reported that the addition of steel fibres increased the toughness of unheated concrete by approximately two times.

Table 2-6: Effect of steel fibre dosage on the flexural tensile strength of UHPC

References	Fibre (L/D)	Specimen size (mm)	Fibre content (%)	Flexural strength (MPa)
Orgass & Klug (2004)	13/0.16	100 x 100 x 500	0.0	9.8
			1.0	11.2
			2.0	14.7
Kazemi & Lubell (2012)	13/0.2	100 x 100 x 300	0.0	15.0
			2.0	23.1
			4.0	38.4
Shu-hua et al. (2012)	18/0.2	100 x 100 x 400	0.0	17.7
			1.0	18.9
			2.0	20.0
Abbas et al. (2015)	12/0.2	100 x 100 x 400	0.0	20.45
			1.0	29.87
			3.0	49.12

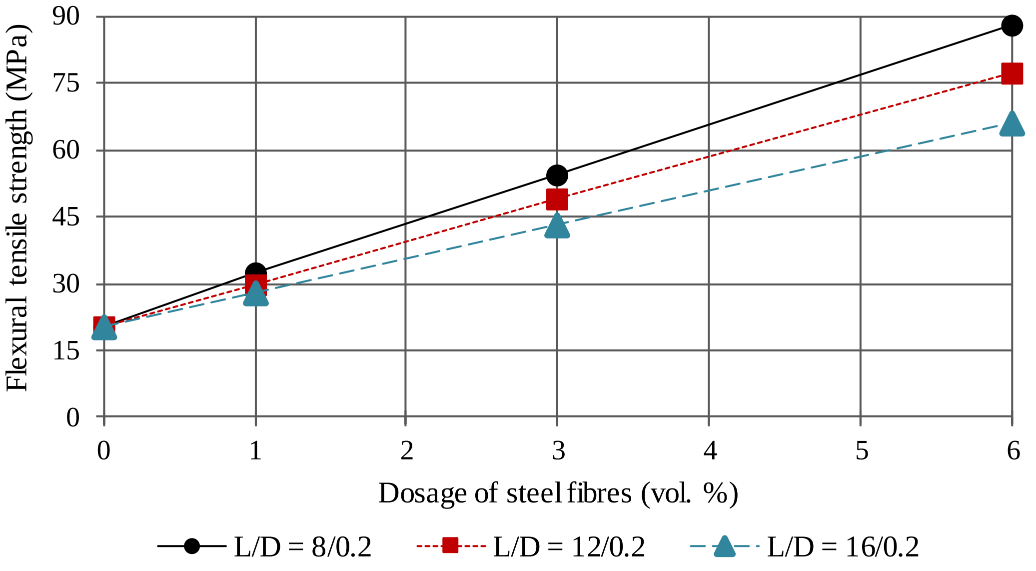

Figure 2-27: Effect of steel fibre dosage and length on the flexural tensile strength of UHPC (adapted from Abbas et al., 2015)

Furthermore, Yu et al. (2012) observed that the aspect ratio of the steel fibres play a role in the flexural capacity of UHPC (see **Figure 2-27**). Mixtures incorporating fibres with a higher aspect ratio have increased number of fibres per unit volume of concrete, which leads to more fibres bridging cracks and, in effect, an increased flexural capacity. This is however contradicting to the results obtained from Abbas et al. (2015), who illustrated that UHPFRC mixtures incorporating short steel fibres (8 mm), and thus lower aspect ratio, show higher flexural tensile strength compared to mixtures with similar dosages and diameter of longer steel fibres (12 mm and 16 mm) (see **Figure 2-27)**. This was attributed to short fibres better bridging the growth of micro-cracks which delayed the formation of macro-cracks and led to higher peak load carrying capacity. More short fibres are available for crack bridging at the same dosage compared to that of the longer fibres. The difference in flexural tensile strength due to fibre length is more prominent with higher fibre dosages. Abbas et al. (2015) observed a steadier drop in load carrying capacity after the peak load was reached for beams incorporating longer fibres compared to short fibres. This was attributed to the pull-out of short fibres after peak load was reached and the increase in energy required for pull-out of the longer fibres.

Wille et al. (2011a) reported flexural tensile strength of 30 MPa with 100 x 100 x 400 mm beams, with a span of 300 mm loaded at third points. The authors did however not state whether a linear-elastic stress state was assumed. Kahanji et al. (2017) observed that beams with a fibre content of 1 % and 2 % (by volume) showed no significant difference in deformation and flexural behaviour. However, beams with a fibre content of 4 % (by volume) showed significantly higher flexural capacity. Beams containing 1 % (by volume) fibres exhibited higher peak load toughness energy compared to beams containing 2 % and 4 % (by volume) fibres. The authors did not make any attempt to explain this trend. Yu et al. (2017) illustrated that the flexural strength of UHPFRC cast on one side of the mould (controlled) yielded higher flexural strength results compared to that of random casting (see **Figure 2-28**). This is attributed to the influence of fibre-orientation in UHPFRC. The figure also illustrates that flexural strength increases with the addition of fibres.

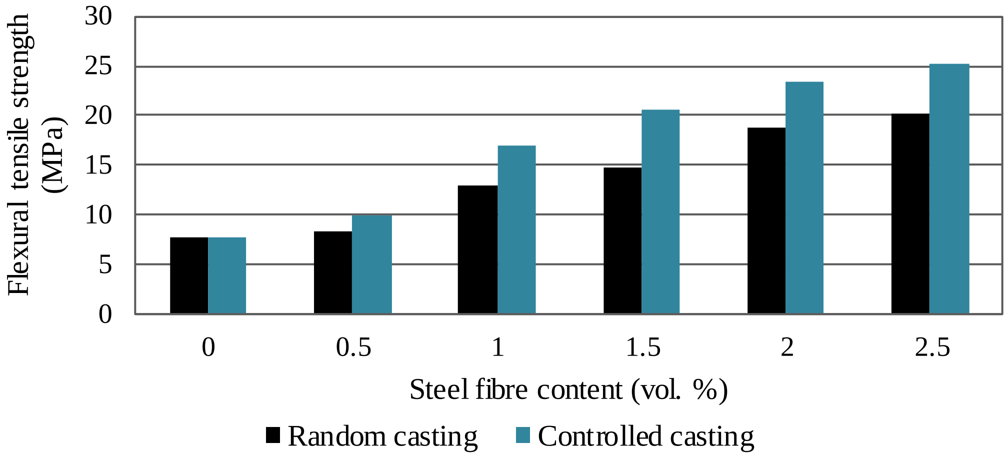

Figure 2-28: Comparison of the flexural strengths for UHPFRC with different fibre contents and different casting methods (adapted from Yu et al., 2017)

2.8.5.2 Effect of specimen size

Denneman (2011) stated that: "*high performance fibre reinforced concrete will exhibit a strong size effect due to its high post crack stress capacity. The size effect will limit the reliability of the MOR obtained for a specific specimen size and geometry, as a predictor of the peak load of elements of a different size and geometry*". The flexural tensile strength of UHPC specimens decreases as the specimen size increases (see **Table 2-7)** due to the higher wall effect of fibres in smaller specimens (Kazemi & Lubell, 2012). Although not indicated in the article, the assumption of linear-elastic stress state can wrongly portrait the size effect due to the wall effect. It was also observed by Orgass & Klug (2004) that the improved fibre orientation within smaller specimens led to higher ductility compared to that of larger specimens. Furthermore, Nguyen et al. (2013) reported that the number of cracks as well as the crack spacing decreased as the specimens size decreased (see **Figure 2-29**). This can be attributed to their increased flexural tensile strain capacity (Nguyen et al., 2013).

Table 2-7: Effect of beam size on the flexural tensile strength of UHPC

References	Fibre (L/D)	Fibre content (%)	Specimen size (mm)	Flexural strength (MPa)
Collepardi et al. (1997)	13/0.18	2.5	150 x 150 x 600	20.2
			40 x 40 x 160	48.3
Orgass & Klug (2004)	13/0.16	2.0	150 x 150 x 700	13.0
			100 x 100 x 500	14.7
			40 x 40 x 160	18.3
Kazemi & Lubell (2012)	13/0.2	2.0	100 x 100 x 300	23.1
			50 x 50 x 150	29.1

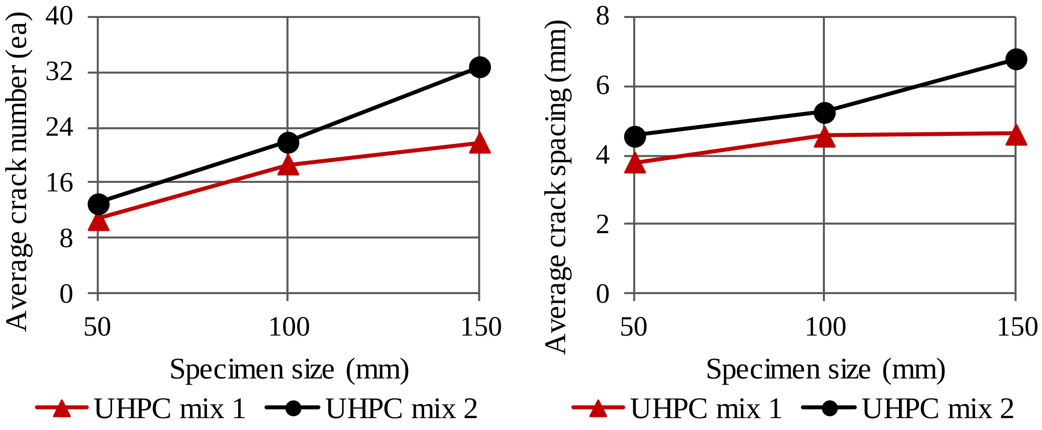

Figure 2-29: Size effect on cracking behaviour (adapted from Nguyen et al., 2013)

Researchers, such as Reagel & Willis (1931), have long established that flexural strength is not a true material property because its value changes with specimen size. Flexural strength also does not provide a sufficient indicator of the fracture toughness of the material, as it is an indicator of ultimate strength only (Denneman et al., 2010). The results obtained by Denneman (2011) are shown in **Table 2-8**. The results indicated that a span-to-depth ratio of 10 yielded the highest flexural strength results for both mixtures. Higher span-to-depth ratios were, however, not considered.

Table 2-8: The effect of span-to-depth ratio on flexural strength (Denneman, 2011)

Fibre content (kg/m^3)	Specimen size (mm)	Span-to-depth ratio	Flexural strength (MPa)
80.1	150 x 150 x 550	3.33	13.3
	150 x 125 x 550	4	13.5
	150 x 75 x 550	6.67	11.3
	150 x 50 x 550	10	13.9
119.5	150 x 125 x 550	4	13.9
	150 x 75 x 550	6.67	13.4
	150 x 50 x 550	10	14.7

2.8.5.3 Effect of pre-treatment

Poon et al. (2004) stated that UHPFRC exhibited higher toughness values after the exposure to high temperatures. Kahanji et al. (2017) reported that UHPFRC beams (100 x 150 x 1300) cured at 90 °C had a slightly higher strength and stiffness compared to beams cured at 20 °C. Kahanji et al. (2017) observed no significant effect on the cracking pattern of the beams due to different curing regimes. **Figure 2-30** illustrates the effect of a curing regime on the flexural tensile strength of UHPC. Müller et al. (2008) showed that autoclaved specimens, for both mixture designs, obtained the highest strength and were more than double the strength of the 23 °C water bath cured specimens. However, the specimen exposed to 250 °C steam curing showed the lowest strength results, which contrasts other literature (Poon et al., 2004; Kahanji et al., 2017). Müller et al. (2008) stated that this could be attributed to micro cracks in the concrete due to induced stress during the cooling of the specimens. Yang et al. (2009), on the other hand, showed that specimens cured in 20 °C water had 10 % lower flexural strength and 15 % lower fracture energy compared to specimens cured in 90 °C.

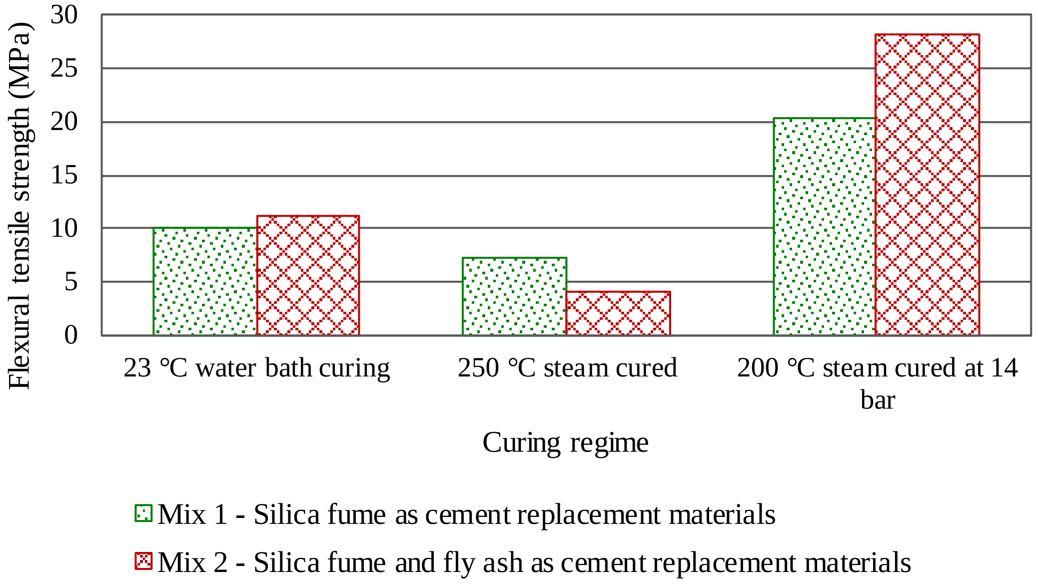

Figure 2-30: Flexural strength of UHPC exposed to different curing regime (adapted from Müller et al., 2008)

2.9 VOLUME CHANGE OF UHPC

According to Domone & Illston (2010), volume change of concrete is a result of both environmental effects (such as moisture gain, moisture loss and temperature) and from applied loads/stresses (short-term and long-term). Volume change due to environmental effects include plastic shrinkage, chemical/autogenous shrinkage, drying shrinkage, thermal deformation and carbonation shrinkage. Deformation due to applied load consists of elastic strain and creep. Plastic, drying and autogenous shrinkage are linked to moisture effects, while thermal deformation is related to temperature effects. Carbonation shrinkage is related to chemical effects (Smit, 2015).

2.9.1 Early age shrinkage

The shrinkage of concrete is influenced by the environmental conditions surrounding the concrete member and is independent of the external load on the concrete member. As soon as the concrete mixing takes place, shrinkage starts as a result of the absorption of the water by the cement and the aggregate. Over time, water evaporates from the surface of the mixture. The hydration process, which continues for several months, not only causes chemical shrinkage but also causes heat generation, resulting in further shrinkage due to thermal contraction. Thermal shrinkage can be controlled by regulating the temperature during the drying time of the concrete. Shrinkage of concrete varies with time. A comprehensive definition for autogenous shrinkage was proposed by the Japanese Concrete Institute which states that: "*Autogenous* *shrinkage is the macroscopic volume reduction of cementitious materials when cement hydrates after initial setting. Autogenous shrinkage does not include volume change due to loss or ingress of substance, temperature variation, application of an external force and restraint.*”

Self-desiccation forms part of autogenous shrinkage. The paste is subject to self-desiccation when there is insufficient moisture movement to or from the cement paste, which leads to removal of water from the capillary pores (Domone & Illston, 2010). Autogenous shrinkage has become of great interest to researchers since the growing use of low w/b ratios in concrete. According to Smit (2015), the magnitude of autogenous shrinkage in cement paste is a function of the w/c ratio. Autogenous shrinkage of the cement paste is more than that of the concrete. This is attributed to the rigid skeleton of the aggregate particles and the hardened cement paste that restrains contraction of the paste body. Most of autogenous shrinkage occurs in the first few days after casting.

Yoo et al. (2018) observed that heat cured UHPC specimens experience accelerated shrinkage development compared to ambient cured specimens. This is illustrated in **Figure 2-31**. There is no significant difference between autogenous shrinkage and total shrinkage, regardless of the curing regime. Thus, total shrinkage of UHPFRC is mainly influenced by autogenous shrinkage instead of drying shrinkage. This is due to the dense microstructure of UHPC and smaller pore sizes (Yoo et al., 2018). There is no significant difference in the long-term shrinkage between ambient cured specimens and thermal cured specimens. In the first twenty-four-hours after casting precast specimens, the cement paste may experience contraction of the paste body and a decrease in the paste volume. However, the cement paste is not restrained and free to experience contraction in the mould. Only after twenty-four-hours would the precast elements be demoulded and, after the concrete has gained enough strength, would they be installed in a structure on site. No stresses induced by autogenous shrinkage are thus transferred to the structure after placement, since most of the autogenous shrinkage occurs in the first few days after casting. Therefore, even though high early age shrinkage forms a significant part of the total shrinkage in UHPC, early age volume change caused by self-desiccation and autogenous shrinkage was not part of the scope of this study.

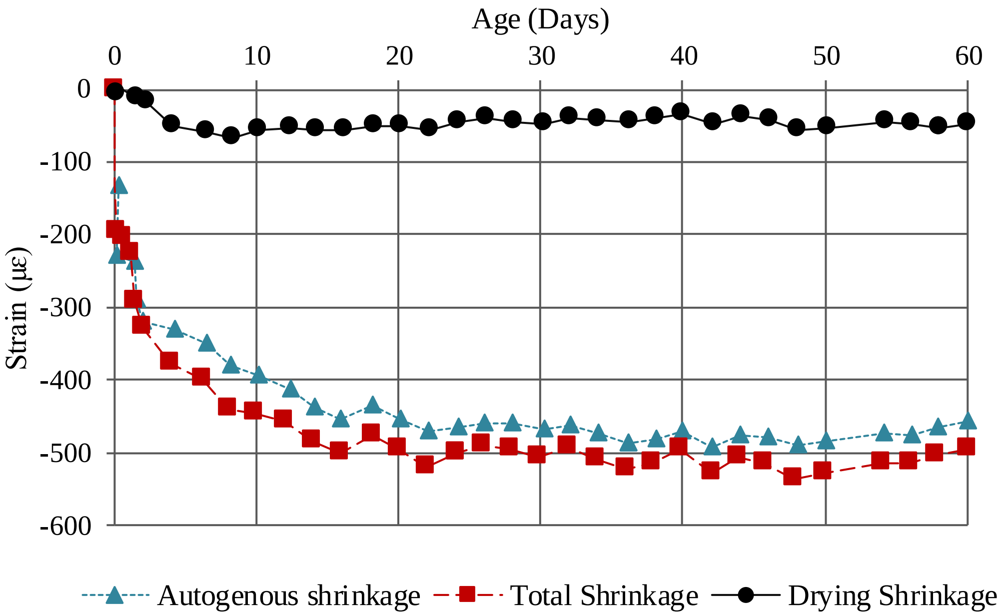

(a)

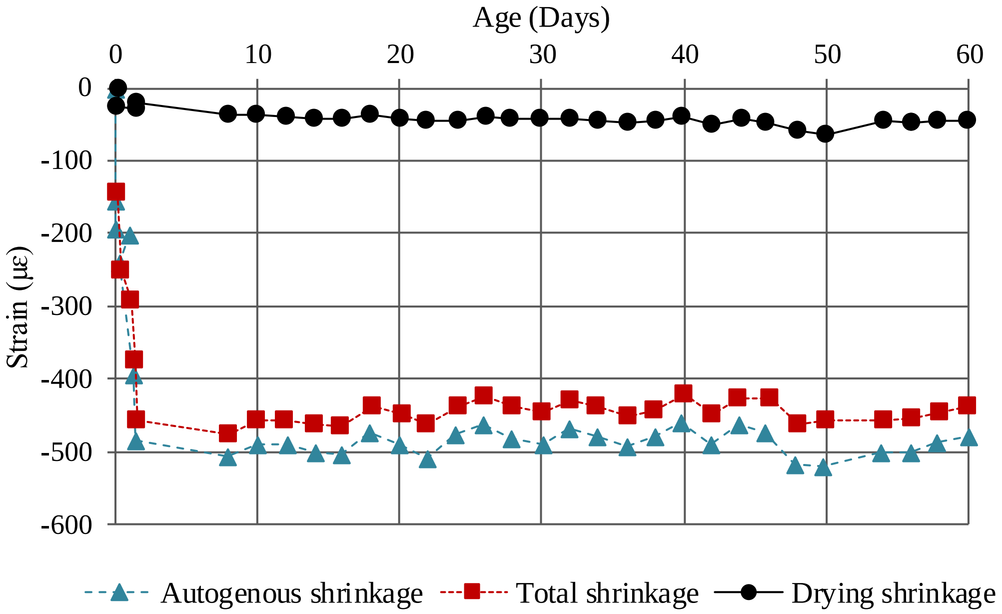

(b)

Figure 2-31: Free shrinkage behaviour of UHPFRC under a) ambient curing and b) heat curing (adapted from Yoo et al., 2018)

2.9.2 Drying shrinkage

Drying shrinkage is defined as the shrinkage of the unloaded concrete in drying conditions. It is caused by the withdrawal of moisture from the concrete. A typical stress versus time curve of drying shrinkage is illustrated in **Figure 2-32**.

The amount of creep and drying shrinkage of UHPC can be limited with a high particle packing density (Bache, 1981; Fennis & Walraven, 2012). A lower w/c ratio can further reduce drying shrinkage due to the reduced amount of evaporated water in the cement paste (Neville, 1995; Yoo et al., 2018). This makes UHPFRC a very suitable material for precast applications. Meng et al. (2017) reported a total drying shrinkage range of 56 μm/m to 500 μm/m, depending on the type of mixture constituents. Habel et al. (2008) measured drying shrinkage of 170 μm/m after fifty-days and stated that most of the drying shrinkage occurred during the first twenty-days after casting. Yoo et al. (2018) reported drying shrinkage of 45 μm/m. UHPC generally experiences lower drying shrinkage compared to that of conventional concrete due to the lower permeability of the matrix (Habel et al., 2008) and denser microstructure (Bache, 1981). This is also confirmed by Vicenzino et al. (2005), who reported that the drying shrinkage of UHPFRC is twice that of conventional concrete, due to the elimination of coarse aggregates in the UHPFRC matrix. Coarse aggregates help to restrain shrinkage in conventional concrete (Vicenzino et al., 2005). Yoo et al. (2018) state that the shrinkage behaviour of UHPC needs further investigation. The drying shrinkage of UHPC could probably be limited by minimising the cement content and replacing some of the binder with inert material (such as aggregate).

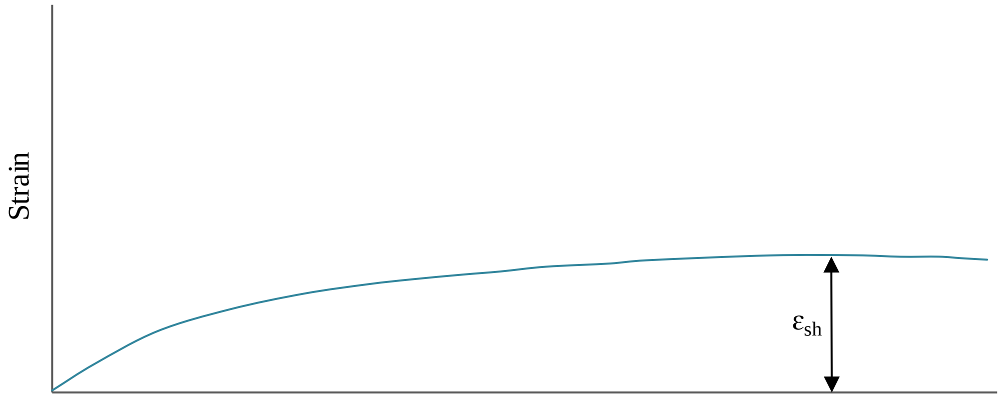

Figure 2-32: Free shrinkage/drying shrinkage (no stress) (adapted from Domone & Illston, 2010)

2.9.3 Creep

Creep affects most materials to some extent and, according to Hurst (2003), the basic mechanism of creep in concrete is that of gradual loss of moisture which causes contraction in the concrete. Creep behaviour due to a constantly applied load is illustrated in **Figure 2-33**, as shown in Domone & Illston (2010). Most of the creep develops within a fairly short time after the application of the load. The creep is substantially increased when the concrete is drying simultaneously, in other words, creep and drying shrinkage are interdependent. After the load is removed from the concrete element, it would experience an immediate reduction in strain, followed by a more gradual reduction referred to as creep recovery. The effect of creep is, however, not completely recoverable and some deformation of the concrete remains (Smit, 2015). Basic creep is defined as creep of a specimen under load but not drying. A typical stress versus time curve of basic creep is illustrated in **Figure 2-34**. The addition of steel fibres in UHPC results in reductions of drying shrinkage and creep deformation of concrete (Afroughsabet et al., 2016). According to Collepardi et al. (1997), drying shrinkage and creep strain is lower in steam cured specimens compared to specimens cured at room temperature. Binard (2017) states that, after heat curing, creep can be regarded as constant and drying shrinkage is essentially non-existent.

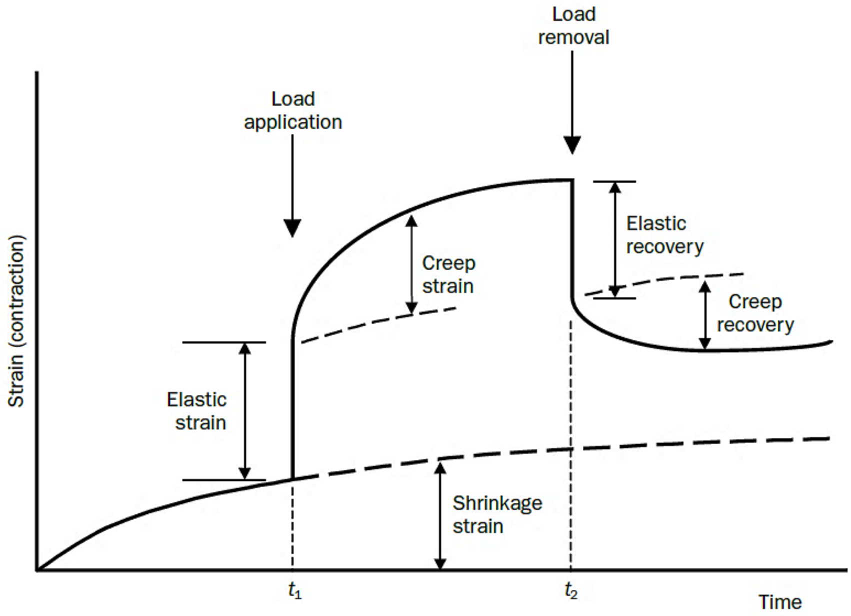

Figure 2-33: The response of concrete to a compressive stress applied in a drying environment (Domone & Illston, 2010)

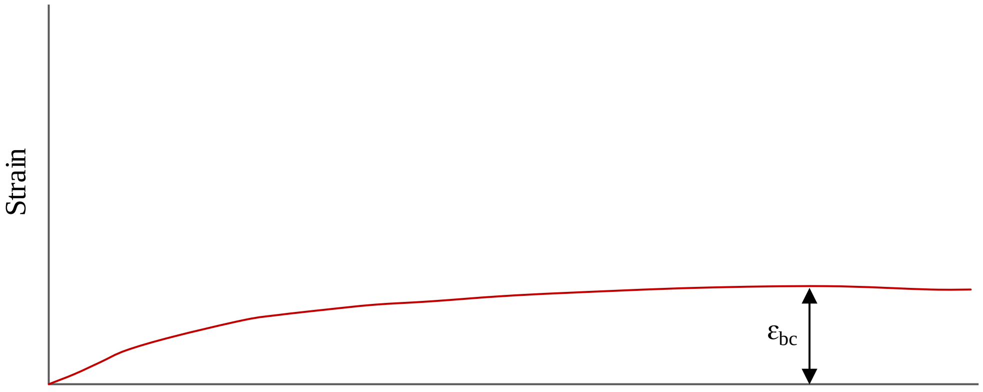

Figure 2-34: Basic creep (stress, no loss of moisture) (adapted from Domone & Illston, 2010)

2.10 CRACKING MODELS FOR CONCRETE

The numerical modelling of cracking of concrete is generally categorised into discrete and smeared approaches (Elsaigh et al., 2007). According to Ngo & Scordelis (1967), a crack is modelled as a geometrical discontinuity, when using the discrete crack approach. Several developments of discrete crack models exist. Elsaigh (2007) reported that simple discrete crack models use special interface elements. These interface elements must either be placed initially in predefined planes or a re-meshing approach is required for the elements in the area of the crack.

In the smeared crack approach, introduced by Rashid (1968), a cracked solid is represented to be a continuum. Micro-cracks are smeared over a crack bandwidth (beyond the cracking point) and materials within this bandwidth is subject to the assumed tension softening stress-strain relation (Elsaigh, 2007). Under increased loading the growth of this band is modelled by reducing the stiffness of the element. In this method the elastic section properties are retained beyond cracking while the material stiffness and strength is reduced to match the actual behaviour of concrete.

Elsaigh (2007) concluded the following: *"the discrete crack approach is deemed to best fit the natural conception of fracture since it generally identifies fracture as a true geometrical discontinuity, whereas a smeared representation is deemed to be more realistic considering the "band of micro-cracks" that form the blunt fracture in matrix-aggregate composites like concrete."* If only the overall load-displacement behaviour is required, the smeared crack approach is the best choice (Elsaigh, 2007).

2.11 SUMMARY

The aim of this chapter was to provide an overview on the material characteristics of UHPC. The chapter served as a guideline defining the course of this study.

The materials used in UHPC and their behaviour were investigated. It was found that UHPC involves more unknowns, variables and dimensions than ever before. However, there are numerous methods to design UHPC mixtures. Extensive studies have revealed that the improvement of the micro and macro properties of the mixture is a key factor in the production of UHPC. Based on the literature review, there is a need to determine an optimised mixture design for UHPC by using available South African materials. Local streams of by-products, such as fly ash and silica fume, were chosen as cement extenders, not only for economic benefits, but also to increase the workability and efficiency of the mixture as well as the flexural and compressive strength. It was decided to use the modified Andreasen and Andersen particle packing model to optimise the UHPC matrix. This method incorporates minimum particle size and the range of fine particles is better presented. Three types of aggregate with different grain sizes were chosen to enhance packing density, namely, silica sand, dolomite sand and dolomite stone. When a particle packing model, industrial by-products and controlled casting methods are well employed, an optimised UHPC can be produced, which should yield a lower environmental impact and should further the development and usage of UHPC and provide additional ideas for a cleaner production of cement-based materials. It was found that a practical method to efficiently utilise steel fibres is of great importance and needs further investigation. RSM was chosen to optimise the combined fibre and superplasticiser content. RSM is an efficient and effective method in predicting the performance and optimising the mixture ingredients of concrete. A superplasticiser as a high range water reducer was chosen to enhance workability and improve flow characteristics. Based on literature, it was decided to use micro steel fibres (13 mm long and 0.2 mm diameter) to enhance the mechanical properties of the concrete. Pre-treatment and curing procedures have received much attention by various researchers due to the significant effect of a curing regime on the mechanical properties of UHPC. Contradicting literature made it difficult to compare different curing regimes and their influence on mechanical properties. Therefore, the difference between conventional water bath curing (25 °C) and hot water bath curing (80 °C) on the mechanical properties and microstructure of UHPFRC was investigated in this study.

3 MIXTURE DESIGN

3.1 INTRODUCTION

In this study, the modified Andreasen and Andersen optimum particle packing model was utilised to develop an optimised UHPC matrix while using available South African materials. The optimum combined superplasticiser and fibre content for the UHPC were determined by taking material cost into account and using a response surface design. Various tests were performed to determine the fresh and mechanical properties of the UHPC mixture. Flowability, air content and densities were considered. The mechanical properties include compressive strength, modulus of elasticity and splitting tensile strength. The experiments were carried out in the Civil Engineering laboratory of the University of Pretoria.

3.2 MATERIALS

Class I 52.5R Portland cement was used with Undensified Silica Fume (USF) and Unclassified Fly Ash (FA) as cementitious materials. The chemical composition of these materials (based on X-Ray Fluorescence (XRF) results) can be seen in **Table 3-1**.

Table 3-1: Chemical composition (%)

	SiO_2	MgO	Al_2O_3	SO_3	K_2O	CaO	Fe_2O_3	TiO_2	Na_2O	LOI
C	20.74	2.31	4.98	1.76	0.13	62.53	2.52	0.34	0.11	3.60
USF	95.00	0.25	<0.10	0.30	0.63	0.70	<0.10	---	0.18	2.00
FA	54.45	1.20	31.88	<0.01	0.73	4.19	3.27	1.48	0.20	0.93

C: Class I 52.5R Portland Cement, USF: Undensified Silica Fume, FA: Unclassified Fly Ash.

Silica sand with a maximum size of 1.50 mm together with dolomite sand with a maximum size of 4.75 mm were chosen as the fine aggregate and dolomite stone with a maximum size of 6.70 mm was chosen as the coarse aggregate. Aggregates were mainly chosen based on locality, type and cost. Straight steel fibres with a length of 13.0 mm and a diameter of 0.2 mm were used in all mix designs. The tensile strength of these fibres is 2500 MPa. A commercially available polycarboxylate ether-based superplasticiser was added to improve the workability of the mixes. The superplasticiser contains no additional defoaming agents. The relative densities obtained for the various materials are tabulated in **Table 3-2**.

Table 3-2: Relative Densities

	C	USF	FA	W	D-A	D-S	S-S	SP	SSF
RD	3.14	2.45	2.22	1.00	2.85	2.91	2.67	1.06	7.85

C: Class I 52.5R Portland Cement, USF: Undensified Silica Fume, FA: Unclassified Fly Ash, W: Water, D-A: Dolomite Stone, D-S: Dolomite Sand, S-S: Silica Sand, SP: Superplasticiser, SSF: Short Straight Fibre, RD: Relative Density.

3.2.1.1 Particle Size Distribution

The PSD was determined for all dry materials using a Malvern Instruments Mastersizer 2000 (Hydro 2000MU) apparatus. The system, driven by Standard Operating Procedures (SOPs), has set exact standards in laser diffraction particle sizing. A Laser and Ultrasound test was conducted on two samples from each material and the average of the results was calculated and plotted. Ultrasound was used in order to disperse the particles. The PSD of all the dry materials can be seen in **Figure 3-1**. It can be noted that the PSD of the FA and USF is comparable to that of cement. As mentioned in literature, USF is prone to agglomeration.

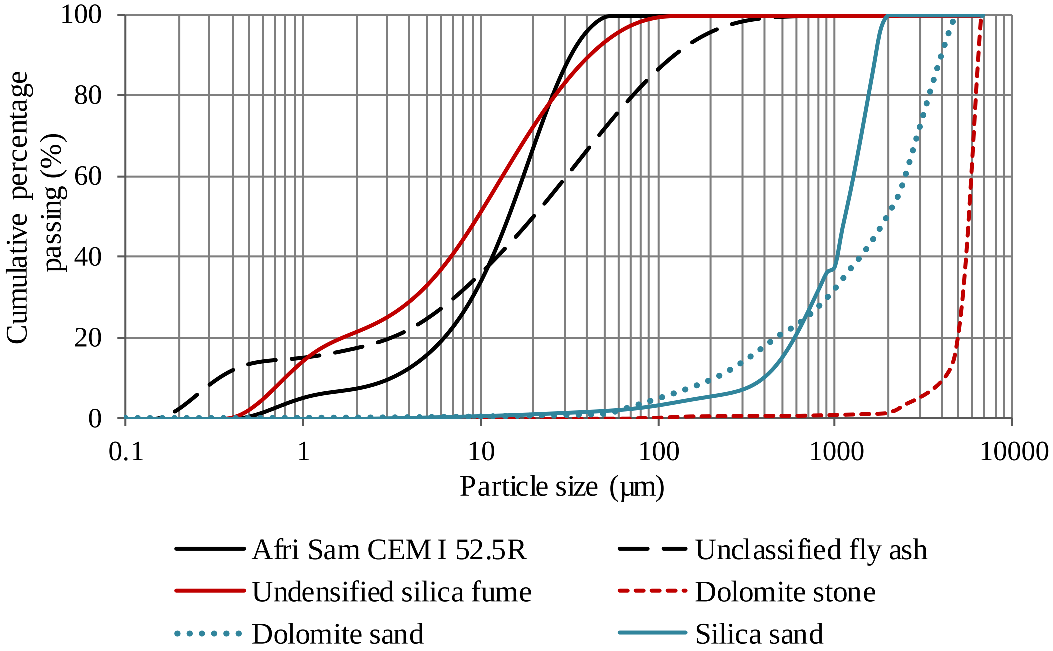

Figure 3-1: Particle Size Distribution

The silica fume was mixed with superplasticiser whereafter a PSD was done on the mixed sample (see **Figure 3-2**) to establish whether the superplasticiser can break up the silica fume agglomerates. As can be seen, the PSD for the mixed sample yields a PSD indicating larger particles compared to the USF samples and, thus, superplasticiser did not break up the agglomerates. The fact that neither ultrasound nor superplasticiser could break up the agglomerates indicates that the silica fume would remain in an agglomerated state in the concrete mixture.

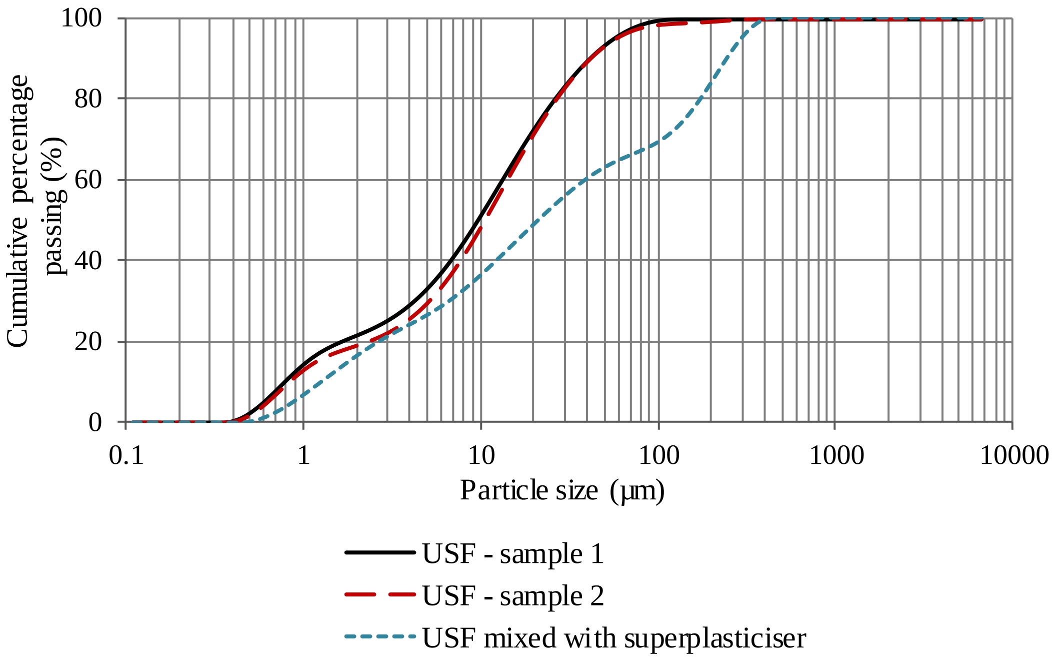

Figure 3-2: Particle Size Distribution for Undensified Silica Fume

3.2.1.2 Scanning Electron Microscope (SEM)

Microstructure studies were conducted on various materials using a SEM. **Figure 3-3 (a)** illustrates a FA particle within the cement sample, while FA particles can be seen in **Figure 3-3 (b)**. This figure shows the characteristic spherical shape of FA particles. According to the PSD (see **Figure 3-1**), about 40 % of both the cement and FA particles passed through the 10 µm sieve. This corresponds to the SEM photos, where there are particles smaller and larger than the scale of 10 µm. **Figure 3-4** illustrates photos of cement particles, silica fume particles and FA particles. According to the PSD (see **Figure 3-1**), FA particles and USF particles should have the same percentage passing through the 1 µm sieve. This does not correspond to the SEM photos, where it can be seen that the USF particles are much smaller than the FA particles. However, when having a closer look at the USF particles (**Figure 3-4 (d) -** magnification = 100 000 and scale = 200 nm), it is clear that agglomeration of the USF particles was present. This confirms that the apparent PSD of silica fume, as indicated in **Figure 3-1**, should be used when optimising the packing density of the concrete mixture.

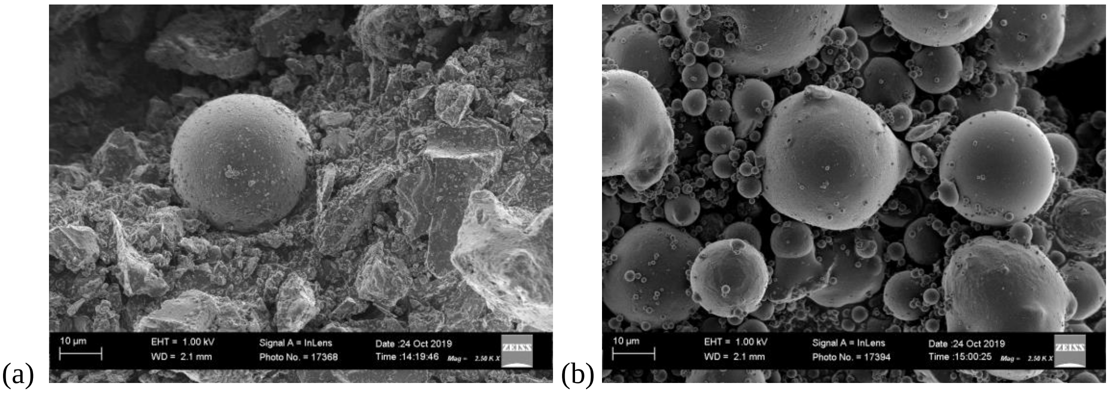

Figure 3-3: SEM photos for (a) cement illustrating FA particle, and (b) FA (magnification = 2 500 and scale = 10 µm)

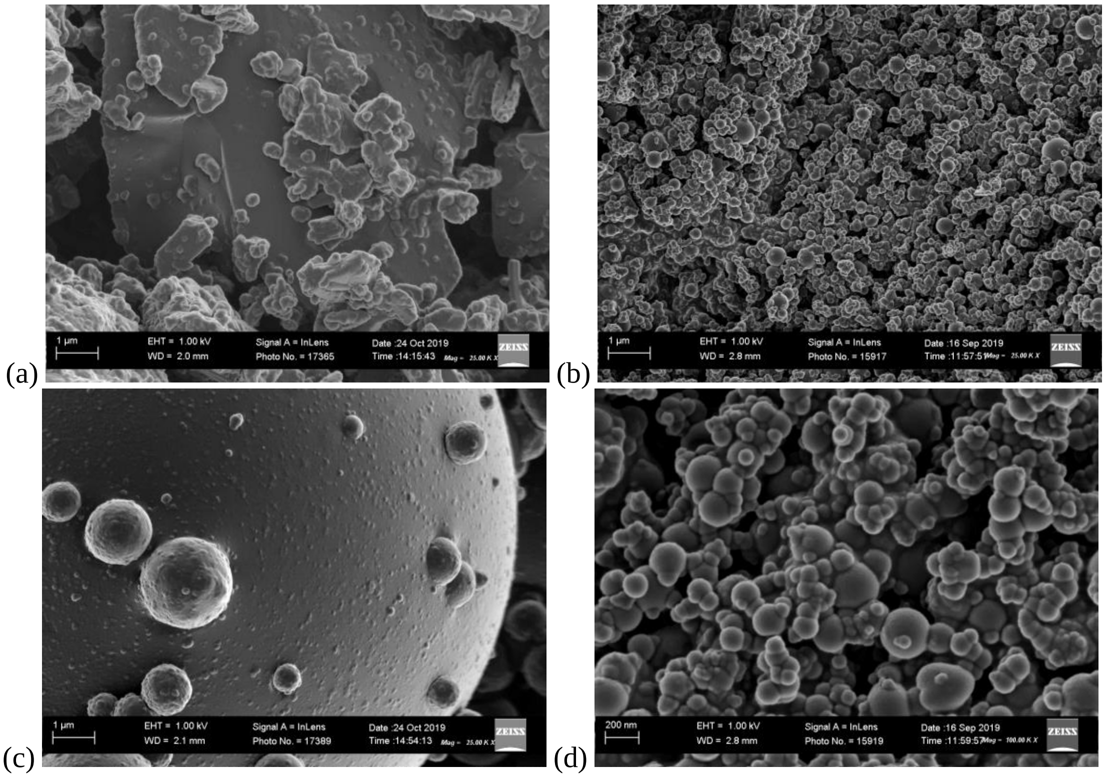

Figure 3-4: SEM photos for (a) Cement, (b) USF, (c) FA (magnification = 25 000 and scale = 1 µm) and (d) USF (magnification = 100 000 and scale = 200 nm)

3.3 MODIFIED ANDREASEN AND ANDERSEN PARTICLE PACKING MODEL

In this study, the modified Andreasen and Andersen particle packing model was used as a target function (**Equation 2-2**) to optimise the concrete mixture composition for all the granular materials. Based on the recommendation by Yu et al. (2014), the value of *q* was fixed at 0.23 in this study, since numerous fine particles are used to produce the UHPFRC matrix. The mass proportions (%) of each individual material in the concrete mix was adjusted (trial and error) until the deviation between the target curve and the composed mix, expressed as the RSS (**Equation 2-3**) at defined particle sizes, was minimised. The composition of the concrete was then considered optimal. In order to limit wastage and minimise cost, no processing took place (grinding or sieving to optimise PSD) and all materials were used as obtained from the suppliers. Based on the literature reviewed, it was decided to use a w/c ratio of 0.27 with the optimised mix composition as indicted in **Table 3-3**, with about 560 kg/m^3 of cement, extended with 17 % FA and 17 % USF. The grading curve for the composed mix is shown in **Figure 3-5** (RSS = 15.9; R^2 = 0.97) together with the target curve obtained from the modified Andreasen and Andersen particle packing model as well as the Fuller curve. The composed mix then serves as the optimised UHPC matrix which was used for the mix compositions throughout the study. Central Composite Design (CCD) was then used to optimise the combined fibre and superplasticiser content.

Table 3-3: Composed mix

Material	kg/m^3	Relative Density
Cement	566	3.14
Undensified Silica Fume	152	2.45
Unclassified Fly Ash	152	2.22
Water	152	1.00
Dolomite Stone	262	2.91
Dolomite Sand	1049	2.85
Silica Sand	226	2.67

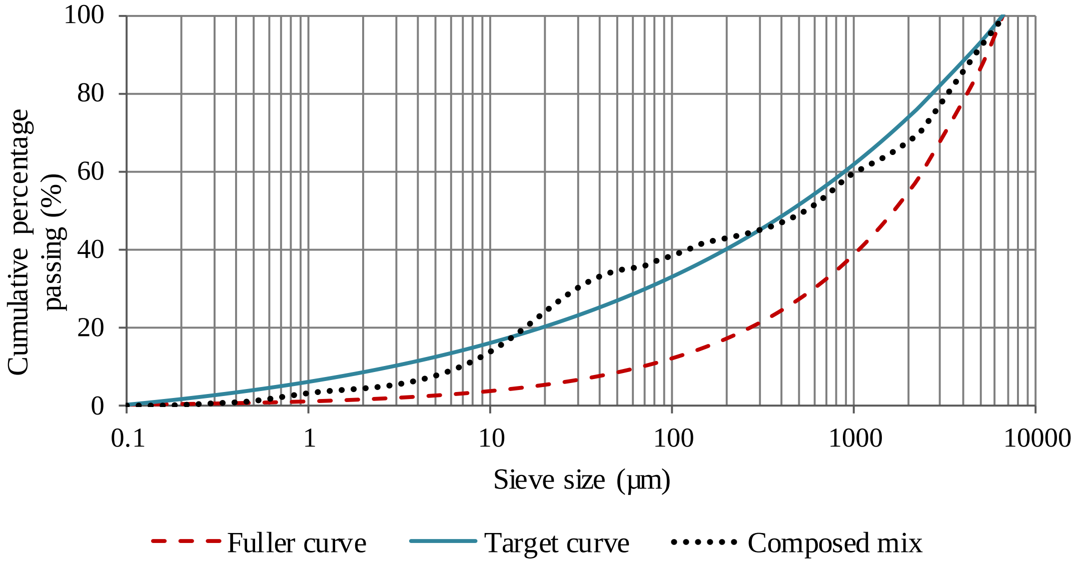

Figure 3-5: PSD of the Fuller curve, target curve and the resulting grading curve of the composed mix

3.4 RESPONSE SURFACE METHODOLOGY

In this study, the Design-Expert® software (Stat-Ease Inc., 2019., Minneapolis, USA) was used for the mixture design, statistical analysis, analysis of data and optimisation of the combined superplasticiser content and steel fibre amount. The procedure followed in Design-Expert® software to fit a mathematical model to the response data, is the inspection of the fit summary, model selection, analysis of variance (ANOVA) of the selected model, diagnostics of the residual plots and, if necessary, transformation of data (Stat-Ease Inc., 2019., Minneapolis, USA). ANOVA is a collection of statistical models that is used to identify significant differences between means.

The influence of parameters was investigated by using ANOVA and the quality of the model was determined by the coefficient of determination (R^2). The adjusted coefficient of determination (adjusted R^2) and the predicted coefficient of determination (predicted R^2) should both be maximised. The amount of variation that can be explained by the model is represented by the adjusted R^2 and the amount of variation of new data explained by the model represents the predicted R^2. A reasonable agreement must exist between the adjusted R^2 and the predicted R^2 (Stat-Ease Inc., 2019., Minneapolis, USA). From the fit summary, an informed decision can be made as to which degree model should be used.

In this study, the cost, flow, compressive strength, modulus of elasticity and splitting tensile strength denote the responses. Two parameters, namely superplasticiser content and steel fibre amount, were selected to describe this model. The ranges of the selected parameters were as follows: superplasticiser content range from 15.0 kg/m^3 to 30.0 kg/m^3 (approximately 2 % to 6 % of cement weight) and steel fibres range from 78.5 kg/m^3 to 236 kg/m^3 (approximately 1 % to 3 % by volume). The coded points as shown in **Figure 3-6**, together with their corresponding values is tabulated in **Table 3-4** (α = 1.41421 – rotatable, as recommended in literature). The various responses were investigated to determine the effectiveness of the superplasticiser content and fibre amount in improving the cost, flow and mechanical properties. A final optimised mixture was then determined from the results and conclusions obtained. The mechanical properties of the final optimised mixture were also investigated and compared to that of the predicted values as obtained from the CCD.

Table 3-4: Coded variables for CCD

Parameters	**Units**	**Coded variables**				
		- α	- 1	0	+ 1	+ α
Superplasticiser	kg/m^3	15.0	17.2	22.5	27.8	30.0
Straight Steel Fibre	kg/m^3	78.5	101.5	157	212.5	235.5

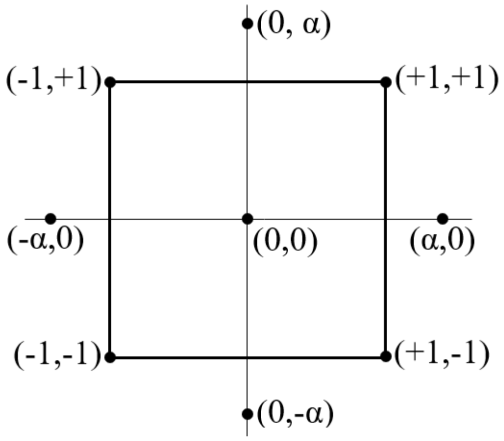

Figure 3-6: Coded points for CCD

3.4.1 Mix compositions obtained from CCD

The mix designs obtained from the CCD are tabulated in **Table 3-5**. A water-cement ratio of 0.27 was kept constant throughout all the mixes. The central mix was cast three times to test the repeatability of the experiment. The mixes were cast in a random order and in the manner as specified in **Chapter 3.3**.

Table 3-5: Mix compositions from the CCD (kg/m^3)

No.	C	USF	FA	W	D-A	D-S	S-S	SP	SSF
1	547	147	147	147	253	1014	218	15.0	157
2	542	146	146	146	251	1005	216	17.2	213
3	543	146	146	146	252	1007	217	22.5	157
4	538	145	145	145	249	997	214	22.5	236
5	543	146	146	146	252	1007	217	22.5	157
6	543	146	146	146	252	1007	217	22.5	157
7	540	145	145	145	250	1000	215	30.0	157
8	550	148	148	148	255	1019	219	17.2	102
9	549	148	148	147	254	1017	219	22.5	78.5
10	537	145	145	144	249	995	214	27.8	213
11	544	147	147	146	252	1009	217	27.8	102

C: Class I 52.5R Portland Cement, USF: Undensified Silica Fume, FA: Unclassified Fly Ash, W: Water, D-A: Dolomite Stone, D-S: Dolomite Sand, S-S: Silica Sand, SP: Superplasticiser, SSF: Short Straight Fibre.

The cost for each material is tabulated in **Table 3-6** and the surface plot obtained from the CCD for material cost in Rand/m^3 is illustrated in **Figure 3-7**. The Rand/m^3 varied between R5 535.00 per m^3 and R11 895.00 per m^3. A linear model was used and the R^2-value for the surface plot was 1.00. As expected, only the fibre content plays a significant role in the cost per m^3.

Table 3-6: Material cost

Material	Rand/kg
Portland Cement	1.92
Undensified Silica Fume	2.50
Unclassified Fly Ash	1.42
Water	0.02
Dolomite Sand	0.14
Dolomite Stone	0.13
Silica Sand	2.17
Superplasticiser	1.66
Short Straight Fibres	40.50

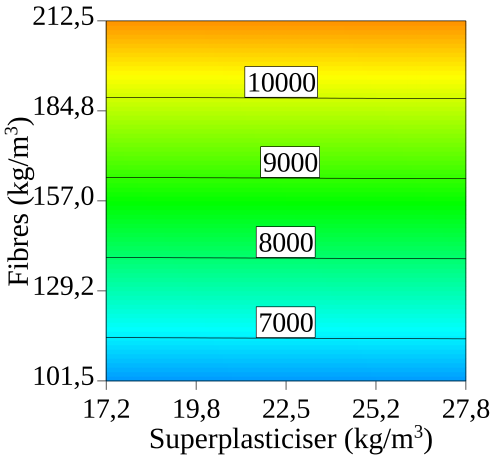

Figure 3-7: Surface plot for material cost in Rand/m^3

3.5 MIXING AND CASTING PROCEDURES

All the dry materials, except for USF, were mixed for approximately one minute. The USF was excluded from the dry mixing since it was undensified and would not mix with the other materials, but instead becomes airborne. Thereafter, the water and admixture were added to the mix, after which the USF was added. After approximately five minutes, the fibres were evenly distributed by hand. After the fibres were added, the concrete was mixed for another four minutes. All casting was done in steel moulds that were sufficiently lubricated. To ensure proper compaction, all the casting was done on a vibrating table and the specimens were vibrated for approximately one minute. The specimens cast for each mix composition, number of specimens cast and the day of testing are tabulated **Table 3-7** . After mixing, a flow table test was performed on all the fresh UHPFRC mixes (see **Figure 3-8**).

Table 3-7: Specimens cast for each mix composition

Parameter	Specimens cast	Amount	Testing days
Compressive strength	100 mm cubes	6	7, 28
E-value	Cylinders	3	28
Splitting tensile strength	-	-	28

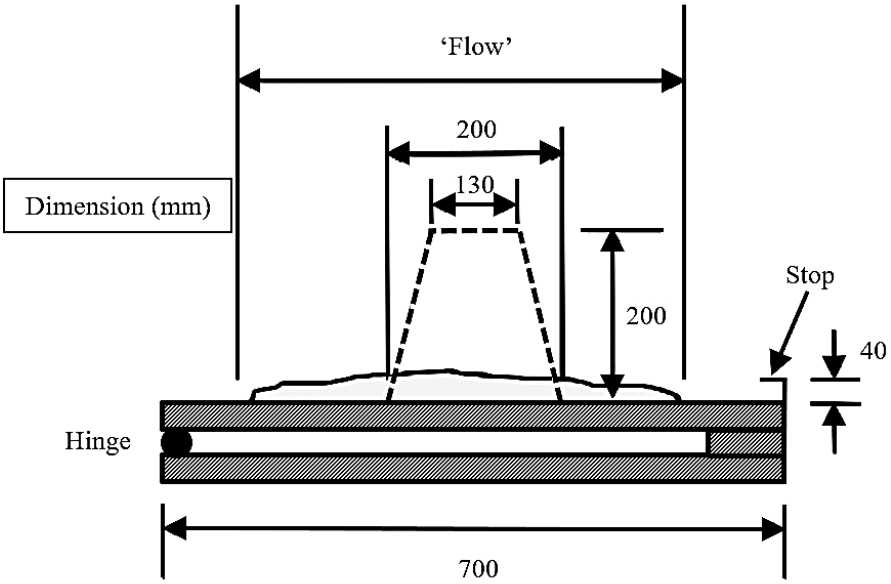

Figure 3-8: Flow table test (Domone & Illston, 2010)

The fresh concrete was used to fill a conical mould in the form of a frustum, as described in SANS 5862-2:2006. The mould was then carefully lifted straight upwards over a period of 5 seconds. The table top was raised slowly until it reached the upper stop and then allowed to drop freely to the lower stop. This cycle was repeated for a total of 15 drops. The total diameter of the concrete, spread in two directions (parallel to the edges of the table top), was measured and the mean value of both diameters was calculated in millimetres as the flow value (see **Equation 3-1**).

$$f = \frac{d_1 + d_2}{2}$$ **Equation 3-1**

where f is the flow value, d_1 is the maximum dimension of the concrete spread, parallel to one edge of the table, and d_2 is the maximum dimension of the concrete spread, parallel to the other edge of the table. Another method to evaluate the workability of UHPFRC is stipulated in BS EN 1015-3 and shown in **Equation 3-2**.

$$\xi_p = (\frac{d_1 + d_2}{2d_0})^2 - 1$$ **Equation 3-2**

where ξ_p is the relative slump, originally introduced by Okamura & Ozawa (1995) as the relative flow area (R), and d_0 is the base diameter of the cone used (200 mm).

All the specimens were left to cure under a curing blanket in a temperature-controlled room (25 °C). The specimens were demoulded approximately twenty-four hours after casting and subsequently cured in water (25 °C) until the day of testing.

3.6 MECHANICAL PROPERTIES

3.6.1 Compressive strength

The compression test specimens consisted of 100 × 100 × 100 mm cubes. The cube compressive strength was determined according to SANS 5863:2006. The specimens were weighed in and out of water to obtain the densities and air content before the test was performed. The test was performed by using a cube-crushing machine. The specimens were tested at a loading rate of 0.333 MPa per second. The standard compression test provides only a single value for the compressive strength of the concrete.

3.6.2 Modulus of elasticity

The E-value test specimens consisted of 100 × 200 mm cylinders. The modulus of elasticity was determined as discussed in BS EN 1239-13:2013. The test was performed by using a compression machine with a maximum capacity of 5000 kN. All the specimens were capped (by surface grinding) before the test was performed. The specimens were loaded at a loading rate of 2620 N per second and to only 40 % of the ultimate cylinder compressive strength. Each specimen was subjected to three loading cycles to minimise the hysteresis effects.

3.6.3 Splitting tensile strength

The splitting tensile test specimens consisted of the top and bottom halves of the cylinders used in the E-value test. The adjusted splitting tensile test procedure was used in accordance with the recommendations by Denneman (2011). The limit between the linear elastic (pre-crack) behaviour and the ductile (post-crack) behaviour of the UHPC was determined by monitoring the transversal deformation perpendicular to the load direction during testing. Two separate peak load conditions, namely the principal crack formation and the secondary crack formation, were thus determined during the test. The transversal deformation was measured with spring loaded Linear Variable Differential Transducers (LVDTs) (see **Figure 3-9**). Measurements were taken on both sides of the cylinder. The test was performed by using a compression machine with a maximum capacity of 5000 kN. The loading rate was kept constant at 1 MPa per minute. Splitting tensile strengths were calculated from the equation as discussed in SANS 6253:2006.

$$f_s = \frac{2P}{\pi L d}$$ **Equation 3-3**

where P is the failure load, L is the sample length, and d is the sample diameter.

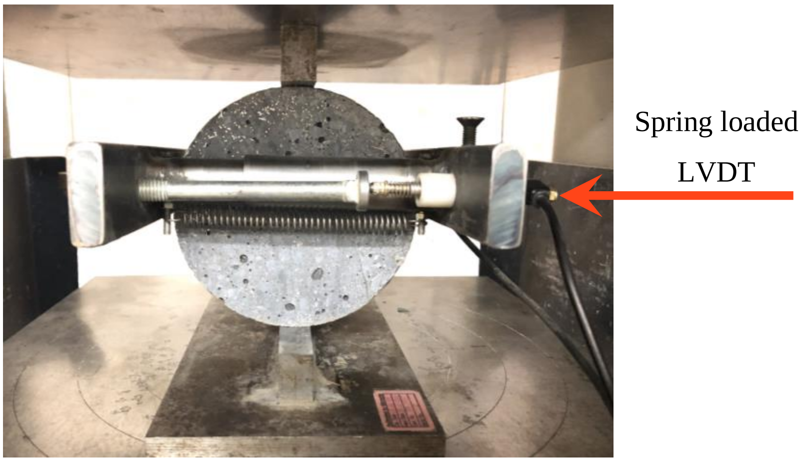

Figure 3-9: Splitting tensile strength specimen test set-up

3.7 EXPERIMENTAL RESULTS FROM CENTRAL COMPOSITE DESIGN

3.7.1 Statistical analysis

The model validation for various responses is tabulated in **Table 3-8**. The predicted R^2-values for all the parameters are in reasonable agreement with the adjusted R^2-value; the difference is less than 0.2, except for relative slump flow. The relative slump flow is, however, linked to the flowability as can be seen in **Equation 3-2**. The predicted R^2-value for the initial cracking strength is negative, which implies that the overall mean would be a better prediction for the response. All the R^2-values are greater than 0.80, except for initial cracking strength. The R^2-value for all the parameters is satisfactory and indicates an acceptable adjustment of the models to the experimental data. The Adequate Precision (AD) of the signal-to-noise ratio for all the models is higher than 4, which indicates that the model is desirable (Stat-Ease Inc., 2019., Minneapolis, USA). This also confirms that the models can be used to navigate the design space defined by the CCD. The Standard Deviation (SD), mean value and Coefficient of Variation (CoV) are also shown for the various responses.

Table 3-8: Model validation for various responses

	Flowability (mm)	**Relative slump flow**	**Air content (%)**	**Density (kg/m^3)**
SD*	29.3	0.46	0.32	8.92
Mean	280	1.06	5.51	2501
R^2	0.84	0.87	0.77	0.96
Predicted R^2	0.67	0.50	0.59	0.92
Adjusted R^2	0.80	0.81	0.71	0.94
CoV (%)*	10.5	43.6	5.88	0.36
AD*	12.5	11.2	9.76	24.8

	7-day compressive strength (MPa)	**28-day compressive strength (MPa)**	**Rand/MPa**	**Cement content/MPa**
SD*	2.48	3.42	1.07	0.08
Mean	117.2	158	54.9	3.45
R^2	0.89	0.83	0.99	0.86
Predicted R^2	0.80	0.64	0.98	0.71
Adjusted R^2	0.87	0.79	0.99	0.83
CoV (%)*	2.12	2.17	1.96	2.22
AD*	15.4	11.9	59.5	13.6

	Modulus of elasticity (GPa)	**Initial cracking strength (MPa)**	**Maximum tensile strength (MPa)**
SD*	0.39	0.16	0.87
Mean	52.2	7.80	17.1
R^2	0.96	0.43	0.89
Predicted R^2	0.72	-0.18	0.81
Adjusted R^2	0.92	0.29	0.86
CoV (%)*	0.75	7.86	5.09
AD*	14.0	4.66	15.3

**SD = Standard Deviation, CoV = Coefficient of Variance, AD = Adequate Precision*

3.7.2 Flowability

The surface plot for the flow of the fresh UHPFRC mixtures is shown in **Figure 3-10 (a)**. The data illustrates the variation of the flow of UHPFRC with different short straight fibre and superplasticiser contents. The flow varied between 180 mm and 430 mm. A linear model was used and the R^2-value for the surface plot was 0.84. It is clear from the surface plot that both the fibre and superplasticiser content play a significant role in the flowability of the fresh concrete. The surface plot for relative slump of the fresh UHPFRC mixtures is shown in **Figure 3-10 (b)**. The data illustrates the variation of relative flow of UHPFRC with different short straight fibre and superplasticiser contents. The relative slump value varied between 0.16 and 3.7. A second-order two-factor interaction model (2FI model) was used and the R^2-value for the surface plot was 0.87. It is important to note that, with the addition of superplasticiser, the relative slump value of the UHPFRC increases only at lower fibre contents. With the addition of fibres, both the flow and relative slump value reduce. This can be attributed to the increase in cohesive forces between the concrete matrix and fibres. Although increased fibre content or decreased superplasticiser content reduced the flowability, all mixtures were sufficiently workable as to allow placement and compaction of concrete specimens.

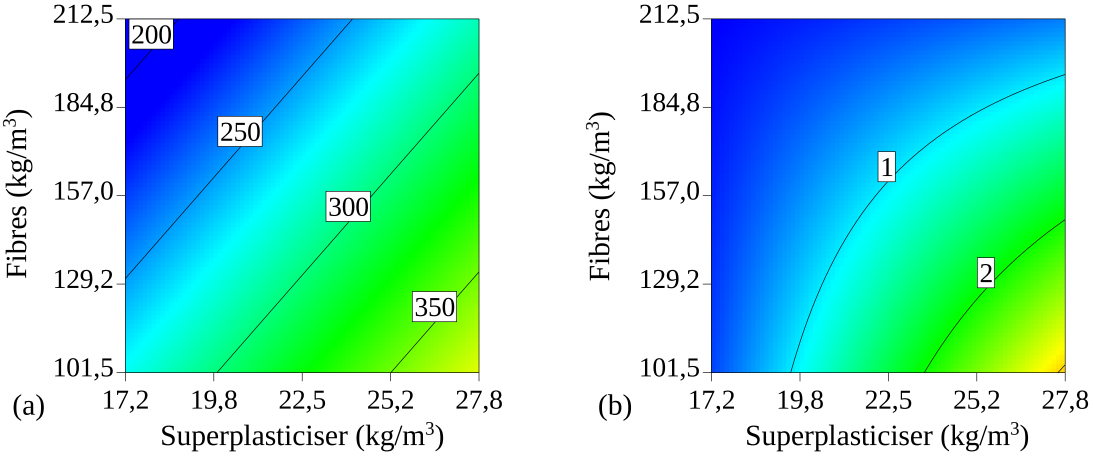

Figure 3-10: Surface plot for (a) flow in mm and (b) relative slump flow

3.7.3 Density

The density obtained from the UHPFRC cubes is illustrated in **Figure 3-11 (a)**. The data shows the variation of the density of the UHPFRC with different short straight fibre and superplasticiser contents. The density varied between 2430 kg per m^3 and 2550 kg per m^3. A linear model was used and the R^2-value for the surface plot was 0.96. It is important to note that the density decreased with the addition of superplasticiser and increased with the addition of fibres. The densest mixes obtained were the ones with high fibre amounts and low superplasticiser contents.

3.7.4 Air content

The air content obtained from the UHPFRC cubes is illustrated in **Figure 3-11 (b)**. The difference between the theoretical density and measured density was used to calculate the air content. The data shows the variation of the air content of the UHPFRC with different short straight fibre and superplasticiser contents. The air content varied between 4.66 % and 6.51 %. A linear model was used and the R^2-value for the surface plot was 0.77. As expected, high superplasticiser content entrains air. From the figure, it can also be seen that fibre content plays a role in the amount of entrained air. Both high superplasticiser and fibre content increased the amount of entrained air. With an increased air content, flowability, density and strength of the concrete could be reduced as stated in literature. Even though a higher density is observed with the addition of fibres, particle packing decreased. This can be attributed to the increased entrained or entrapped air content with the addition of fibres.

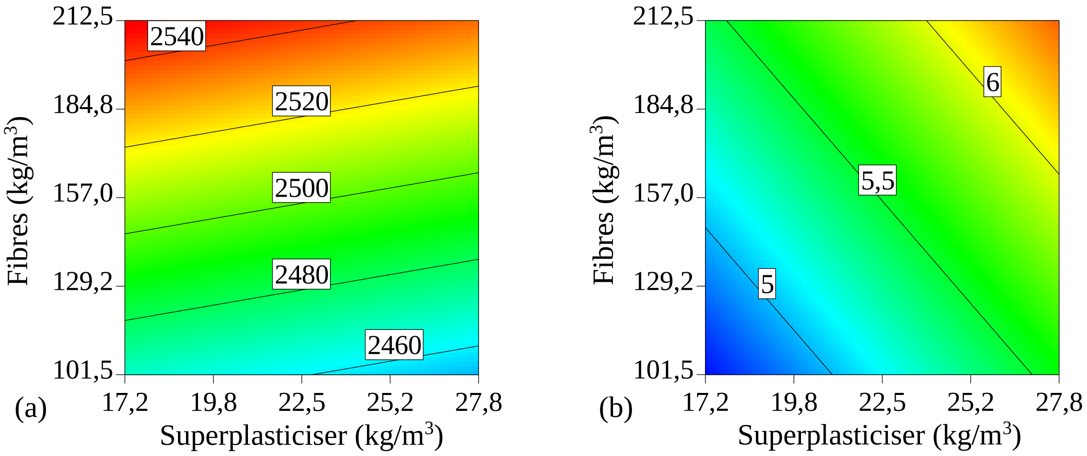

Figure 3-11: Surface plot for (a) density in kg/m^3 and (b) air content in %

3.7.5 Compressive strength

The cube compressive strength (100 x 100 x 100 mm cube) of the UHPFRC mixes is illustrated on the surface plots in **Figure 3-12**. The seven-day compressive strength varied between 106 MPa and 126 MPa. A linear model was used and the R^2-value for the surface plot was 0.89. The twenty-eight-day compressive strength varied between 144 MPa and 168 MPa. A linear model was used and the R^2-value for the surface plot was 0.83. The addition of fibres significantly improved the compressive strength of the UHPFRC. However, the addition of superplasticiser slightly decreased the compressive strength of the UHPFRC.

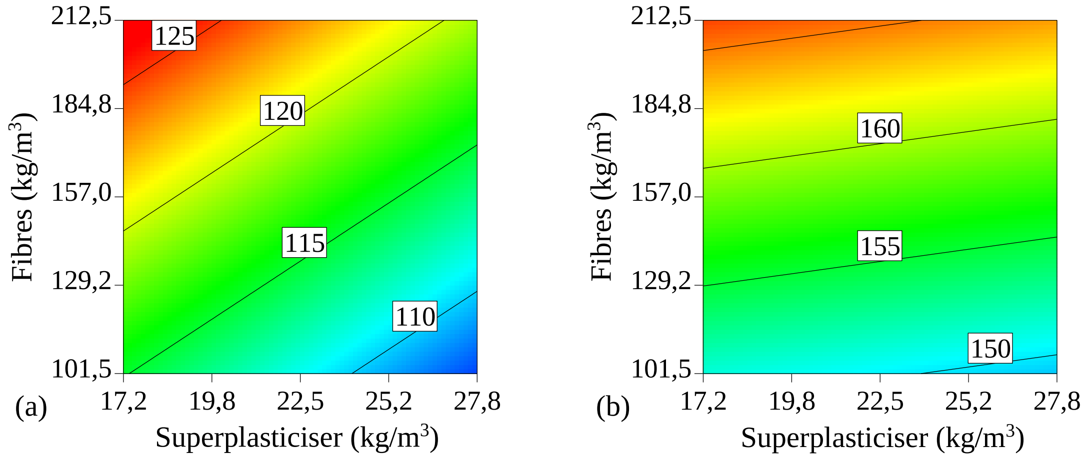

Figure 3-12: Surface plot for (a) the 7-day compressive strength in MPa and (b) the 28-day compressive strength in MPa

The surface plot for Rand per MPa of the compressive strength is illustrated in **Figure 3-13 (a)**. A linear model was used and the R^2-value for the surface plot was 0.99. Since the fibres used in this study cost R40.50 per kg (refer to **Table 3-6**), it is understandable why the increase of fibre content plays such a significant role in the Rand per MPa. It is important to note that the Rand per MPa value slightly decreases with an increase in superplasticiser content. Thus, an increase in superplasticiser content and a decrease in fibre content will increase workability and decrease the cost per MPa. The surface plot for cement content per MPa of compressive strength is illustrated in **Figure 3-13 (b)**. A linear model was used and the R^2-value for the surface plot was 0.86. The cement per MPa value decreases with an increase in fibre content and slightly decreases with a decrease in superplasticiser content. The surface plot illustrates that the fibre content plays a significant role in the cement content per MPa value.

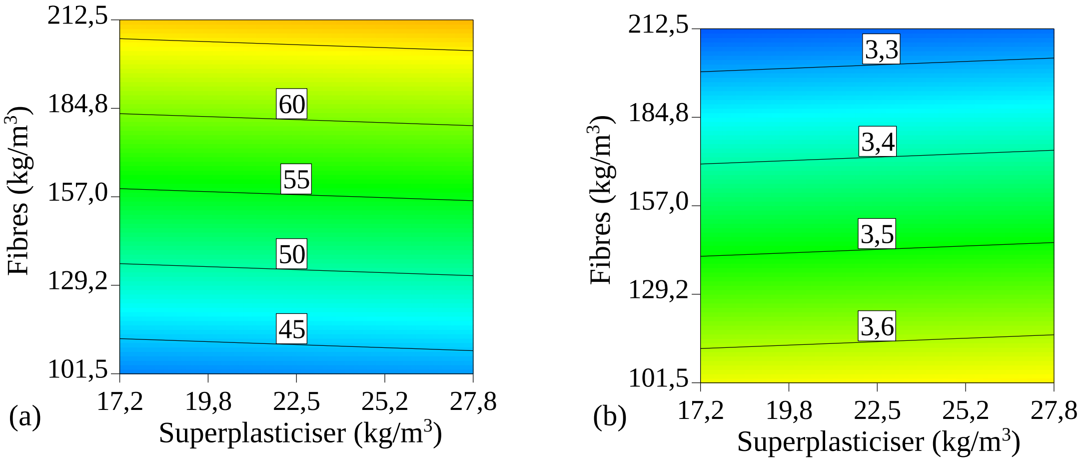

Figure 3-13: Surface plot for (a) Rand/MPa (compressive strength) and (b) cement content/MPa (compressive strength)

3.7.6 Modulus of elasticity

As the water-cement ratio, aggregate type and aggregate size were kept constant for all the mixes, the difference in modulus of elasticity between the mixes was expected to be small. The modulus of elasticity for the UHPFRC mixes varies between 49.5 GPa and 53.0 GPa and is illustrated in **Figure 3-14**. A quadratic model (second order polynomial) was used and the results obtained a R^2-value of 0.96. It was observed that the addition of different steel fibre or superplasticiser contents did not influence the elastic modulus. The difference between all the mixes was deemed to be insignificant.

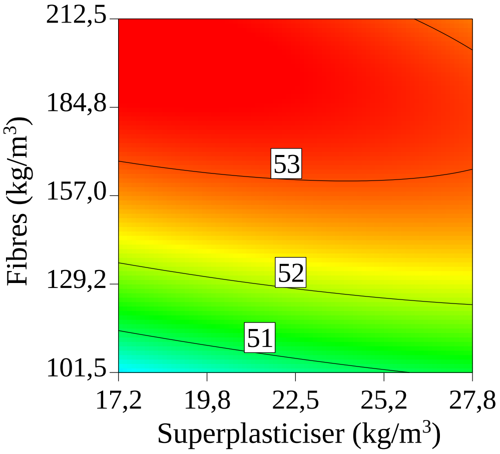

Figure 3-14: Surface plot for the modulus of elasticity in GPa

3.7.7 Splitting tensile strength

The splitting tensile strength results of the UHPFRC mixes are shown on the surface plot in **Figure 3-15**. The initial cracking strength varied between 6.0 MPa and 8.7 MPa. A linear model was used and the R^2-value for the surface plot was 0.43. Design Expert® software did, however, state that the overall mean value would be a better estimation for the response. The mean value for the initial cracking strength was 7.8 MPa. The maximum tensile strength varied between 13.6 MPa and 20.5 MPa. A linear model was used and the R^2-value for the surface plot was 0.89. The addition of fibres significantly improved the maximum tensile strength of the UHPFRC. On the other hand, the addition of superplasticiser slightly decreased the maximum tensile strength of the UHPFRC. The maximum tensile strength results follow the same trend as the compressive strength results.

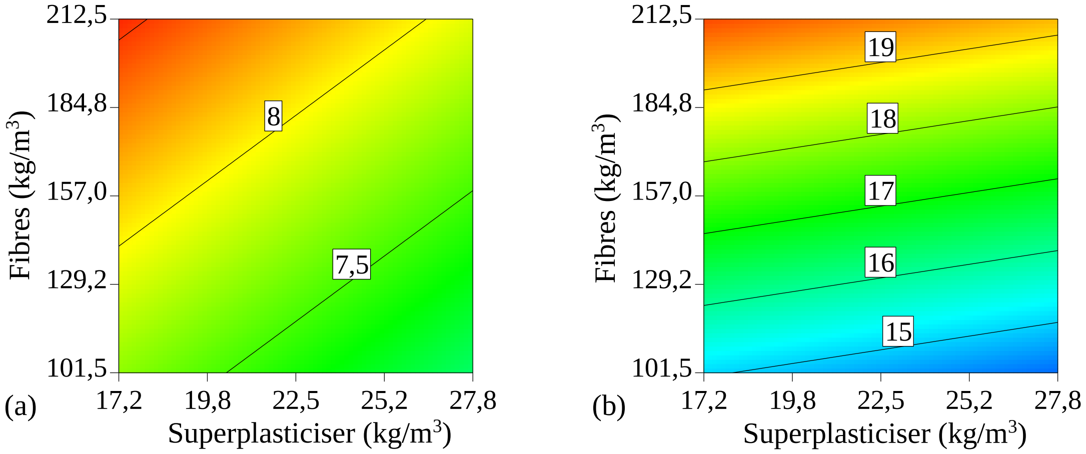

Figure 3-15: Surface plot for (a) the initial cracking strength in MPa and (b) the maximum splitting tensile strength in MPa

3.8 CONCLUSIONS

The UHPFRC was appropriately designed, produced and tested. Using the modified Andreasen and Andersen particle packing model together with response surface design methodology, a dense UHPFRC with a relatively low binder amount, low fibre content and good workability was produced. The superplasticiser content can be increased if a more workable mix is required without decreasing the strength significantly. The statistical analysis of the RSM confirms that the designed models can be used to navigate the design space defined by the CCD. With the addition of fibres, the following conclusions can be drawn:

- Significantly increased cost/m^3.
- Flow reduced.
- Density increased.
- Air content increased.
- Particle packing decreased due to the increased entrapped or entrained air content.
- No significant effect on the initial cracking strength.
- Compressive and splitting tensile strength increased.
- No significant effect on the modulus of elasticity.

With the addition of superplasticiser, the following conclusions can be drawn:

- Flow increased.
- Density decreased.
- Air content increased.
- No significant effect on the initial cracking strength.
- Little effect on the compressive and splitting tensile strength.
- No significant effect on the modulus of elasticity.

4 EXPERIMENTAL SET-UP FOR OPTIMISED MIXTURE

4.1 INTRODUCTION

In this study, an optimised UHPC matrix was developed while using available South African materials. The optimum combined superplasticiser and fibre content for the UHPC were determined by taking material cost into account and using a response surface design. The mechanical properties as well as volume change due to drying shrinkage and creep were established for the optimised mixture. The flexural performance of the small UHPFRC beams (50 x 100 x 2000 mm) was determined together with their maximum load carrying capacity. The experiments were carried out in the Civil Engineering laboratory of the University of Pretoria.

4.2 FINAL OPTIMISED MIXTURE COMPOSITION

The final mixture composition was obtained by using Design-Expert® software. In the numerical optimisation, superplasticiser and fibre content were set in the range where the cost was minimised, taking into consideration the flow, compressive strength, modulus of elasticity and splitting tensile strength. The criteria used to optimise the mix design is tabulated in **Table 4-1**.

Table 4-1: Criteria for optimisation

Parameter	Specification	Reference
Flow	≥ 300 mm	-
28-day compressive strength	≥ 150 MPa	Habel et al. (2008)
Splitting tensile strength	≥ 16.5 MPa	Meng et al. (2017)
E-value	≥ 52 GPa	Meng et al. (2017)
Cost/m^3	≤ R 8500.00	Wille & Boisvert-Cotulio (2015)

The responses obtained from the CCD were used to optimise the combination of fibres and superplasticiser to give the optimum performance in terms of acceptable mechanical properties. Considering the criteria to obtain the optimum performance, as specified in **Table 4-1**, an overlay plot was drawn and is shown in **Figure 4-1**. Thereafter, a fibre content and superplasticiser content were chosen to meet the criteria specified (i.e. fall inside the blue triangle) as indicated with a flag in the surface plot. The final optimised mix design is tabulated in **Table 4-2**.

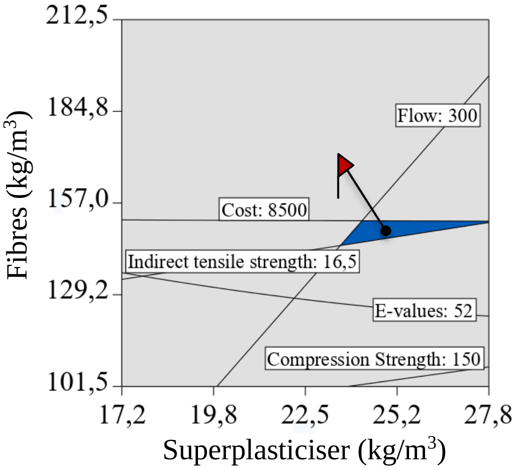

Figure 4-1: Overlay plot

Table 4-2: Mix composition for the final optimised mix (kg/m^3)

Material	**kg/m^3**	**Relative Density**
Cement	542	3.14
Undensified Silica Fume	146	2.45
Unclassified Fly Ash	146	2.22
Water	146	1.00
Dolomite Stone	251	2.91
Dolomite Sand	1005	2.85
Silica Sand	216	2.67
Superplasticiser	25.6	1.06
Short Straight Fibres	149	7.85

The mechanical properties for the optimised mixture were tested to confirm the accuracy of the estimated model. The absolute relative deviation (ARD) (%) was calculated as a measure of predictability. The lower the ARD (%), the better agreement is obtained between experimental and estimated values (Ghafari et al., 2015a). The equation to determine the ARD (%) is described in **Equation 4-1**.

$$ARD\ (\%) = \frac{Experimental-Model}{Experimental} \times 100 \qquad \textbf{Equation 4-1}$$

Values for flow, density, compressive strength, modulus of elasticity and splitting tensile strength results were estimated for the chosen final optimised mix from the various surface plot results obtained in **Chapter 3.6** (see **Table 4-3**).

Table 4-3: Estimated properties for the final optimised mixture

Parameter	Property (estimated from surface plot)
Flow (mm)	310
Density (kg/m^3)	2490
Air content (%)	5.75
Seven-day compressive strength (MPa)	144
Twenty-eight-day compressive strength (MPa)	156
Modulus of elasticity (GPa)	52.7
Splitting tensile strength (MPa)	16.6

4.3 SPECIMENS CAST

The same mixing procedure as set out in **Chapter 3.5** was used. The specimens cast, number of specimens cast, curing regime considered and the day of testing are tabulated in **Table 4-4**. Microstructure studies were also conducted on the concrete specimens cast, to look at the arrangements of hydrated and unhydrated particles in the UHPFRC under different curing conditions using SEM.

Table 4-4: Specimens cast for final optimised mix

Parameter	Specimens cast	Amount	Curing regime	Testing days
Compressive strength	100 mm cubes	15	25 °C Water	3, 7, 28, 56, 90
		15	80 °C Water	28
Compressive strength	50 mm cubes	9	25 °C Water	28, 56, 90
E-value	Cylinders	3	25 °C Water	28
		3	80 °C Water	
Splitting tensile strength	-	-	-	28
Direct tensile strength	Dog bones	3	25 °C Water	28
Flexural tensile strength	MOR beams	3	25 °C Water	28
Specimen size effect	Modified beams	12	25 °C Water	28
Creep and shrinkage	Cylinders	3	25 °C Water	28

4.4 CURING REGIME

All the specimens were cast and then left to cure under a curing blanket in a temperature-controlled room (25 °C) for one day. After one day, all the specimens, except for fifteen cubes and three cylinders, were demoulded and placed in a 25 °C water bath until the day of testing. The other fifteen cubes and three cylinders were demoulded and placed in a different curing bath with the current water temperature at 25 °C to ensure that no thermal shocking took place.

The temperature of the water for this bath was then set to go up gradually to 80 °C (±8 °C/hour). The specimens were left for 48 hours to cure. Thereafter, the temperature of the 80 °C water bath was set back to 25 °C and the water temperature gradually returned to 25 °C (±8 °C/hour). All the specimens were then left to cure in the 25 °C water bath until the day of testing.

4.5 MECHANICAL PROPERTIES

4.5.1 Compressive strength

The compression test specimens consisted of 50 x 50 x 50 mm cubes and 100 × 100 × 100 mm cubes (see **Figure 4-2**). The cube compressive strength was determined according to SANS 5863:2006. The same procedure was followed to measure the modulus of elasticity as discussed in **Chapter 3.6.2**. The standard compression test provides only a single peak value (not a stress-strain response) for the compressive strength of the concrete.

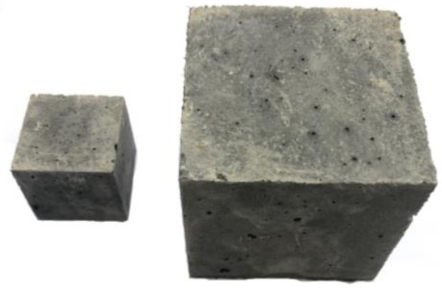

Figure 4-2: 50 mm cube vs 100 mm cube

Domone & Illston (2010) state that the twenty-eight-day strength of concrete is usually used to characterise the concrete for design and specification purposes. Characteristic concrete strength (f_{cu}) is an important concept. This concept is taken from the theory of probability. The concrete strength used in calculations should not be the mean strength determined from a series of cube crushing tests. The strength should rather be much lower than the mean. The spread of cube crushing results will follow a normal distribution curve, as shown in **Figure 4-3**. The value of f_k is defined so that the shaded area below f_k is 5 % (EN 1992-1-1) of the total area below the curve. This means that there is a one in twenty chance of any test result falling below f_k. According to Hurst (2003), this is an acceptable probability. **Equation 4-2** was used to determine this characteristic cube strength.

$$f_{cu} = f_{cm} - 1.64SD \qquad \textbf{Equation 4-2}$$

where f_{cu} is the characteristic cube strength, f_{cm} is the average cube strength and SD is the Standard Deviation.

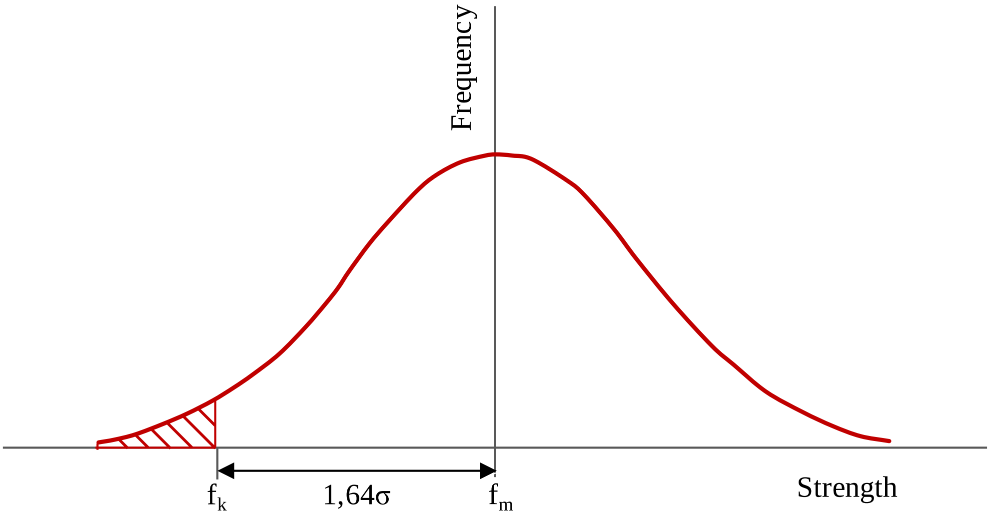

Figure 4-3: Concrete strength distribution (adapted from Hurst, 2003)

According to Soutsos et al. (2018) all the existing maturity functions used to estimate the strength development of concrete does not incorporate the detrimental effect of high curing temperatures on long-term strength and therefore all of them overestimate the long-term strengths. The development of strength with time was predicted using **Equation 4-3** (*fib* Model Code 2010, 2013).

$$f_{cm}(t)=\beta_{cc}(t)\times f_{cm} \qquad \textbf{Equation 4-3}$$

with:

$$\beta_{cc}(t)=exp\left[s\times\left(1-\left(\frac{28}{t}\right)^{0.5}\right)\right] \qquad \textbf{Equation 4-4}$$

where f_{cm} is the mean compressive strength in MPa at an age t in days, $f_{cm}(t)$ is the mean compressive strength in MPa at an age of twenty-eight-days, $\beta_{cc}(t)$ is a function to describe the strength development with time, t is the concrete age in days adjusted according to **Equation 4-5** (taking into account the temperature during curing) and s is a coefficient which depends on the strength class of cement as given in **Table 4-5**. However, Vollpracht et al. (2018) state that no guidance is provided for the s coefficient for supplementary cementitious materials. Concrete containing high fly ash contents will result in slower strength development, which leads to higher s coefficients. Vollpracht et al. (2018) state that an s coefficient of 0.382 should be used for concrete mixes with 30 % cement replacement with fly ash. The effect of elevated or reduced temperatures on the maturity of concrete may be considered by adjusting the concrete age with **Equation 4-5** (*fib* Model Code 2010, 2013).

$$t_{T=} \sum_{i=1}^{n} \Delta t_i \, exp\left[13.65 - \frac{4000}{273+T(\Delta t_i)}\right]$$ **Equation 4-5**

where t_T is the temperature-adjusted concrete age, which replaces t in the corresponding equation in days, Δt_i is the number of days where a temperature T prevails, and $T(\Delta t_i)$ is the mean temperature in °C during the time period Δt_i.

Table 4-5: Coefficients to be used in Equation 4-4 for different types of cement (*fib* Model Code 2010, 2013)

f_{cm} (MPa)	Strength class of cement	s
	32.5 N	0.38
≤ 60	32.5 R, 42.5 N	0.25
	42.5 R, 52.5 N, 52.5 R	0.20
> *60*	All classes	0.20

4.5.2 Modulus of elasticity

The E-value test specimens consisted of 100 × 200 mm cylinders. The modulus of elasticity was determined as discussed in BS EN 1239-13:2013. The same procedure was followed to measure the modulus of elasticity, as discussed in **Chapter 3.6.2**.

4.5.3 Direct tensile strength

The specimens used in the direct tensile test consisted of three 50 mm thick un-notched dog bone-shaped specimens with geometry and set-up as shown in **Figure 4-4**. The specimens were placed in a displacement controlled hydraulic tensile load frame with a maximum capacity of 300 kN. A 50 mm clip gauge was used to measure the extension of the specimen as well as to capture potential crack development, strain hardening and strain softening. The equipment and set-up did not allow for more than one clip gauge and therefor it was not possible to determine whether the specimen was tested in pure tension. A pin-fixed support system was used to minimise the secondary moment.

4.5.4 Splitting tensile strength

The splitting tensile test specimens consisted of the top and bottom halves of the cylinders used in the E-value test. The adjusted splitting tensile test procedure was used in accordance with the recommendations by Denneman (2011). Splitting tensile strengths were calculated as discussed in SANS 6253:2006. The same procedure was followed to measure the splitting tensile strength, as discussed in **Chapter 3.6.3**.

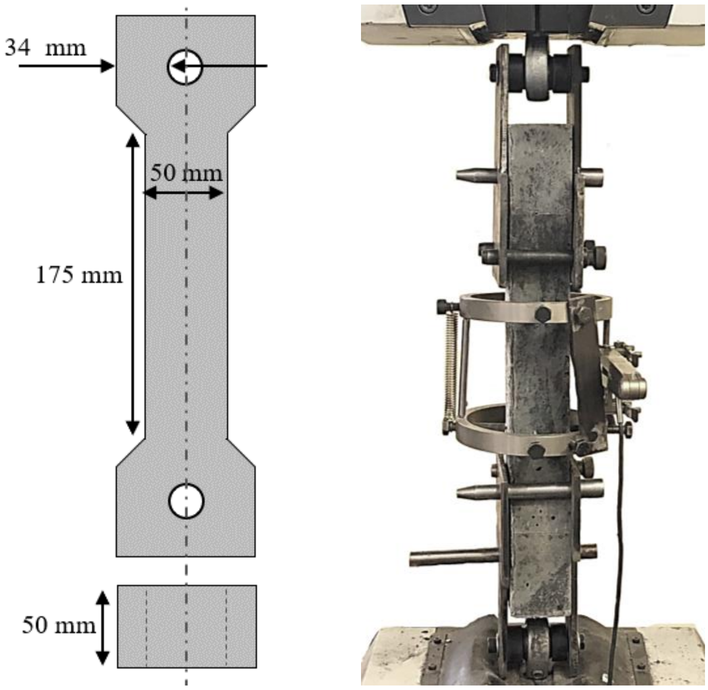

Figure 4-4: Direct tensile test specimen geometry and set-up

4.5.5 Flexural tensile strength

The Modulus of Rupture (MOR) test was conducted to determine the flexural tensile strength by using a four-point-flexural prism test with a span length of 300 mm, as described in SANS 5864:2006 (see **Figure 4-5** for test set-up). The MOR test specimens consisted of three 100 × 100 × 500 mm beams. The beams were tested until failure in order to determine their flexural tensile strength. In order to obtain the load-deflection curve, the vertical displacement at mid-span was measured by using Linear Variable Differential Transducers (LVDTs) at either side of the beam. Both the LOP and the peak load (MOR) was then determined from the results obtained. The set-up was running in displacement control mode, which was set at 0.1 mm per minute. The assumption of a linear-elastic stress state to determine the flexural tensile strength was assumed even though the stress state in UHPFRC after cracking would be highly nonlinear. The flexural tensile strength value does not reflect the reality but allow a comparison between different types of UHPFRC. The flexural tensile strengths (f_b) were calculated using the equation, as proposed in SANS 5864:2006:

$$f_b = \frac{PL_{span}}{bh^2}$$ **Equation 4-6**

where P is the failure load, L_{span} is the span length, b is the sample width, and h is the sample depth. The flexural toughness was determined to three significant digits from the area below the load-deflection curve until the measured deflection reached 1/150 of the span as described in JSCE-SF4:1984. According to Yu et al. (2015b), the JSCE-SF4:1984 standard is more suitable to evaluate the flexural toughness of UHPFRC than ASTM C1018-97. Flexural toughness should be expressed as flexural toughness factor (JSCE-SF4:1984). The flexural toughness factor was calculated by using **Equation 4-7**, as discussed in JSCE-SF4:1984. Although this equation is not valid for strain hardening results, it allows a comparison between different types of UHPFRC.

$$TF = \frac{T_b}{\delta_{tb}} \cdot \frac{L_{span}}{bh^2}$$ **Equation 4-7**

where TF is the flexural toughness factor, T_b is the flexural toughness and δ_{tb} is the deflection of 1/150 of the span.

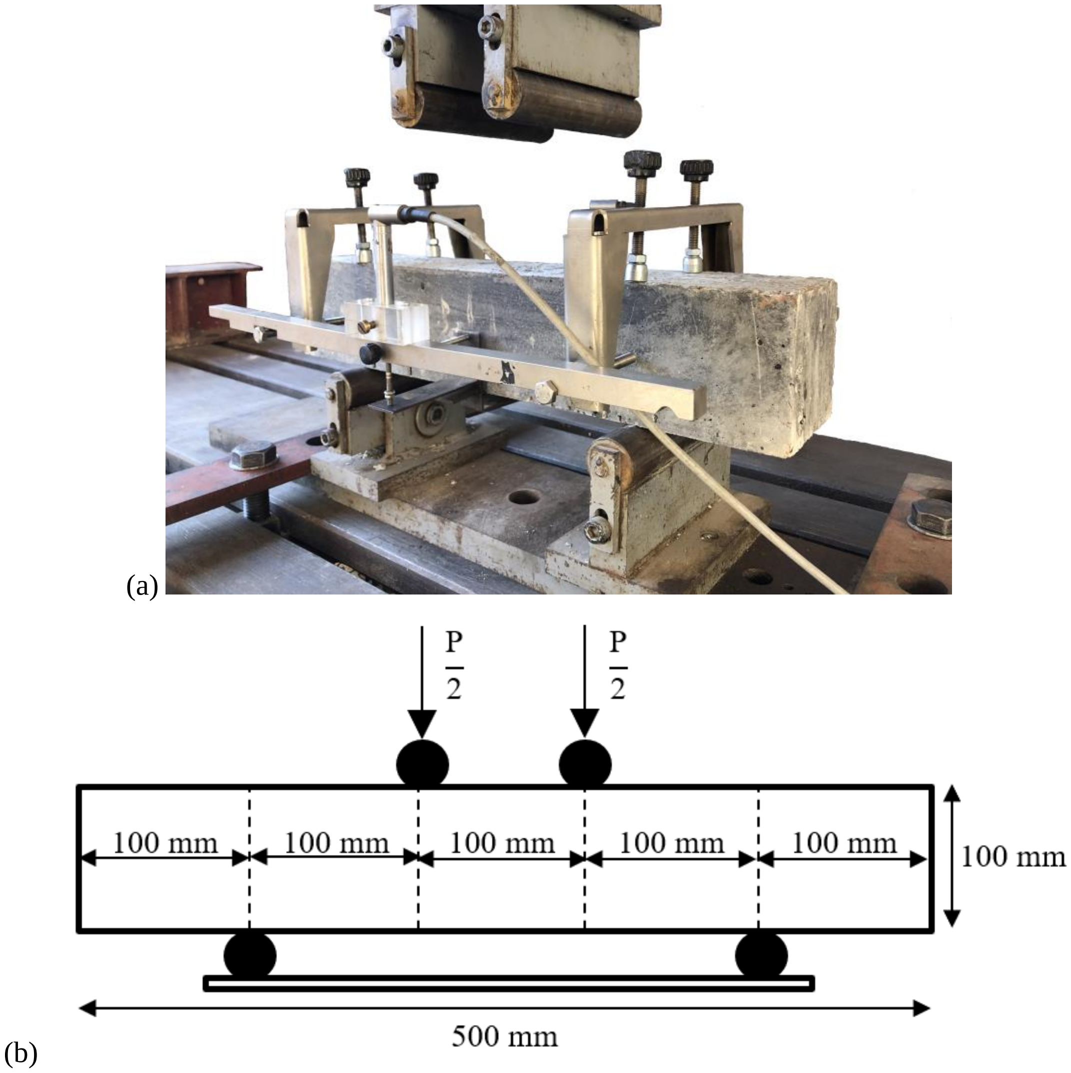

Figure 4-5: (a) MOR test set-up and (b) schematic of test set-up and dimensions

4.5.6 Size effect of small experimental beams

The size effect of small experimental beams was also considered. The MOR test moulds was altered so that 4 beams with different depths were cast. The specimens had the following dimensions: 100 × 60 × 500 mm, 100 × 45 × 500 mm, 100 × 30 × 500 mm and 100 × 15 × 500 mm (see **Table 4-6**). A four-point bending test was conducted to determine the flexural strength of the beams with a span length of 300 mm. The flexural tensile strength and flexural toughness of all beams were determined using **Equation 4-6** and **Equation 4-7**.

Table 4-6: Specimen dimensions

	Dimensions (b x h x L - mm)*	**Second moment of area (I – mm^4)**	**Span-to-depth ratio (L_{span}/h)**
Type 1	100 x 100 x 500	8.333×10^6	3.0
Type 2	100 x 60 x 500	1.800×10^6	5.0
Type 3	100 x 45 x 500	0.759×10^6	6.7
Type 4	100 x 30 x 500	0.225×10^6	10
Type 5	100 x 15 x 500	0.028×10^6	20

**b: width, h: depth, L: length*

4.5.7 Creep and Shrinkage

Three concrete 75 × 300 mm creep and shrinkage cylinders were cast and cured for twenty-eight days. The creep rig was loaded to approximately 15 % of the cylinder strength after twenty-eight days (maximum capacity of creep rig). The rig set-up was placed in a temperature-controlled room at 25 ± 2 °C and 65 ± 5 % relative humidity. The set-up of the creep rig is illustrated in **Figure 4-6**. A LVDT was mounted between the two collars (200 mm length apart) to measure the change in length of the sample. Readings were taken every two minutes for ninety days.

4.6 SMALL EXPERIMENTAL BEAMS

One of the main objectives of this research was to study the flexural performance of the UHPFRC beams and to determine their maximum load carrying capacity. Two 2000 × 50 × 100 mm beams and two 2000 × 100 × 50 mm beams (see **Table 4-7**) were cast from the final optimised mix design and tested to determine their flexural behaviour and ultimate load capacity. No additional reinforcing was cast into the beams and the beams did not include any shear reinforcement. The four beams were cured in a water bath (25 °C) until the day of testing. The test was conducted by using a four-point bending test with a span length of 1.8 m. A 5 kN load cell was used to measure the applied load. Two LVDTs were attached (at mid-span of the beams) to measure the deflection as the load was applied. The test set-up is shown in **Figure 4-7**.

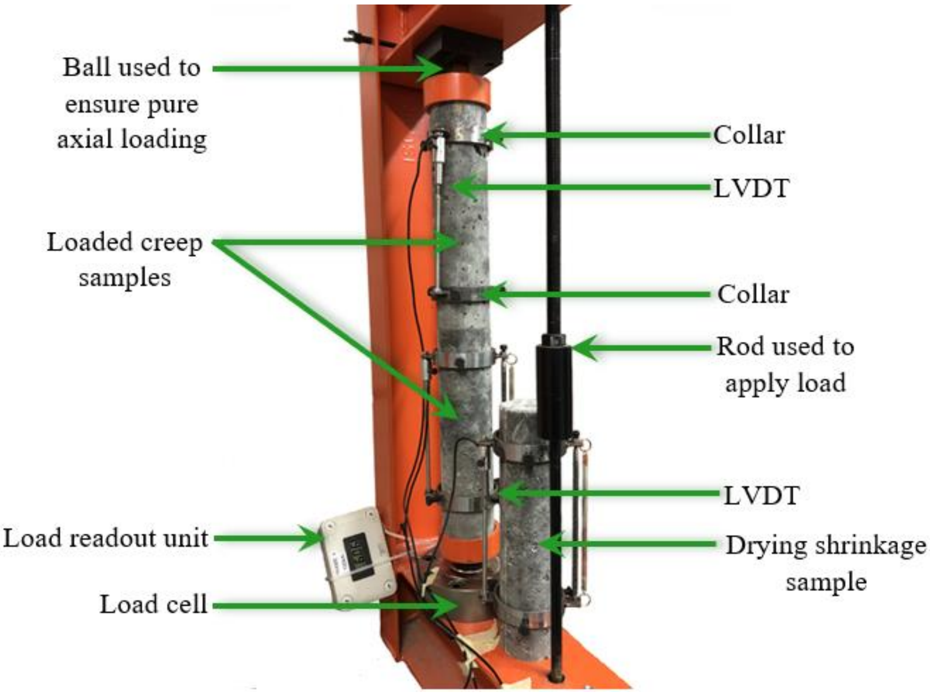

Figure 4-6: Creep and shrinkage rig set-up

Table 4-7: Beam information

	Dimensions (b x h x L - mm)*	**Second moment of area (I – mm^4)**	**Span-to-depth ratio (L_{span}/h)**
Beam 1	50 x 100 x 2000	4.167 x 10^6	18
Beam 2	50 x 100 x 2000	4.167 x 10^6	18
Beam 3	100 x 50 x 2000	1.042 x 10^6	36
Beam 4	100 x 50 x 2000	1.042 x 10^6	36

**b: width, h: depth, L: length*

Figure 4-7: (a) 50 x 100 x 2000 mm beam and (b) 100 x 50 x 2000 mm test set-up

5 EXPERIMENTAL RESULTS FOR OPTIMISED MIXTURE

5.1 FLOWABILITY

The flow obtained for the fresh optimised UHPFRC mixture was 310 mm. The estimated flow as obtained from the surface plot in **Chapter 4.2** was 310.4 mm. The difference between the actual flow and estimated flow was deemed insignificant.

5.2 DENSITY

The average density obtained from the 100 mm cubes (before testing) of the final optimised UHPFRC mixture was 2481 kg per m^3. The estimated density as obtained from the surface plot (see **Chapter 4.2)** was 2491 kg per m^3. The difference between the actual density obtained and estimated density is 10 kg per m^3.

The average cube densities obtained from the final optimised mix are tabulated in **Table 5-1**. The difference caused by curing conditions was deemed insignificant. This illustrates that thermal curing has no effect on cube density.

Table 5-1: Cube density (kg/m^3)

Days	25 °C water bath curing	80 °C water bath curing
3	2484	2484
7	2470	2470
28	2481	2471
56	2482	2483
90	2494	2494

5.3 AIR CONTENT

The average air content obtained from the 100 mm cubes of the final optimised UHPFRC mixture was 5.5 %. The estimated air content as obtained from the surface plot (see **Chapter 4.2)** was 5.75 %. The difference between the actual air content obtained and estimated air content was 0.25 %. The difference was deemed insignificant.

The average air content obtained from the final optimised mixture is tabulated in **Table 5-2**. The difference caused by curing conditions was deemed insignificant. This illustrates that thermal curing has no effect on air content.

Table 5-2: Air content (%)

Days	25 °C water bath curing	80 °C water bath curing
3	5.4	5.4
7	6.0	6.0
28	5.5	5.9
56	5.5	5.5
90	5.1	5.1

5.4 COMPRESSIVE STRENGTH

The estimated compressive strength values obtained from the surface plots (see **Chapter 4.2**) will first be compared to the actual compressive strength results, whereafter the actual compressive strength results will be compared to the predicted compressive strength results obtained from the *fib* Model code 2010 (2013).

The average seven-day cube compressive strength (25 °C water bath curing) for the optimised mix was 111 MPa. The estimation obtained from the surface plot for the seven-day compressive strength as discussed in **Chapter 4.2** was 114 MPa. The difference between the actual seven-day compressive strength and the estimated strength was 3 MPa. The average twenty-eight-day cube compressive strength (25 °C water bath curing) for the optimised mix was 153 MPa. The estimation obtained from the surface plot for the twenty-eight-day compressive strength as discussed in **Chapter 4.2** was 156 MPa. The difference between the actual twenty-eight-day compressive strength and the estimated strength was 3 MPa. These results indicate that the compressive strength was estimated to within 5 % when using the estimated values obtained from surface plots.

The results for the average compressive strengths, predicted compressive strengths (*fib* Model code 2010, 2013) and characteristic cube strength are tabulated in **Table 5-3** and **Table 5-4**. The SD obtained for the conventional cured specimens (for all ages) was lower compared to the SD for the heat cured specimens. Thus, a higher variability is observed in compressive strength for the heat cured specimens. **Equation 4-2** was used to determine the characteristic cube strength. The characteristic cube strengths calculated for the conventional cured specimens was higher from twenty-eight days onward, compared to the characteristic cube strengths calculated for the heat cured specimens. This is a result of the higher variability observed in the heat cured samples. The short-term and long-term compressive strength were predicted using **Equation 4-3** (*fib* Model code 2010, 2013) and then compared to the actual experimental results.

Table 5-5 includes the strength growth factor due to the higher temperature curing regime. The results show that the strength growth factor decreases with time. The average strength growth factor for three days was 1.78; however, after ninety days, the factor reduced to 0.90. This indicates that the strength for heat cured samples shows little strength development with age.

Table 5-3: 25 °C water bath curing compressive strengths (MPa)

Time (Days)	**3**	**7**	**28**	**56**	**90**
Cube 1 – 100 mm	86.3	110	151	157	164
Cube 2 – 100 mm	84.8	105	156	170	172
Cube 3 – 100 mm	83.3	117	151	165	174
Average	**84.8**	**111**	**153**	**164**	**170**
Standard Deviation	1.23	4.66	2.07	5.03	4.39
Estimated cube strength	101	125	153	162	167
Characteristic cube strength	82.8	103	149	156	163

Table 5-4: 80 °C water bath curing compressive strengths (MPa)

Time (Days)	**3**	**7**	**28**	**56**	**90**
Cube 1 – 100 mm	148	156	152	158	144
Cube 2 – 100 mm	154	152	164	156	157
Cube 3 – 100 mm	151	164	150	146	159
Average	**151**	**157**	**155**	**153**	**153**
Standard Deviation	2.63	5.19	6.19	5.25	6.96
Estimated cube strength	148	151	160	165	168
Characteristic cube strength	147	149	145	145	142

Table 5-5: Strength growth factor ($f_{c\ 80\ °C}$ / $f_{c\ 25\ °C\ average}$)

Time (Days)	**3**	**7**	**28**	**56**	**90**
Cube 1 – 100 mm	1.74	1.41	0.99	0.96	0.84
Cube 2 – 100 mm	1.82	1.37	1.07	0.95	0.92
Cube 3 – 100 mm	1.78	1.49	0.98	0.89	0.94
Average	**1.78**	**1.42**	**1.02**	**0.93**	**0.90**
Standard Deviation	0.03	0.05	0.04	0.03	0.04

The compressive strength development graph of the concrete over a period of ninety days for the final optimised mix is illustrated in **Figure 5-1**. The graph shows both the compressive strength results for the cubes cured in a 25 °C water bath and in an 80 °C water bath. The graph indicates that the strength development for concrete specimens is higher when cured in the conventional 25 °C water bath than for concrete cured in the 80 °C water bath. The cubes cured in the 80 °C water bath reached a maximum strength after seven days of 157 MPa. The cubes cured in the 25 °C water bath show a gradual increase in strength up to ninety days whereas strength of the cubes cured in the 80 °C water bath decreased from seven days to ninety days. This decrease could have been caused by the low strength of one cube, but statistically this cube must still be considered as the value falls within 15 % of the average. If this result is excluded, there would be an increase in strength after twenty-eight days. The low strength could however be attributed to the concrete micro-structure. Curing at elevated temperatures may cause DEF. The late formation of ettringite produces forces that lead to concrete damage, expansive distress and cracking of the concrete could lead to higher variability in cube compressive strength, which was observed for concrete cured at 80 °C.

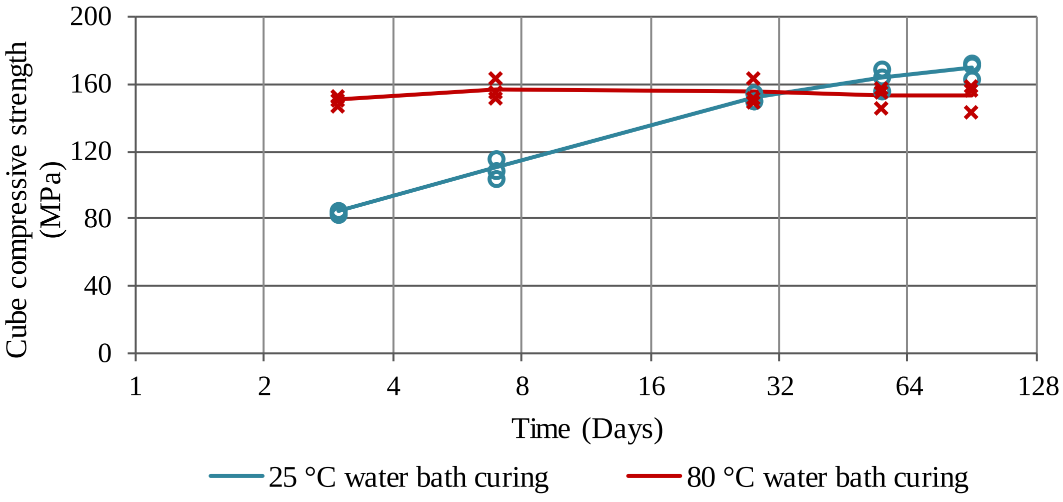

Figure 5-1: Cube compressive strength development graph

The predicted compressive strengths (*fib* Model code 2010, 2013) together with the actual experimental results are compared in **Figure 5-2** (for 25 °C water bath curing) and **Figure 5-3** (for 80 °C water bath curing). Two different *s* coefficients were considered namely, s = 0.2 (*fib* Model code 2010, 2013) and s = 0.382 (Vollpracht et al., 2018). The predicted short-term compressive strengths, when considering *s* = 0.2 (after three days and seven days) for the specimens cured in the 25 °C water bath are not as accurate compared to the long-term compressive strength predictions (see **Figure 5-2**). This is due to the high FA content in the mix composition, which results in reduced compressive strength at an early age and increased strength gain at higher ages. Therefore *s* = 0.382 was also considered, which account for the effect of FA. Accurate short-term predicted compressive strength results were then obtained. The long-term predicted compressive strengths were however over predicted. The estimated early age predicted compressive strengths for the specimens cured in the 80 °C water bath (see **Figure 5-3**) show accurate results compared to the experimental compressive strength for both *s* coefficients. The specimens cured in an 80 °C water bath show reduced experimental compressive strengths with age, whereas both the predicted cube strength graphs increase with age. Thus, the long-term predicted strengths are higher than the actual strengths. This corresponds well with the results obtained by Soutsos et al. (2018), who stated that the predicted strength development of concrete does not incorporate the detrimental effect of high curing temperatures on long-term strength and therefore overestimate the long-term strengths. The strength predictions for both early and long-term ages can be improved by considering this effect in the strength development functions.

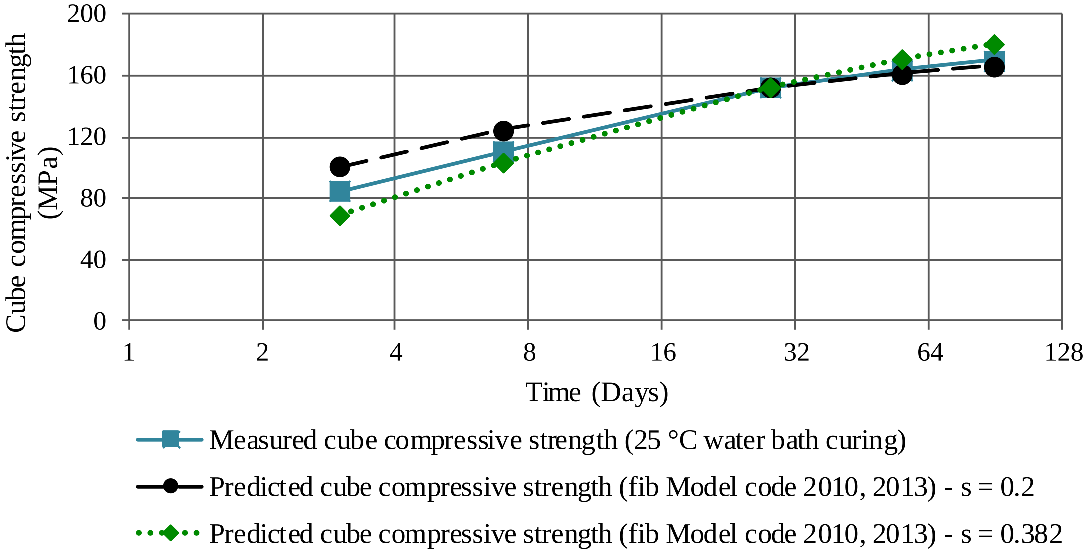

Figure 5-2: Actual cube compressive strength for specimens cured in a 25 °C water bath vs. predicted cube compressive strength (*fib* Model code 2010, 2013)

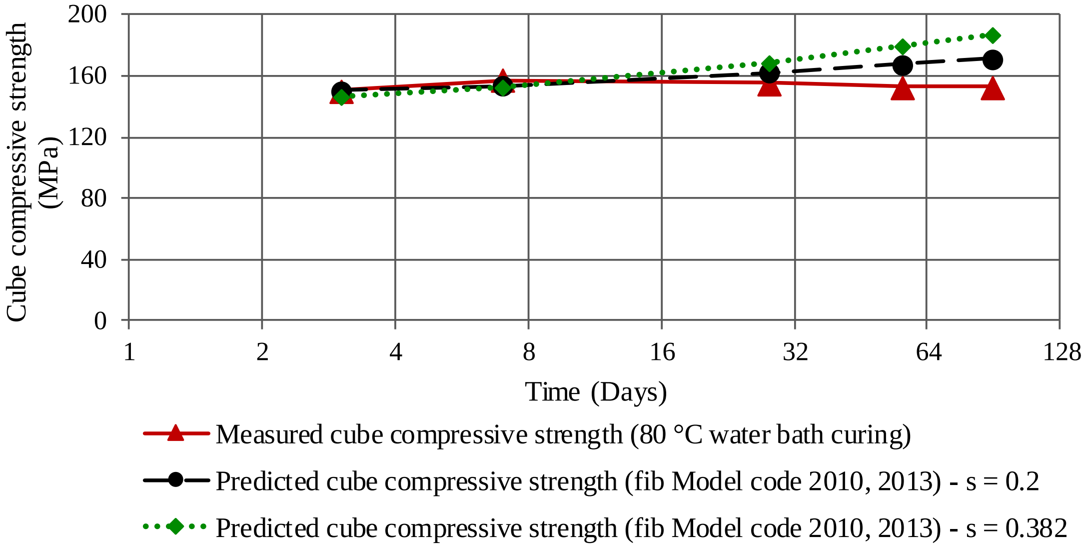

Figure 5-3: Actual cube compressive strength for specimens cured in a 80 °C water bath vs. estimated cube compressive strength

5.4.1 Specimen size effect for compressive strength

Specimen size effect for compressive strength was considered by comparing the compressive strength results of the 100 mm cubes (25 °C water cured) to the 50 mm cubes (25 °C water cured). The compressive strength results obtained for the 50 mm cubes is tabulated **Table 5-6**. Cube 1 for the twenty-eight-day strength was not considered, as this strength differs from other values by more than 15 % of the average and was regarded as unreliable (SANS 5863:2006). The SD obtained decreased with age. The conversion factors calculated for all ages has an average value of 1.10. This corresponds well with Kazemi & Lubell (2012), who obtained a conversion factor of 1.09. **Figure 5-4** illustrates the difference in cube compressive strength for the different specimen sizes. It was found that the specimen size has a significant effect on the measured cube compressive strength. An 11% increase in cube compressive strength after twenty-eight days was observed for specimen sizes of 50 mm compared to those of 100 mm. This can be due to confinement effect or larger size flaws that may be found in larger specimens.

Table 5-6: Specimen size effect for compressive strength

Time (Days)	28	56	90
Cube 1 – 50 mm	~~128.5~~*	174.4	179.0
Cube 2 – 50 mm	181.2	186.3	185.7
Cube 3 – 50 mm	163.3	178.0	178.1
Average	**172.3**	**179.6**	**180.9**
Standard Deviation	8.98	4.98	3.39
Characteristic cube strength	157.5	171.4	175.4
Conversion factor (from 100 mm cube to 50 mm cube)	1.13	1.10	1.06

** Not considered – falls outside 15 % of the average*

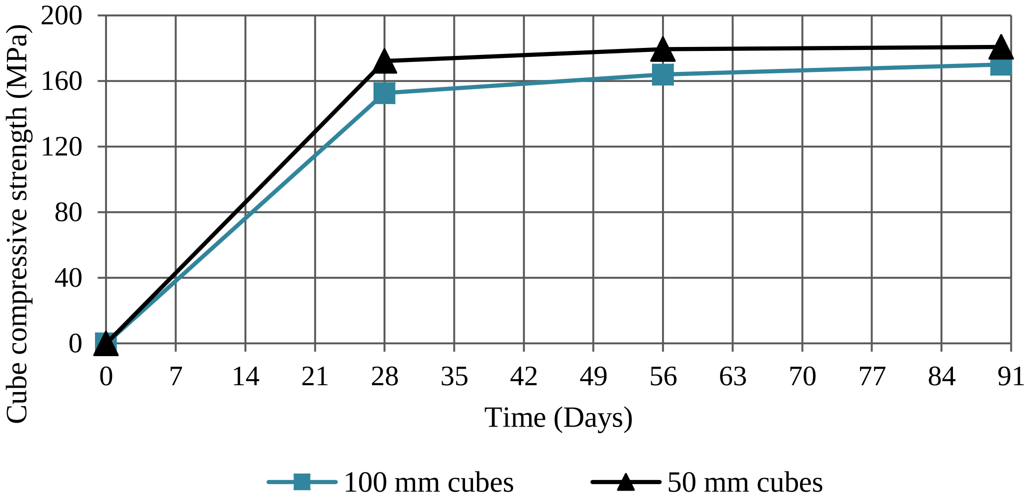

Figure 5-4: Specimen size effect for compressive strength

5.5 MODULUS OF ELASTICITY

The average twenty-eight-day E-value (25 °C water bath curing) for the optimised mix was 54.2 GPa. The estimation for the twenty-eight-day E-value as discussed in **Chapter 4.2** was 52.7 GPa. The difference between the actual E-value and the estimated E-value is 1.5 GPa, which is deemed to be insignificant.

The E-value results for the final optimised mix are tabulated in **Table 5-7**. The table shows both the twenty-eight-day E-value results for the cylinders cured in a 25 °C water bath and in an 80 °C water bath. The elastic modulus should increase with age and decreasing water-cement ratio of the concrete (Domone & Illston, 2010). These two factors thus lead to a slight increase in modulus of elasticity with an increase in compressive strength. From **Figure 5-1**, it was concluded that there is no significant difference in the twenty-eight day compressive strengths for specimens cured in the 25 °C water bath and the 80 °C water bath (SD of 1.95 GPa). The cylinders cured in the 80 °C water bath yielded a slightly lower value compared to the cylinders cured in the 25 °C water bath.

Table 5-7: Elastic modulus (GPa)

	25 °C water bath curing	**80 °C water bath curing**
Cylinder 1	55.1	51.1
Cylinder 2	53.3	50.2
Cylinder 3	54.1	51.3
Average	**54.2**	**50.9**
Standard Deviation	0.75	0.48

5.6 DIRECT TENSILE STRENGTH

An average direct tensile strength (uniaxial tension) of 6.92 MPa, with an average critical load of 17.0 kN, was obtained for the final optimised mix (see **Table 5-8**). Very low Standard Deviations were obtained. A dog bone specimen (after testing) is shown in **Figure 5-5**. The stress-strain diagram for all three direct tensile strength tests is shown in **Figure 5-6** and it can be observed that all three test samples behaved in a similar manner. As obtained from literature, strain-softening behaviour is where fibres continue to transfer forces across the crack while avoiding brittle failure, which lead to gradual post-peak strength reduction, whereas strain-hardening behaviour is characterised by UHPFRC's ability to continue to increase in tensile capacity due to multiple cracking and beneficial fibre orientation. A steady drop in load carrying capacity was observed after the formation of the first crack. Strain softening behaviour was observed in two of the three test samples with the deformation localising in one major crack.

This may be attributed to the lower fibre content (< 2 %) used in the mixture design and fibre pull-out due to their short length.

Table 5-8: Direct tensile strength

	Critical load (kN)	Direct tensile strength (MPa)
Dog bone 1	17.8	7.26
Dog bone 2	16.5	6.68
Dog bone 3	16.7	6.81
Average	**17.0**	**6.92**
Standard Deviation	0.21	0.25

Figure 5-5: Dog bone specimen after test

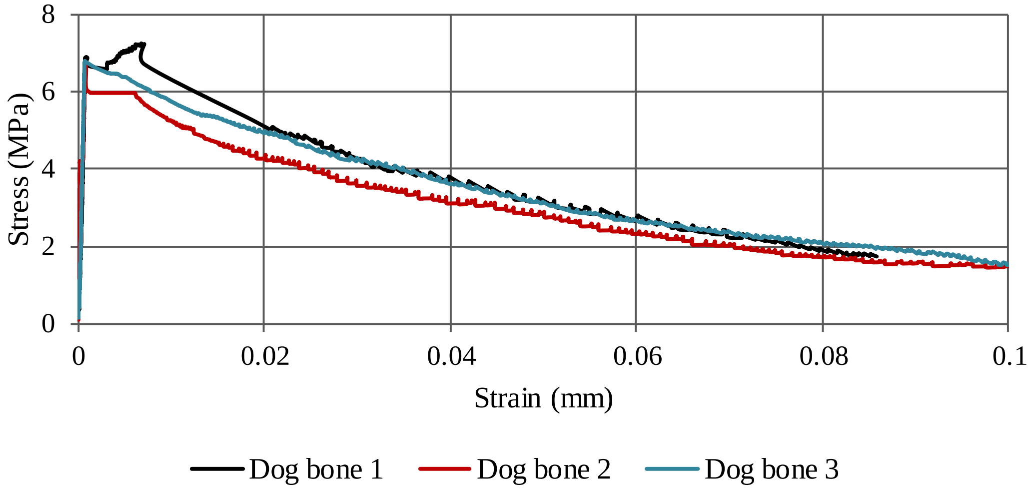

Figure 5-6: Stress-strain diagram for the direct tensile strength

5.7 SPLITTING TENSILE STRENGTH

The average splitting tensile strength (25 °C water bath curing) for the optimised mix was 17.5 MPa. The estimation for the splitting tensile strength as discussed in **Chapter 4.2** was 16.6 MPa. The difference between the actual splitting tensile strength and the estimated splitting tensile strength is 0.9 MPa, which is less than the SD obtained. The stress-deformation graph for the splitting tensile strength for the cylinder cured in a 25 °C water bath and in the 80 °C water bath is shown in **Figure 5-7** and **Figure 5-8** respectively. Two load peaks can be seen in all the results, with the first peak occurring with the initial/first crack and then a second peak forming as a result of the residual strength of the fibres. No significant difference can be observed in the initial cracking strength between the different curing conditions. The specimens cured under conventional curing conditions reached a higher secondary peak strength compared to the heat cured samples. However, the variability observed in the secondary peak strength for the heat cured specimens is lower compared to the conventional cured specimens.

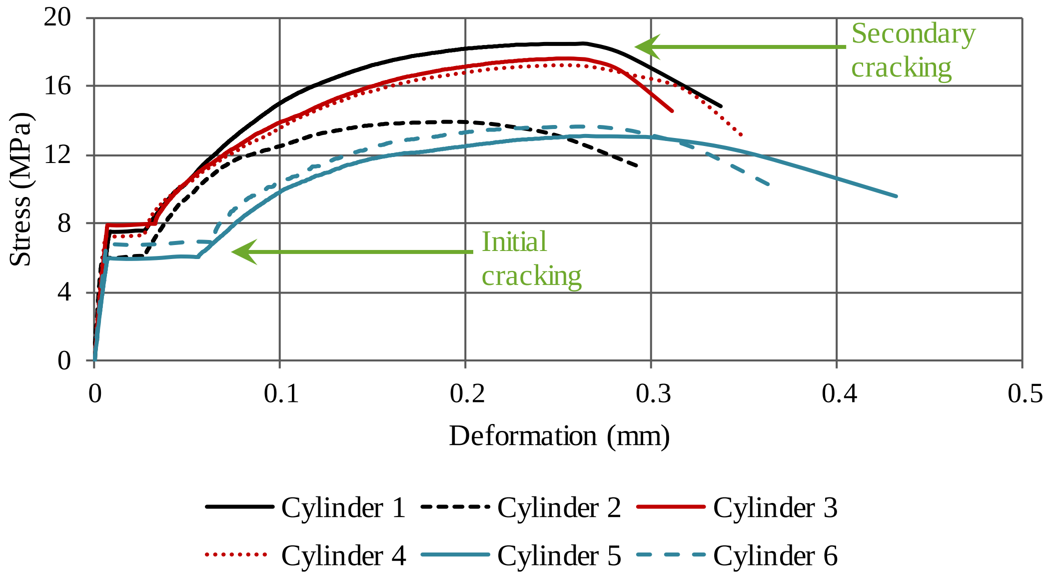

Figure 5-7: Splitting tensile strength - 25 °C water bath curing

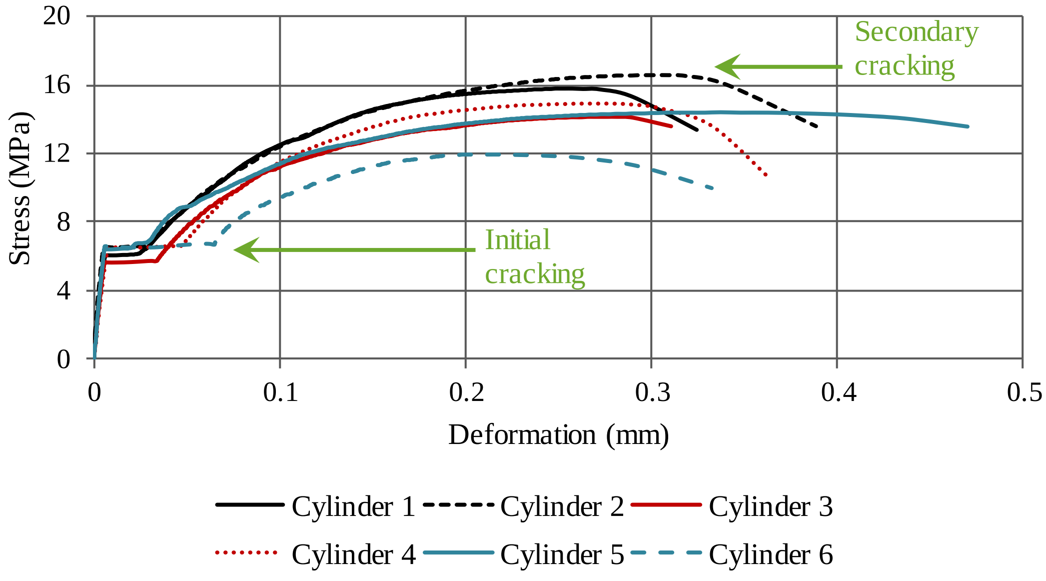

Figure 5-8: Splitting tensile strength - 80 °C water bath curing

The average splitting tensile strength results for the final optimised mix are illustrated in **Table 5-9**. The table shows both the twenty-eight-day initial cracking strength results and secondary peak strength results for the cylinders cured in the 25 °C water bath and the 80 °C water bath. The cylinders cured in the 80 °C water bath yielded a slightly lower initial cracking strength and secondary peak strength compared to the cylinders cured in the 25 °C water bath. The difference in the initial cracking strength and secondary peak strength between the different curing regimes was 0.7 MPa and 1.1 MPa respectively. The difference in initial cracking strength and secondary peak strength between the different curing conditions was deemed insignificant. The difference in the characteristic strengths calculated (for both initial cracking strength and secondary peak strength) between the different curing conditions was deemed insignificant. **Figure 5-9** shows a split cylinder after it had been tested until failure (reached peak load). No significant cracking was observed.

Table 5-9: Splitting tensile strength

	25 °C water bath curing		**80 °C water bath curing**	
	Initial cracking strength (MPa)	Secondary peak strength (MPa)	Initial cracking strength (MPa)	Secondary peak strength (MPa)
Cylinder 1	9.29	20.3	7.85	17.6
Cylinder 2	7.86	15.7	8.30	18.4
Cylinder 3	9.70	19.5	7.40	15.9
Cylinder 4	8.98	19.0	8.14	16.7
Cylinder 5	7.75	14.9	8.16	16.2
Cylinder 6	8.60	15.5	8.36	13.7
Average	**8.70**	**17.5**	**8.04**	**16.4**
Standard Deviation	0.71	2.15	0.33	1.46
Characteristic strength	7.53	13.94	7.50	14.01

Figure 5-9: Split cylinder after tested until failure

5.8 FLEXURAL TENSILE STRENGTH

The flexural tensile strength results obtained are tabulated in **Table 5-10** and the load-displacement curve is shown in **Figure 5-10**. The first crack load is the point where the initial linear elastic portion of the load-displacement curve ends (Limit of Proportionality - LOP). The peak load is the maximum point on the load-displacement curve (MOR). The assumption of a linear-elastic stress state to determine the flexural tensile strength was assumed even though the stress state in UHPFRC after cracking would be highly nonlinear. The flexural tensile strength value does not reflect the reality but allow a comparison between different types of UHPFRC. The other references did however not state whether a linear-elastic stress state was assumed."

Table 5-10: Flexural tensile strength

	Limit of Proportionality (LOP)		**Peak load (MOR)**	
	Load (kN)	LOP strength (MPa)	Load (kN)	Flexural tensile strength (MPa)
MOR beam 1	52.6	15.8	70.3	21.1
MOR beam 2	47.2	14.2	67.7	20.3
MOR beam 3	54.2	16.2	70.5	21.2
Average	**51.3**	**15.4**	**69.5**	**20.8**
Standard Deviation	2.98	0.90	1.30	0.39

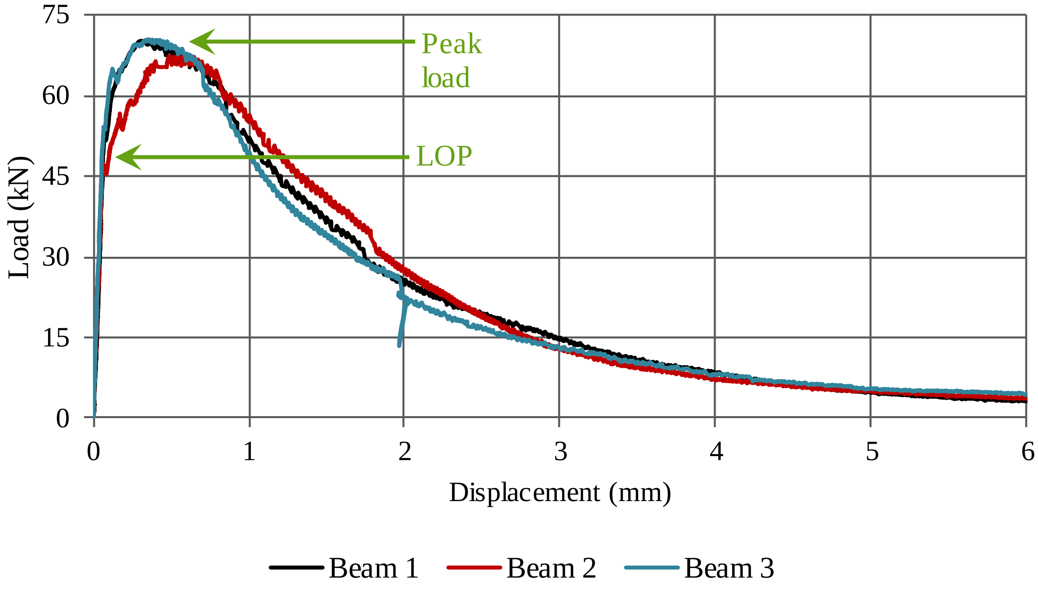

Figure 5-10: Load-displacement curve - 100 x 100 x 500 beams

All three test samples behaved in a similar manner. The strain hardening branch can be observed after the formation of the initial crack (LOP). All three beams experienced ductile failure with strain softening after the peak load. The figure shows that the short fibre efficiently bridges micro cracks. When the fibres could not restrain further growth of the cracks, the fibres pulled out. The load applied then decreased, which is reflected by the strain softening branch.

The flexural toughness was determined, as discussed in JSCE -SF4. The area under the load-displacement curve up to a deflection of span/150 (2 mm in this study) was calculated. The section of elasticity, strain hardening branch and strain softening branch were all considered in the calculation of the flexural toughness (see **Table 5-11**). The flexural toughness factor was determined using **Equation 4-5**. A MOR beam after failure is illustrated in **Figure 5-11**. One major crack was observed.

Table 5-11: Flexural toughness and flexural toughness factor

	Flexural toughness (Nm)	**Flexural toughness factor (N/mm^2)**
MOR beam 1	157	23.5
MOR beam 2	180	27.0
MOR beam 3	151	22.7
Average	**163**	**24.4**
Standard Deviation	12.4	1.87

Figure 5-11: MOR beam after tested until failure

5.8.1 Specimen size effect on flexural strength

Specimen size effect for bending strength was investigated by testing beams with five different depths in the same four-point bending set-up than what was used for the MOR beam tests. The LOP and flexural tensile strength results obtained for the various beams are tabulated in **Table 5-12** and **Table 5-13** respectively. The SD for both the LOP and peak load strength tends to increase as the specimen size decreases, indicating that the variation in strength is higher for smaller beam specimens. This is, however, not the case for the 100 x 45 x 500 mm MOR beam. This beam size experienced the lowest SD for both the LOP and the peak load strength.

The difference in load-displacement behaviour for the different beam depths is illustrated in **Figure 5-12** (The load-displacement behaviour for each beam depth is individually shown in **Appendix A**). It was observed that the smaller beam specimens showed higher ductility compared to that of the larger beam specimens. This is due to the improved fibre orientation in the smaller specimens. It was also noted that the crack opening size decreased as the beam's depth decreased. The flexural tensile strength obtained for the different beam specimens yielded similar results. The SD between the different beam specimens was 1.8 MPa.

Table 5-12: Specimens size effect on the flexural LOP

Thickness	Load (kN)*	Standard Deviation	LOP Strength (MPa)*	Standard Deviation
100	51.2	2.98	15.4	0.9
60	19.5	1.18	16.2	0.98
45	11.6	0.35	17.2	0.53
30	6.5	0.34	21.6	1.15
15	1.3	0.24	16.9	3.16

**(Average values)*

Table 5-13: Specimen size effect on the peak load strength (flexural tensile strength)

Thickness	Load (kN)*	Standard Deviation	Peak Strength (MPa)*	Standard Deviation
100	69.5	1.30	20.8	0.39
60	23.4	2.06	19.5	1.72
45	12.1	0.59	17.9	0.87
30	6.8	0.37	22.8	1.24
15	1.4	0.15	18.3	2.04

**(Average values)*

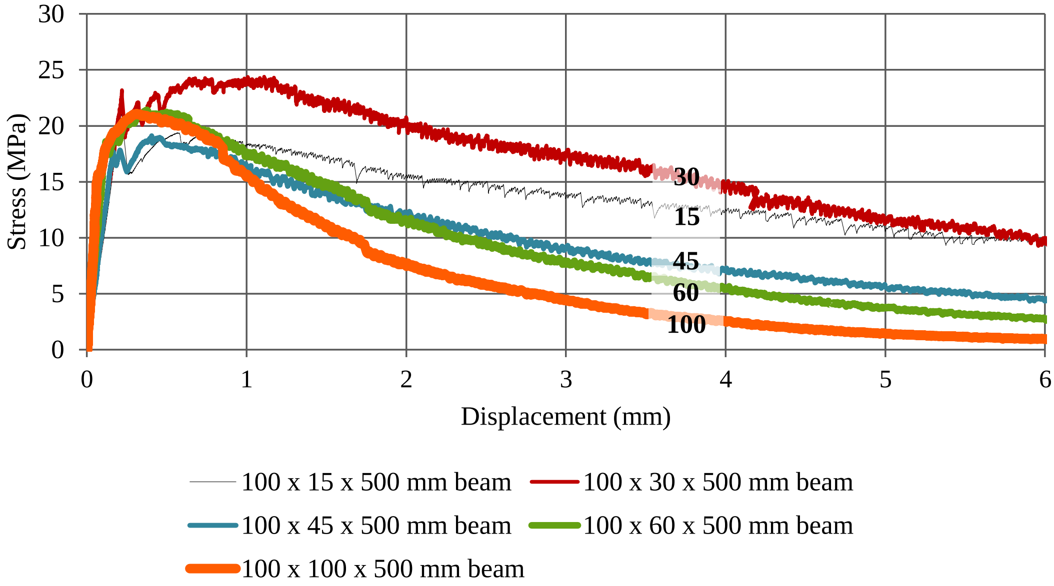

Figure 5-12: Specimen size effect on the flexural tensile strength

The LOP against beam depth is shown in **Figure 5-13**. It is clear from the graph that the beam depth of 30 mm yielded the highest flexural LOP. The LOP decreases with increasing depth (up to 100 mm). However, the beam depth of 15 mm yielded lower LOP results compared to the beam depth of 30 mm. The 30 mm beam yields a maximum value when considering the LOP.

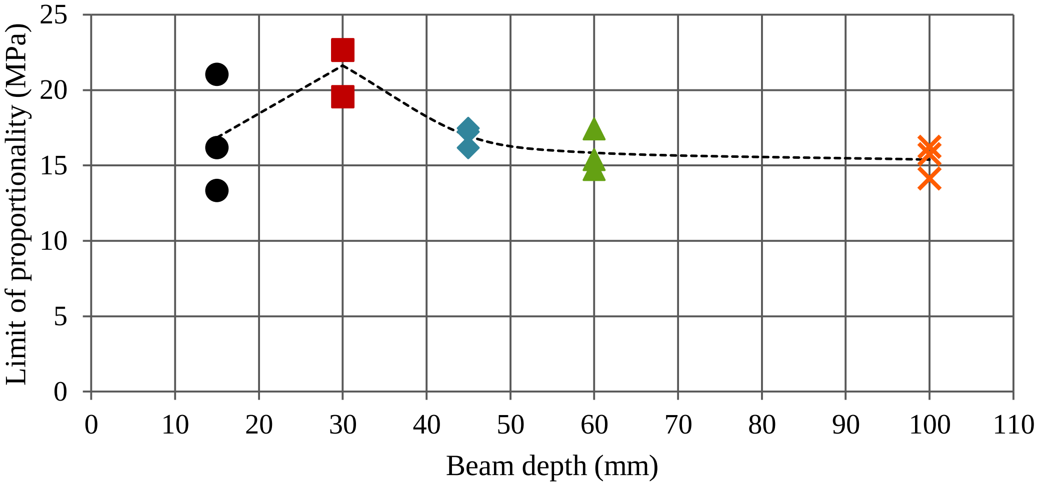

Figure 5-13: LOP vs. beam depth

Figure 5-14 illustrates the flexural tensile strength (peak load) over beam depth. The same trend is observed as in **Figure 5-13.** It can be said that the beam with the 30 mm depth has an optimal depth for an element spanning 300 mm. Further testing is required to determine whether a span-to-depth ratio of 10 would yield optimum (maximum) flexural tensile strength. The results obtained from Denneman (2011), as discussed in **Chapter 2.8.5.2,** also yielded a maximum flexural tensile strength for beam specimens with a span-to-depth ratio of 10.

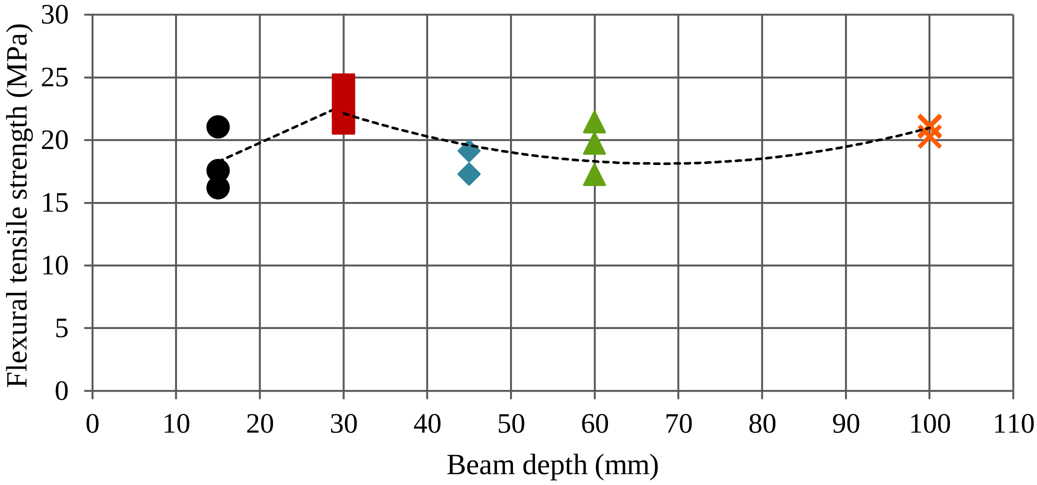

Figure 5-14: Flexural tensile strength vs. beam depth

The flexural toughness and flexural toughness factor were determined as per JSCE -SF4:1984 and are tabulated in **Table 5-14**. The area under the load-displacement curve up to a deflection of span/150 (2 mm in this study) was calculated to determine the flexural toughness (see **Figure 5-15)**. The section of elasticity, strain hardening branch and strain softening branch were all considered in the calculation of the flexural toughness. The flexural toughness factor was determined using **Equation 4-7**. It should be noted that the SD decreased with decreasing depth for both the flexural toughness and the flexural toughness factor. Thus, a lower variability is experienced in the beams with limited depth.

Table 5-14: Specimen size effect on the flexural toughness and flexural toughness factor

Thickness	Flexural toughness (Nm) *	Standard Deviation	Flexural toughness factor (N/mm^2) *	Standard Deviation
100	163	33.2	30.6	4.99
60	60.5	17.6	9.10	2.64
45	28.5	4.80	4.28	0.72
30	14.8	5.51	2.22	0.83
15	2.96	0.89	0.44	0.13

**(Average values)*

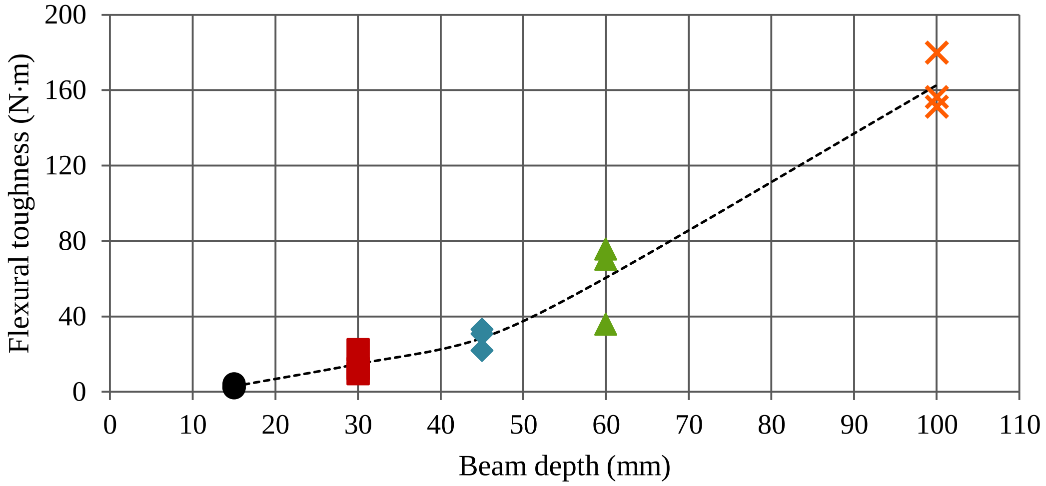

Figure 5-15: Flexural toughness vs. beam depth

During a flexural tensile strength test, the measured deflection of the UHPC specimens experience both deflection due to moment (δ_M) and due to shear (δ_V). However, both the deflection due to moment and shearing deflection must be considered if the span-to-depth ratio of the specimen is large. **Equation 2-5** was used to determine the shear contribution for each beam depth (see **Table 5-15**). According to Elsaigh (2007), shear stresses would contribute significantly to the total deflection of the beam with a span-to-depth ratio in a range of 3 to 4.

This is confirmed in **Figure 5-16**. The beams with limited depth would have a lower shear contribution.

Table 5-15: Shear contribution

	Dimensions (b x h x L - mm)	Span-to-depth ratio (L_{span}/h)	Shear contribution $(h/L_{span})^2$
Type 1	100 x 100 x 500	3.0	0.111
Type 2	100 x 60 x 500	5.0	0.040
Type 3	100 x 45 x 500	6.7	0.023
Type 4	100 x 30 x 500	10	0.010
Type 5	100 x 15 x 500	20	0.003

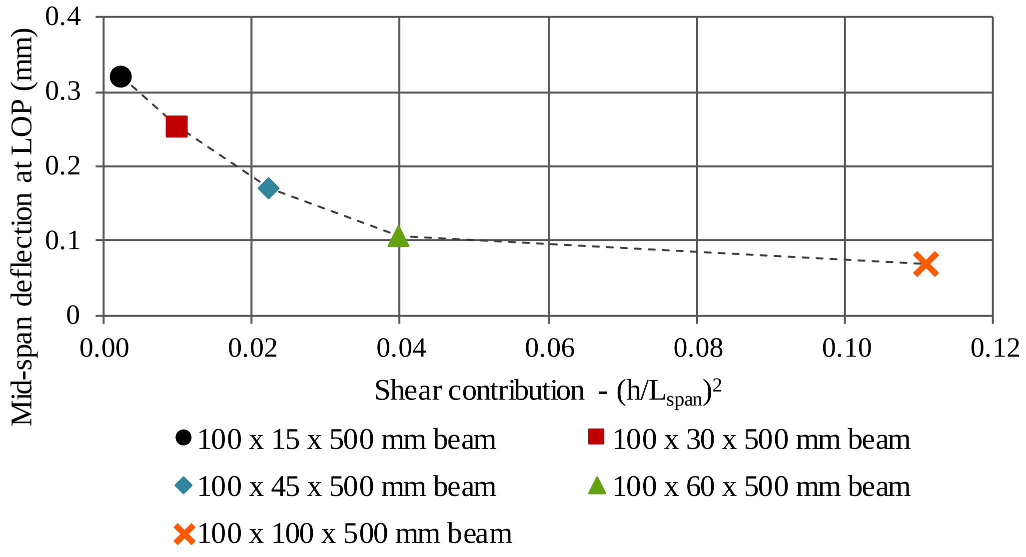

Figure 5-16: Shear contribution

5.9 VOLUME CHANGE

The results obtained from the three concrete cylinders for drying shrinkage and creep are illustrated in **Figure 5-17**. Three important aspects of time-dependant behaviour are illustrated, namely, elastic strain, shrinkage strain and basic creep strain. The total strain experienced is when these three act simultaneously together. The short-term elastic strain experienced due to the applied load is almost 50 micro-strain. By using the experimentally obtained modulus of elasticity together with the stress applied to the creep specimens, the predicted maximum elastic stain value could be calculated. This value was calculated within 2 % of the experimentally obtained value. The predicted maximum elastic strain value was successfully calculated and the difference between the calculated value and the experimentally obtained value was deemed insignificant. The long-term shrinkage strain and creep strain experienced in the concrete is less than 30 micro-strain and 160 micro-strain respectively (up to ninety days). The drying shrinkage results correspond well with results obtained from Yoo et al. (2018), who reported drying shrinkage for UHPC of 45 micro-strain. Drying shrinkage can be neglected, but autogenous shrinkage should be studied if this type of concrete is cast in situ or restrained during setting. Vatannia (2018) measured higher creep values (560 micro-strain) than those obtained in this study. A higher stress level was however applied to the specimens compared to the stress level of approximately 15 % of the concrete cylinder strength capacity used in this study. It can be seen from the results obtained that drying shrinkage and creep are interdependent. Basic creep of the specimens under load but not drying, i.e. no moisture movement from or to the surrounding environment, is illustrated in **Figure 5-18**. Both specimens behaved in a similar manner. The basic creep strain per MPa experienced in the concrete was less than 8 micro-strain per MPa for both samples. It can thus be concluded that insignificant creep occurred at the stress level of approximately 15 % of the concrete cylinder strength capacity used in this study.

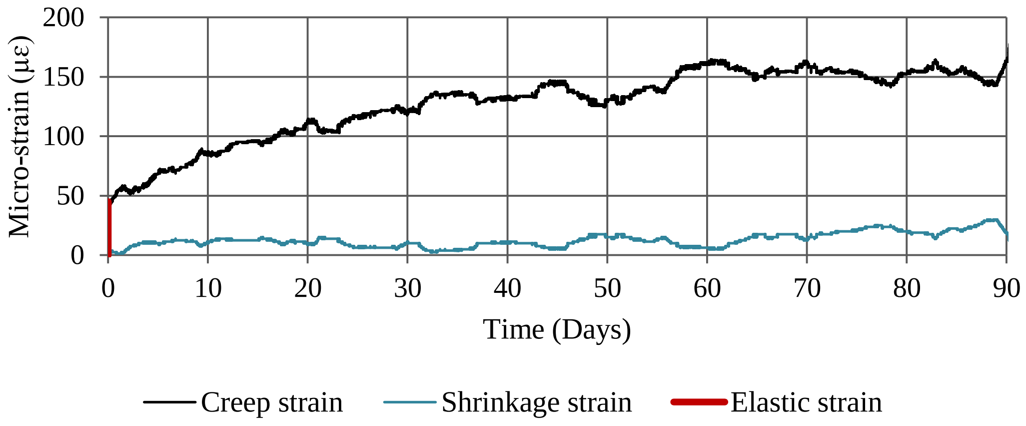

Figure 5-17: Creep strain, shrinkage strain and elastic strain

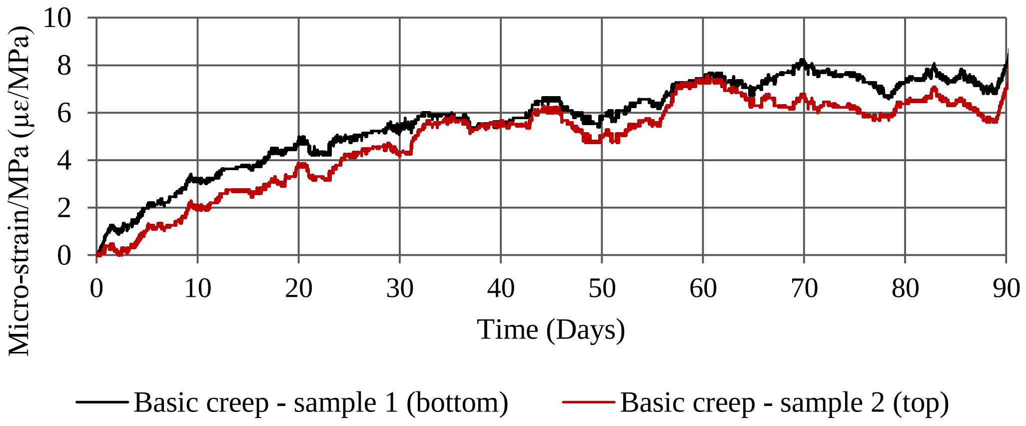

Figure 5-18: Basic creep

5.10 MICROSTRUCTURAL ANALYSIS

Microstructure studies were also conducted on the conventional cured and heat cured UHPFRC cubes using a SEM. **Figure 5-19** illustrates the SEM images for conventional cured and heat cured samples taken from outside and inside (centre) of a 100 mm cube after tested until failure (fifty-six days). Both the conventional and heat cured sample show a dense microstructure. However, there is a difference in the appearance of the microstructure when comparing the two different curing regimes. A rougher appearance can be seen in the heat cured samples compared to that of the conventional cured samples. Both the samples taken from the outside of the cubes show more cracks, whereas the samples taken from the centre of the cubes are more compact with very little to no cracks. No DEF was observed in the samples.

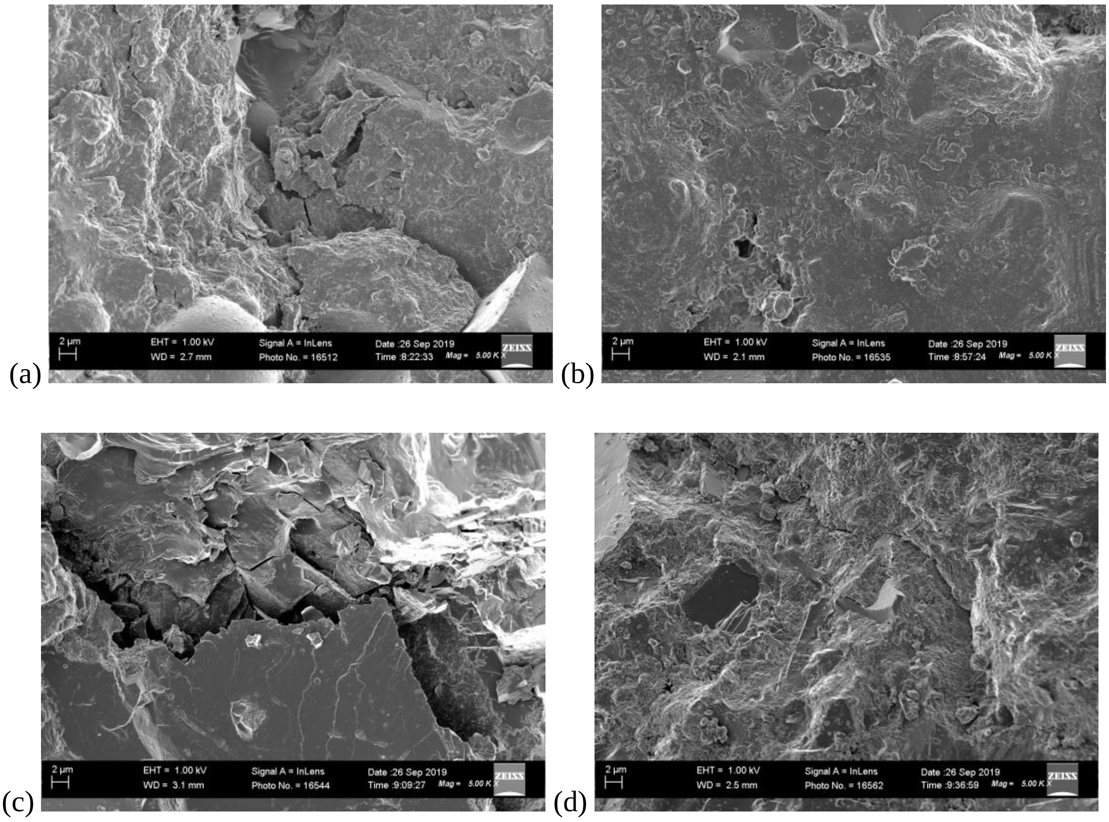

Figure 5-19: SEM images for (a) conventional cured sample (outside), (b) conventional cured sample (centre), (c) heat cured sample (outside), and (d) heat cured sample (centre) (magnification = 5 000 and Scale = 2 µm)

Figure 5-20 illustrates the SEM images showing unhydrated FA particles in the various samples (note that the magnification as well as the scale differ for the images). Both curing regimes still have unhydrated FA particles for samples taken from outside and from the centre of the samples. Thus, the curing regime did not influence the hydration of the FA. **Figure 5-21** illustrates the SEM images of the conventional cured sample taken from the centre of the sample. A close-up image of unhydrated silica fume agglomeration is illustrated in **Figure**

5-21 (a). This image proves that, even after mixing, silica fume agglomerates do not break up and, therefore, the PSD as shown in **Figure 3-1** is an accurate representation of the particle size of a silica fume agglomerate. Needle-like structures can also be seen in **Figure 5-21 (b)**.

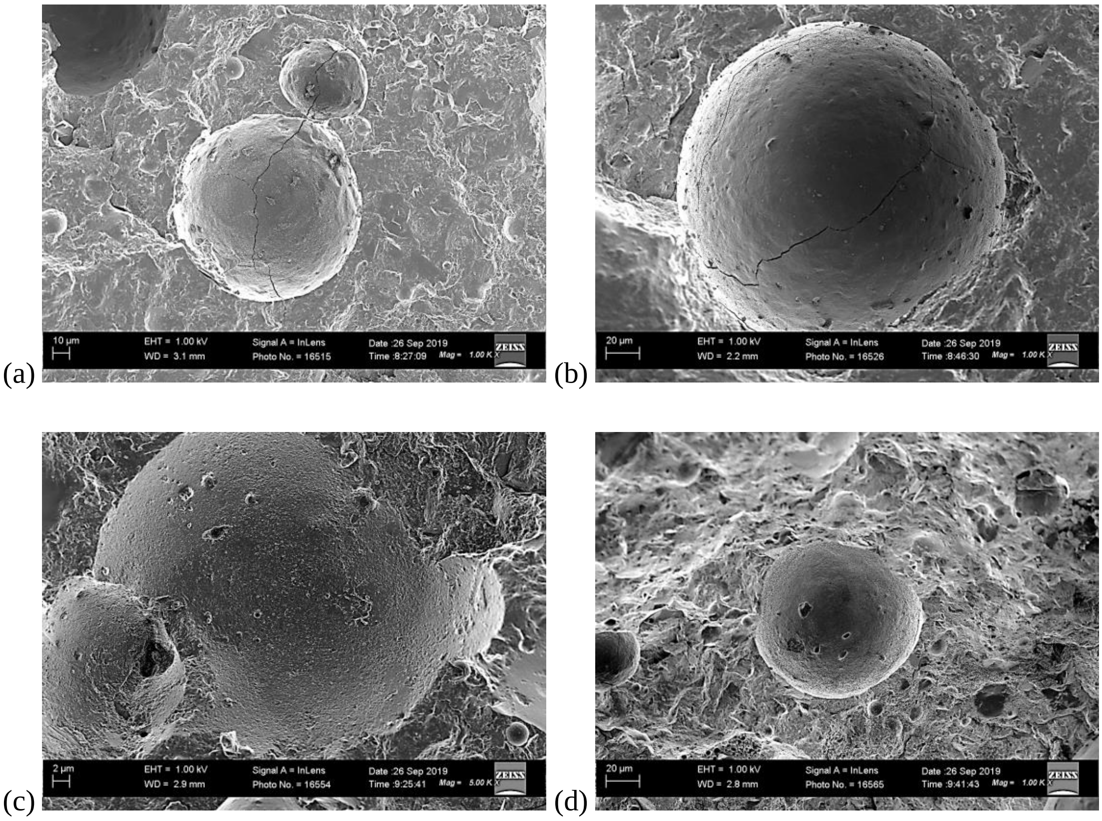

Figure 5-20: SEM images showing a FA particle in (a) conventional cured sample (outside) (magnification = 1 000 and Scale = 10 µm), (b) conventional cured sample (inside) (magnification = 1 000 and Scale = 20 µm), (c) heat cured sample (outside) (magnification = 5 000 and Scale = 2 µm) and (d) heat cured sample (inside) (magnification = 1 000 and Scale = 20 µm)

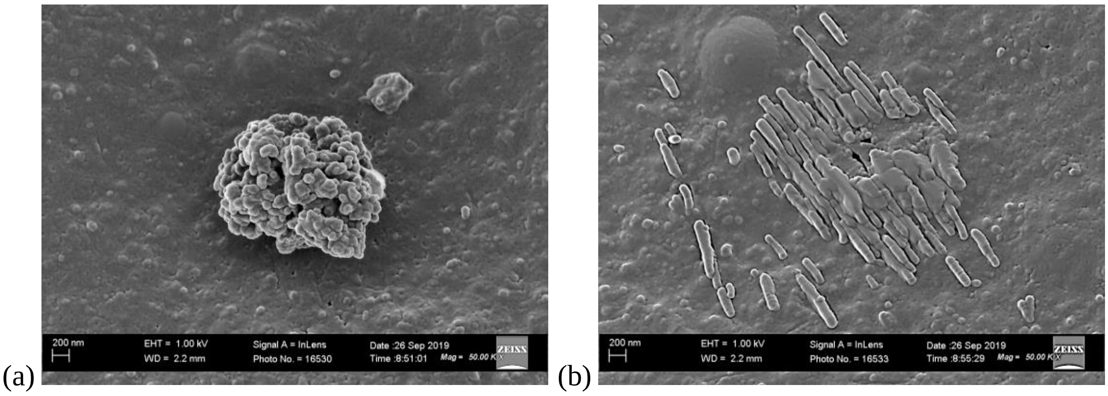

Figure 5-21: SEM images for conventional cured sample (centre) showing (a) close-up image of an unhydrated silica fume agglomeration and (b) needle-like structures (magnification = 50 000 and scale = 200 nm)

Figure 5-22 illustrates the SEM images of the heat cured sample taken from the centre of the sample. A close-up image of needle-like structures is illustrated in **Figure 5-22 (a)**. **Figure 5-22 (b)** illustrates a close-up image of the rough concrete matrix.

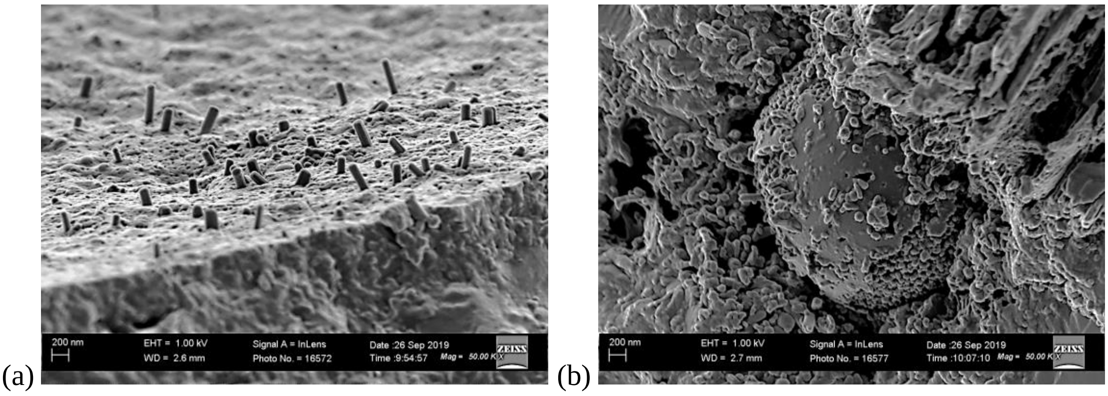

Figure 5-22: SEM images for heat cured sample (centre) showing (a) needle-like structures and (b) close-up image of the concrete matrix (magnification = 50 000 and scale = 200 nm)

5.11 EXPERIMENTAL RESULTS FOR SMALL PRECAST BEAMS

The experimental results obtained from the testing of the precast beams are discussed in this section. Two 2000 × 50 × 100 mm beams and two 2000 × 100 × 50 mm beams were cast from the final optimised mix design and tested to determine their flexural behaviour and ultimate load capacity. No additional reinforcing was cast into the beams and the beams did not include any shear reinforcement. The four beams were cured in a water bath (25 °C) until the day of testing. The weight of each experimental precast beam was determined before it was placed in a 25 °C water bath and then again on the day of testing (see **Table 5-16**). The weight gained due to water absorption was then determined. A beam gained an average weight of 0.13 kg over the twenty-eight-day water curing period. This was regarded as insignificant. This can be attributed to the very dense microstructure of the UHPFRC matrix.

Table 5-16: Weight gained after water curing (kg)

	Weight before water curing	**Weight on testing day**	**Weight gained**
Beam 1	23.68	23.72	0.04
Beam 2	22.66	22.82	0.16
Beam 3	22.50	22.66	0.16
Beam 4	23.38	23.54	0.16
Average	**23.06**	**23.19**	**0.13**
Standard Deviation	0.49	0.45	0.05

The test was conducted by using a four-point bending test with a span length of 1.8 m. The maximum load values as well as the flexural tensile strength results obtained for the small experimental precast beams are tabulated in **Table 5-17** and the load-displacement graph is shown in **Figure 5-23**.

Table 5-17: Small experimental precast beams

	Peak load (kN)	**Flexural tensile strength (MPa)**
Beam 1 (50 x 100 x 2000 mm)	3.91	14.06
Beam 2 (50 x 100 x 2000 mm)	3.54	12.76
Average	**3.72**	**13.41**
Standard Deviation	0.18	0.65
Beam 3 (100 x 50 x 2000 mm)	1.77	12.72
Beam 4 (100 x 50 x 2000 mm)	2.02	14.55
Average	**1.89**	**13.64**
Standard Deviation	0.13	0.91

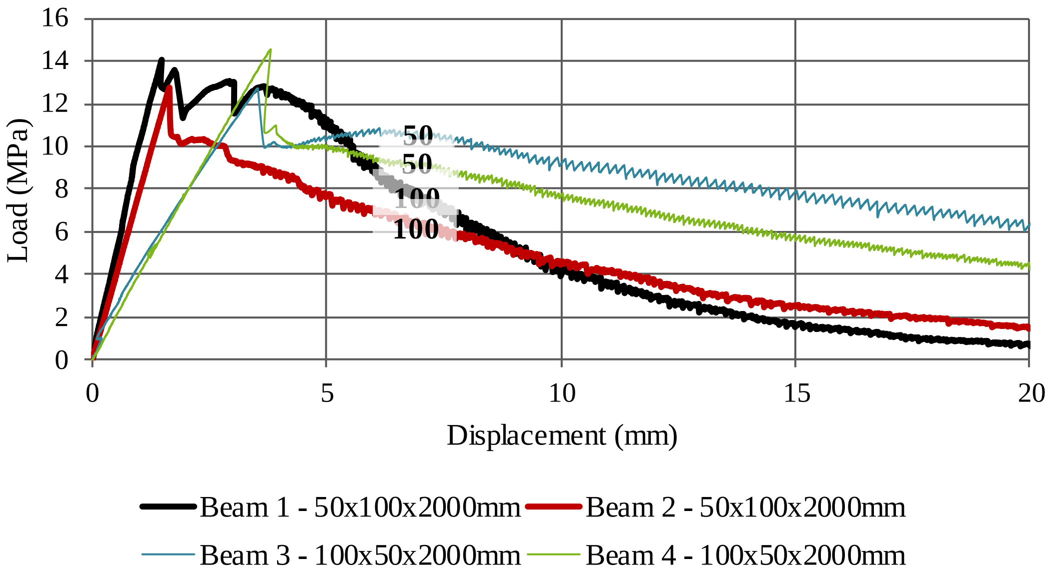

Figure 5-23: Load-displacement curve

All test samples failed due to flexural failure. No shear failure was observed in any of the beams tested. At the start of loading, a linear behaviour in the load-displacement graph was noticeable for all beam specimens. After the first crack, strain softening behaviour was observed in all four test samples and one major crack opening formed. Due to the improved fibre orientation in the smaller specimens, as seen in **Chapter 5.8.1**, the beams with limited depth showed higher ductility**.** This was also observed with the 100 x 50 x 2000 mm beam specimens that showed higher ductility compared to that of the 50 x 100 x 2000 mm beam specimens. This indicates that beam specimens with a lower second moment of area show higher ductility after cracking.

It was also reported that the crack size decreased with the 100 x 50 x 2000 mm beam specimens compared to the 50 x 100 x 2000 mm beam specimens. Even though the 50 x 100 x 2000 mm beam specimens can carry a higher peak load, flexural tensile strength and deflection at peak load obtained for the 100 x 50 x 2000 mm beam specimens was higher.

5.12 COMPARISON TO NORMAL STRENGTH CONCRETE

The experimental UHPFRC precast beams were compared to an equivalent 30 MPa concrete beam (unreinforced) that was designed to withstand the same failure load as measured for the UHPFRC beams. A 30 MPa concrete mix design was developed, as tabulated in **Table 5-18**. All the specimens were then left to cure in the 25 °C water bath until testing day. The specimens cast, number of specimens cast and the day of testing are tabulated in **Table 5-19**. The material properties obtained from the 30 MPa concrete mix is compared to the final optimised UHPFRC mix in **Table 5-20.** The estimated density obtained from the surface plot was 2491 kg/m^3 (theoretical density = 2626.6 kg/m^3) The air content for the final optimised mix were 5.5 % which will cause a reduction in the expected density. The theoretical density for the 30 MPa mix was calculated to be 2542 kg/m^3. Therefor the densities were expected to be similar. The beam dimensions, self-weight and cost per MPa for the normal 30 MPa beam, so as to carry the same load as the experimental UHPFRC beams, were determined and these results were compared.

Table 5-18: Mix composition for 30 MPa concrete (kg/m^3)

Material	kg/m^3	Relative Density
Cement	287	3.14
Water	215	1.00
Dolomite sand	1110	2.91
Dolomite aggregate/stone	930	2.85

Table 5-19: Specimens cast for 30 MPa concrete mix

Parameter	Specimens cast	Amount	Testing days
Compressive strength	100 mm cubes	5	28
E-value	Cylinders	3	28
Splitting tensile strength	-	-	28

Table 5-20: Comparison of material properties

	UHPFRC beam	30 MPa concrete beam
Cube compressive strength (MPa)	152.6	30.31
E-value (GPa)	54.18	30.38
Splitting tensile strength (MPa)	17.47	2.23
Density (kg/m^3)	2481	2473

Embodied Energy (EE) and Embodied Carbon (EC) is defined by Soutsos & Domone (2018) as follows:

- EE: "*The amount of energy required to mine, collect, crush, refine, extract, synthesise and process the materials into the form that we can use.*"
- EC: "*The amount of carbon dioxide emitted during the above processes but taking into account the source of energy and its impact on the environment.*"

EE and EC relate to a material's production. Typical values for EE and EC are given in **Table 5-21** (Hammond & Jones, 2008; Mishra et al., 2018; Zheng, 2009). There are no published South African values for EE and EC and thus typical values as given in **Table 5-21** were used to determine the EE/unit strength and EC/ unit strength of the UHPFRC and 30 MPa concrete mixtures. The EE and EC per unit strength comparison between the UHPFRC mixture and 30 MPa concrete mixture is given in **Table 5-22**. The EE/unit compressive strength for the UHPFRC is 3.7 % higher than the 30 MPa concrete. Whereas the EC/unit compressive strength for the UHPFRC is 37.7 % lower than the 30 MPa concrete. The EE/unit splitting tensile strength for the UHPFRC is 48.6 % lower than the 30 MPa concrete. Whereas the EC/unit splitting tensile strength for the 30 MPa concrete is more than double that of the UHPFRC.

Table 5-21: EE and EC contents of materials used

	EE (MJ/kg)	EC (kg CO_2/kg)
Portland Cement	4.6	0.83
USF	0.1	0.08
FA	0.1	0.08
Water	0.02	-
Aggregate	0.11	0.005
Superplasticiser	11.5	0.6
Steel fibres	36.0	2.83

Table 5-22: EE/unit strength and EC/unit strength

	UHPFRC	30 MPa concrete
EE/unit compressive strength (MJ/m^3/MPa)	54.9	52.9
EC/unit compressive strength (kg CO_2/m^3/MPa)	6.01	8.28
EE/unit splitting tensile strength (MJ/m^3/MPa)	479	712
EC/unit splitting tensile strength (kg CO_2/m^3/MPa)	52.5	111

The dimension required for the 30 MPa beam to carry the failure load of the experimental precast UHPFRC beams was determined by using the splitting tensile strength obtained for the 30 MPa concrete together with **Equation 4-6**. A width:depth relationship of 1:2 was used and the length was kept constant (2 m). The volume cast, self-weight, cost per beam and cost per MPa were then calculated (see **Table 5-23**). Even though the cost per kg for the precast UHPFRC beam is ten times more than the 30 MPa concrete beam, the self-weight and cost per MPa for the precast UHPFRC beam is much lower compared to the 30 MPa concrete beam, making the precast UHPFRC beam much more cost-effective with reduced self-weight of the structure. Furthermore, the utilisation of by-products, such as USF and FA, as cement replacement materials makes UHPFRC more sustainable.

Table 5-23: Comparison of beam dimension, self-weight, cost/beam and cost/m^3

	UHPFRC beam	30 MPa concrete beam
Dimension (mm)	50 x 100 x 2000	90 x 180 x 2000
Volume (m^3)	1.0 x 10^{-2}	3.2 x 10^{-2}
Theoretical self-weight (kg)	24.81	80.13
Cost per beam (Rand)	83.17	26.95
Cost per kg (Rand/kg)	3.35	0.33
Cost per MPa (Rand/MPa)	6.20	11.64

5.13 SUMMARY

The estimated material properties for the final optimised mix, obtained from the various surface plots as discussed in **Chapter 3.7**, were compared to the actual experimental values obtained and are tabulated in **Table 5-24**. The results (ARD (%)) show that RSM (CCD) can effectively be used to predict the material behaviour of any combination of fibre and superplasticiser content.

Table 5-24: Estimated material properties obtained from surface plots vs actual experimental material properties

Parameter	Estimated	Actual	ARD (%)
Flow (mm)	310.4	310.0	0.13
Density (kg/m^3)	2491	2481	0.40
Air content (%)	5.75	5.5	4.55
Seven-day compressive strength (MPa)	114.4	110.6	3.44
Twenty-eight-day compressive strength (MPa)	156.0	152.6	2.23
Modulus of elasticity (GPa)	52.70	54.18	2.73
Splitting tensile strength (MPa)	16.60	17.47	4.98

The material properties obtained for the final optimised mix is summarised in **Table 5-25**. The concrete can be considered as UHPFRC as the twenty-eight-day compressive strength is greater than 150 MPa. The state of stress for the splitting tensile strength cylinders is biaxial and this results in the value for the splitting tensile strength being higher than the direct tensile strength (uniaxial tensile strength). Simple beam-bending theory and linear elastic stress-strain behaviour until failure is assumed when determining the maximum flexural tensile stress (MOR). However, concrete is a non-linear material and the assumption of linear stress distribution is not valid after cracking. The stress calculated for the flexural tensile strength is higher than the actual value developed in the concrete but allow a comparison between different types of UHPFRC. Therefore, the MOR is also greater than the direct tensile strength. Limited long-term drying shrinkage and creep was observed for the UHPFRC.

Table 5-25: Summary of material properties

Parameter	Average
Twenty-eight-day compressive strength (MPa)	152.6
E-value (GPa)	54.18
Direct tensile strength (MPa)	6.92
Splitting tensile strength (MPa)	17.47
Flexural tensile strength (MPa)	20.84
Shrinkage strain (με)	30
Creep strain (με)	160

The difference in density and air content between the different curing conditions was deemed insignificant. The strength development for concrete specimens is higher when cured in the conventional 25 °C water bath than for concrete cured in the 80 °C water bath. A maximum cube strength was reached after seven days for the heat cured specimens. Specimens cured in the 25 °C water bath showed a gradual increase in strength up to ninety days. The estimated strength development of concrete does not incorporate the detrimental effect of high curing temperatures on long-term strength and therefore overestimate the long-term strengths. The strength estimates for both early and long-term ages can be improved by considering this effect in the strength development functions. It can be concluded that there is no significant difference in the twenty-eight-day modulus of elasticity for the conventional cured specimens and the heat cured specimens. No significant difference was observed in the initial cracking strength (obtained from the splitting tensile strength test) between the different curing conditions. The secondary peak strength (splitting tensile strength) for the conventional cured specimens was higher than the heat cured specimens. From the results, it can be concluded that heat curing is not recommended when considering the long-term strength development. The microstructural analysis of the concrete specimens showed no DEF. Unhydrated FA particles were observed in the microstructural analysis. Silica fume agglomerates were also observed, confirming that superplasticiser and mixing does not break up the agglomerated silica fume.

It was found that the specimen size has a significant effect on the measured cube compressive strength. An 11% increase in cube compressive strength after twenty-eight days was observed for specimen sizes of 50 mm compared to those of 100 mm. Smaller beam specimens showed higher ductility compared to those of the larger beam specimens. The crack opening size decreased as the beam’s depth decreased. A lower variability was experienced in the beams with limited depth. It can be concluded that the beam with the 30 mm depth has a depth resulting in the highest LOP for an element spanning 300 mm. Further testing is required to determine whether a span-to-depth ratio of 10 would yield maximum results. Shear stresses contribute significantly to the total deflection of the beam with a span-to-depth ratio in a range of 3 to 4. The beams with limited depth yield a lower shear contribution.

The small precast experimental beams failed due to flexure. No shear failure was observed in any of the beams tested. After the first crack, strain softening behaviour was observed in all four test samples and one major crack opening formed. The specimens with a lower second moment of area showed higher ductility after cracking and decreased crack size.

The self-weight and cost per MPa for the precast UHPFRC beam is lower compared to the equivalent 30 MPa concrete beam, making the precast UHPFRC beam more cost-effective. Furthermore, the utilisation of by-products, such as USF and FA, as cement replacement materials makes UHPFRC more sustainable, leading to a reduced life-cycle cost. The calculated EE/unit strength and EC/unit strength values for the UHPFRC mixture yield lower values compared to that of the 30 MPa concrete mixture, indicating that the UHPFRC can be used to reduce the environmental footprint of the concrete industry.

6 NUMERICALLY PREDICTED BEHAVIOUR OF UHPFRC BEAMS

6.1 INTRODUCTION

Researchers often use inverse analysis (back-calculation) techniques for establishing the tensile stress-strain relationship for concrete (Elsaigh, 2007). In this study a generalised analytical method proposed by Elsaigh (2007) was used to obtain the equivalent stress-strain relationship of UHPFRC. Inverse analysis was used to determine the stress-strain relationship of concrete based on experimental load-deflection or moment-curvature results. A simplified stress-strain response was used to match theoretical moment curvature and load-displacement relationships with the corresponding experimental responses. The theoretical moment curvature relationship was converted to a theoretical load-displacement relationship and compared to that of the experimentally obtained results.

6.2 ANALYSIS METHOD

The moment-curvature or load-displacement relationships was derived by assuming a simplified stress-strain response for the UHPFRC. An iterative trial and error procedure were followed, where the stress-strain response was adjusted until either the analytical moment-curvature or load-displacement results matched the experimentally obtained values. The inverse analysis uses the following major steps (Küsel, 2018) and is shown schematically in **Figure 6-1**:

1. Assume a stress-strain response for the concrete.
2. Calculate the moment-curvature relationship based on the assumed stress-strain response.
3. Convert the calculated moment-curvature relationship into a load-displacement response.
4. Adjust the stress-strain response and repeat steps (2) and (3) until the calculated moment-curvature or load-displacement behaviour agree with the experimental results (within acceptable limits).

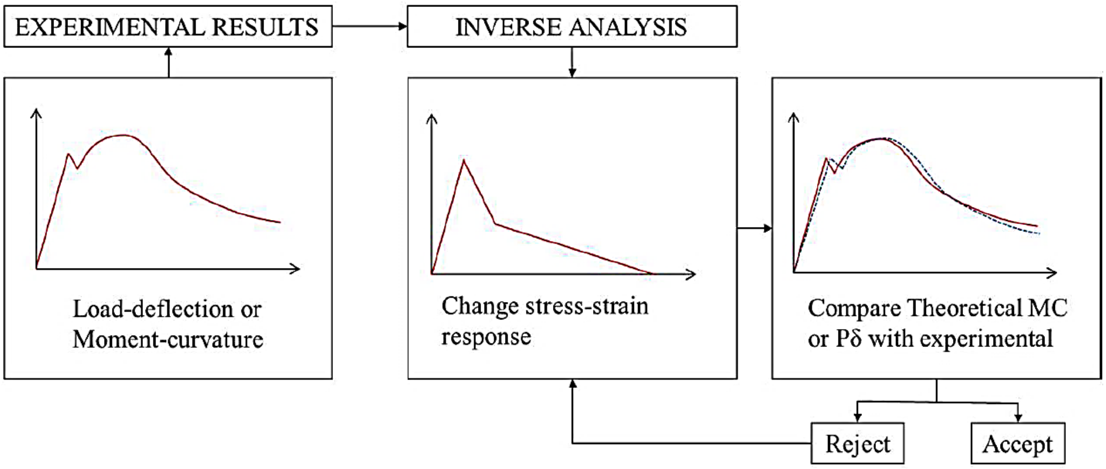

Figure 6-1: Inverse analysis procedure (Küsel, 2018)

6.3 PROPOSED STRESS-STRAIN RELATIONSHIP

According to Küsel (2018), the accuracy to which a theoretical moment-curvature or load-displacement relationship can be matched to the experimentally obtained response depends on the number of parameters in the stress-strain response. The proposed stress-strain response used in the inverse analysis procedure is illustrated in **Figure 6-2**. The parameters shown in this figure are described as follows (Küsel, 2018):

- Compression behaviour:
    - σ_{cu} and ε_{co} represent the maximum linear elastic stress and corresponding elastic strain respectively.
    - ε_{cu} represent the ultimate compressive strain.
- Tension behaviour:
    - σ_{to} and ε_{to} represent the cracking strength and corresponding elastic strain respectively.
    - σ_{t1} and ε_{t1} represent the residual stress and residual strain which denotes a change in slope of the tensile softening curve.
    - ε_{tu} represents the ultimate tensile strain.

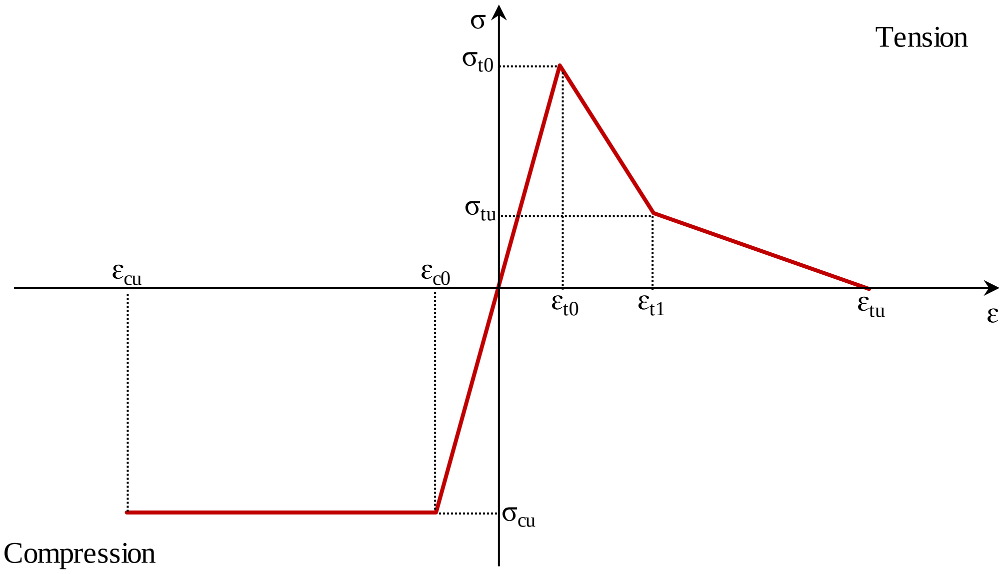

Figure 6-2: Proposed simplified stress-strain response (adapted from Elsaigh, 2007)

The stress-strain relationship is expressed in **Equation 6-1**.

$$\sigma(\varepsilon) = \begin{cases} \sigma_{cu}, & for\ (\varepsilon_{cu} \leq \varepsilon < \varepsilon_{co}) \\ E\varepsilon, & for\ (\varepsilon_{co} \leq \varepsilon < \varepsilon_{to}) \\ \sigma_{to} + \psi(\varepsilon - \varepsilon_{to}), & for\ (\varepsilon_{to} \leq \varepsilon < \varepsilon_{t1}) \\ \sigma_{tu} + \lambda(\varepsilon - \varepsilon_{t1}), & for\ (\varepsilon_{t1} \leq \varepsilon < \varepsilon_{tu}) \end{cases}$$

Equation 6-1

Where E, ψ and λ represent the slopes of the lines:

$$E = \frac{\sigma_{cu}}{\varepsilon_{co}}$$

Equation 6-2

$$\psi = \frac{\sigma_{tu} - \sigma_{to}}{\varepsilon_{t1} - \varepsilon_{to}}$$

Equation 6-3

$$\lambda = \frac{-\sigma_{tu}}{\varepsilon_{tu} - \varepsilon_{t1}}$$

Equation 6-4

The material property tests performed in **Chapter 5** provided the preliminary points for the assumed stress-strain response values. This reduced the number of variables required to obtain a representative stress-strain response. The remaining variables were obtained through an iterative trial and error procedure until the tensile behaviour provided theoretical moment-curvature or load-displacement responses comparable to the responses obtained from the experimental results. Since the proposed stress-strain relationship greatly simplifies the actual stress-strain response, some parameters, such as the cracking stress may not be accurately represented on the moment-curvature or load-displacement curves (Küsel, 2018).

6.4 MOMENT CURVATURE CALCULATIONS

The following three assumptions was used to perform the iterative procedure to obtain the moment-curvature relationship as described by Elsaigh (2007):

1. The stress-strain relationship of the material is known.
2. Plane sections remain plane during bending.
3. Equilibrium exists between the externally applied loads and the internal stresses.

The stress-strain relationship proposed in **Equation 6-1** was used together with the assumed initial values obtained from the material property tests. This forms part of the first assumption. The second assumption implies a linear strain distribution across the depth of the cross-section so that the relationship between strains and the neutral axis can be expressed as in **Equation 6-5** and illustrated in **Figure 6-3**.

$$\varepsilon(y) = \frac{y}{x}\varepsilon_{top} = \left(\frac{y}{h - x}\right)\varepsilon_{bot}$$ **Equation 6-5**

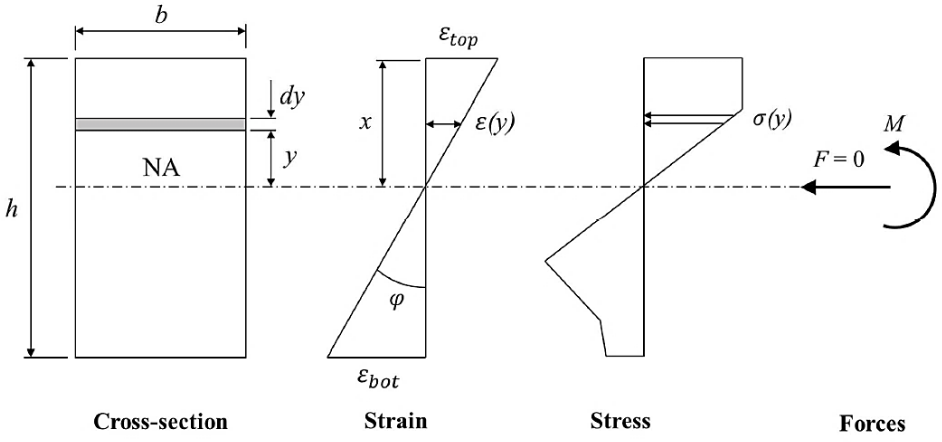

Figure 6-3: Strain and stress distribution at a section (Küsel, 2018)

The final assumption is used to relate the internal forces and moments to the internal stresses and strains. The internal forces are equal to zero and the internal moment is equal to the applied moment. The force and moment equilibrium are described as follows:

$$F = \int_{-(h-x)}^{x} \sigma(\varepsilon) b \, dy = \frac{xb}{\varepsilon_{top}} \int_{\varepsilon_{bot}}^{\varepsilon_{top}} \sigma(\varepsilon) \, d\varepsilon = 0$$ **Equation 6-6**

$$M = \int_{-(h-x)}^{x} \sigma(\varepsilon) y b \, dy = \frac{-x^2 b}{{\varepsilon_{top}}^2} \int_{\varepsilon_{bot}}^{\varepsilon_{top}} \sigma(\varepsilon) \, \varepsilon \, d\varepsilon = 0$$ **Equation 6-7**

The top and bottom strains are required to describe the strain distribution of a section at any applied load. One can select a value for either the top or bottom strain and calculate the other unknown strain using **Equation 6-5** together with **Equation 6-6**. The selected and calculated strains correspond to a certain external applied load. The moment can then be calculated using **Equation 6-7**. The curvature of the section can be calculated by using **Equation 6-8**. Curvature is described as the gradient of the strain distribution profile.

$$\varphi = \frac{\varepsilon_{top}}{x} = \frac{\varepsilon_{bot}}{(h-x)} \qquad \textbf{Equation 6-8}$$

The procedure followed to obtain the analytical moment-curvature response is summarised as follows:

1. A value is selected for the bottom strain (ε_{bot}).
2. The top strain (ε_{top}) is solved using **Equation 6-6**. This step is an iterative trial and error procedure in which the top strain is varied until force equilibrium is achieved ($F = 0$).
3. Moment and curvature are determined using **Equation 6-7** and **Equation 6-8** respectively.
4. A new bottom strain value is selected and steps (2) and (3) is repeated until sufficient points have been obtained to describe the complete moment-curvature response.

The procedure outlined above is based on the initial proposed stress-strain relationship. This relationship is then altered and the procedure to calculate the moment-curvature relationship is repeated until the theoretical moment-curvature relationship corresponds with the experimental moment-curvature response.

6.5 STRESS-STRAIN RELATIONSHIP ESTIMATION GUIDELINE

An initial guess is required when determining the simplified stress-strain response for concrete. The following general guideline can be used for the first estimate (Elsaigh, 2007):

1. σ_{cu} and ε_{cu} can be approximated as cube compressive strength and 0.0035 respectively.
2. σ_{to} can be estimated as 10 % the compressive strength.
3. Assume modulus of elasticity is valid for tension and determine ε_{to}.
4. σ_{tu} can be approximated as 42 % of σ_{to}.
5. The values for ε_{t1} and ε_{tu} can be approximated as (ε_{to} + 0.001) and 0.1 respectively.

Küsel (2018), recommend the following steps for calculating the stress-strain response:

1. Establish the compressive stress-strain behaviour from the compressive strength results obtained.
2. Assume modulus of elasticity is valid for tension, change σ_{to} to fit the peak moment and peak load.
3. To match the position of the inflection point, change σ_{t1} and ε_{t1}.
4. To match the curve following the inflection point, change ε_{tu}.
5. Make final correction to match the peak moment and peak load by re-adjusting σ_{to}.
6. Minor adjustments can be made to any parameter to reach an agreeable fit.

6.6 PARAMETRIC STUDY

A parametric study was performed by changing parameters on the stress-strain curve and then calculating the moment-curvature response. The material properties were used as a guideline, specific parameters were changed, one at a time, and the resulting change in the moment-curvature shape was then observed. The aim of the parameter study was to determine how the stress-strain parameters must be changed in order to reach the required moment-curvature relationship. The influence of the stress-strain parameters as shown in **Figure 6-4** was investigated.

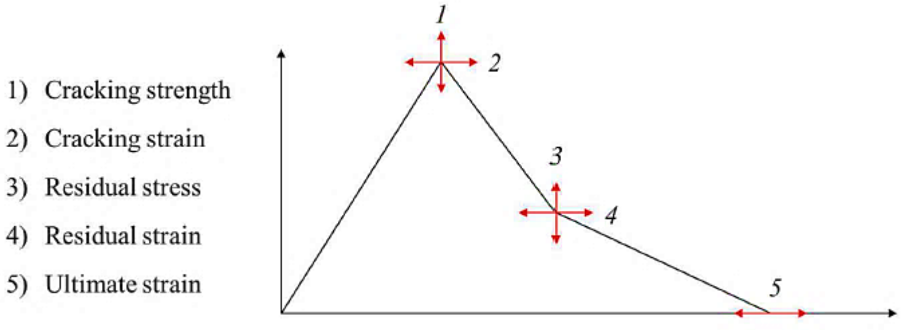

Figure 6-4: Stress-strain parameters (Küsel, 2018)

6.6.1 Effect of changing the cracking strength

Figure 6-5 illustrates the changes in cracking strength and the resulting stress-strain response. Three modulus of elasticity values were investigated namely, 45.0 GPa, 54.2 GPa and 60.0 GPa. Theses modulus of elasticity values are commonly encountered in UHPC and cover the range of modulus of elasticity values obtained from material tests. The cracking strength values were based on the modulus of elasticity values. **Figure 6-6** show the resulting moment-curvature relationship when changing the cracking strength. The peak moment increased with increased cracking strength. An increase in cracking strength of 20 % (from 8.0 MPa to 9.6 MPa) leads to an increase of approximately 19 % in the peak moment.

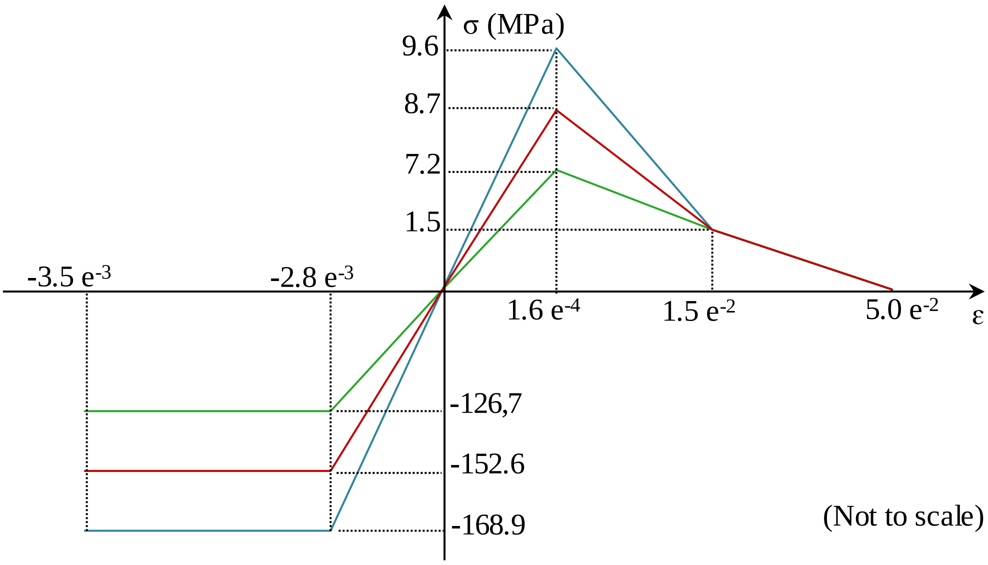

Figure 6-5: Stress-strain curve with changing cracking strength

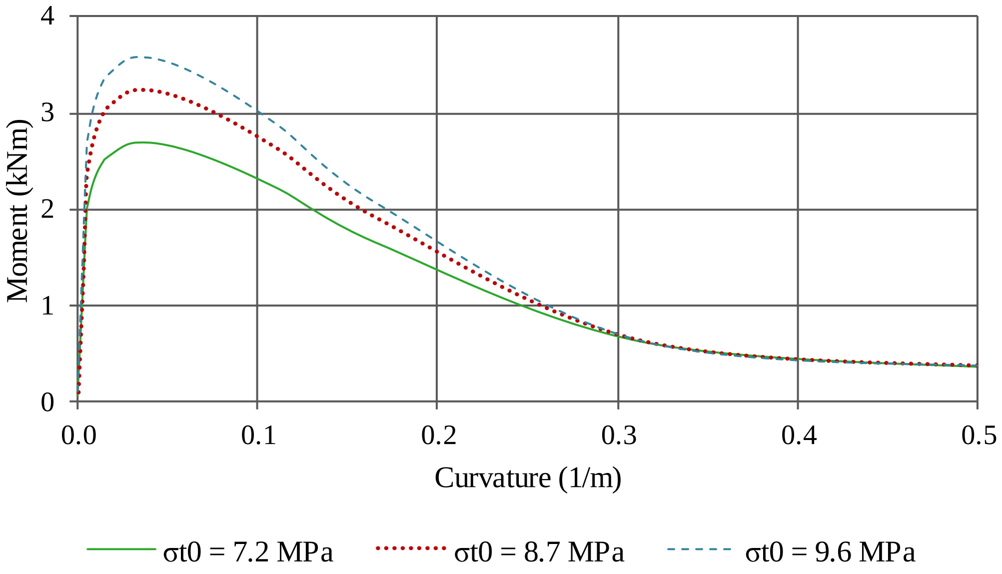

Figure 6-6: Moment-curvature response for a changing cracking strength

6.6.2 Effect of changing the cracking strain

Figure 6-7 illustrates the stress-strain response when the cracking strain is changed. The cracking strength was kept constant as 8.7 MPa. The same three modulus of elasticity values of 45.0 GPa, 54.2 GPa and 60.0 GPa were investigated. The cracking strain values were based on the modulus of elasticity values. **Figure 6-8** show the resulting moment-curvature relationship when changing the cracking strain. No significant influence of changing the cracking strain on the peak moments is observed. Reducing the cracking strain results in an increased modulus of elasticity, and vice versa. The change in cracking strain has very little effect on the overall moment-curvature relationship.

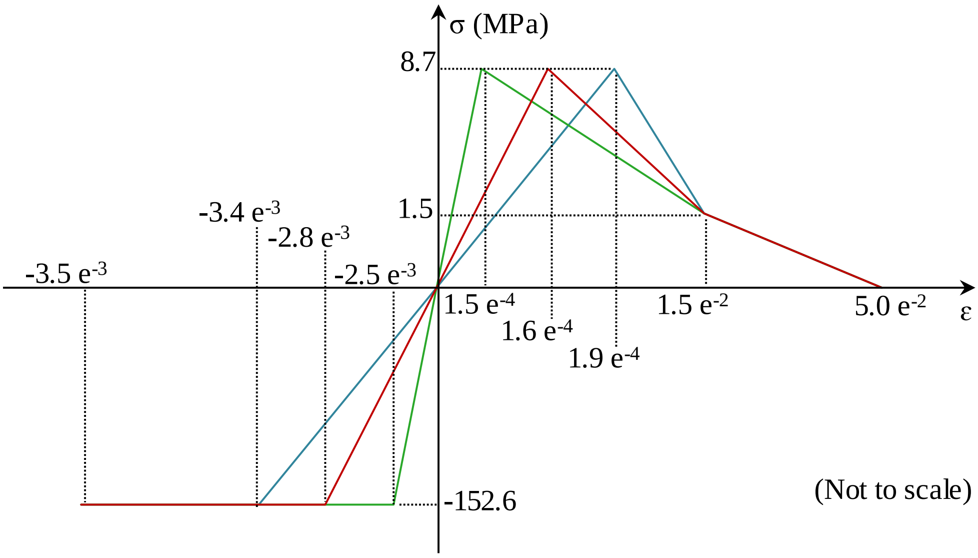

Figure 6-7: Stress-strain curve with changing cracking strain

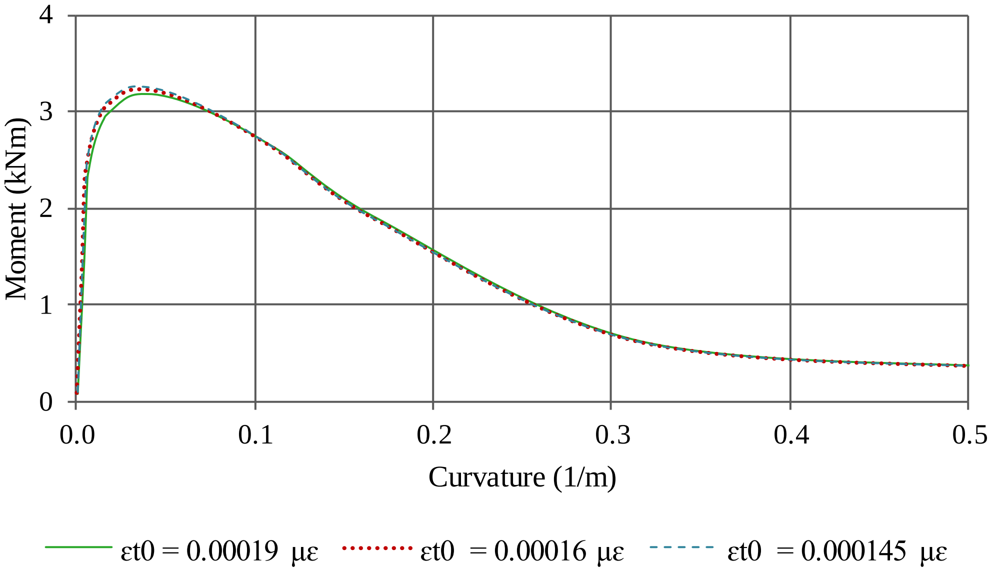

Figure 6-8: Moment-curvature response for a changing cracking strain

6.6.3 Effect of changing the residual stress

Figure 6-9 shows the three chosen residual stresses while all other parameters were kept constant. **Figure 6-10** illustrates the resulting moment-curvature relationship when changing the residual stress. The change in residual stress influence the latter part of the moment-curvature curve. A small change in residual stress led to a significant change in the moment-curvature relationship after the peak loads. The peak moments increased by approximately 1.34 % and 1.36 % as the residual stress increased from 0.5 MPa to 1.5 MPa and 1.5 MPa to 2.5 MPa respectively. The position of the peak moments shifted by approximately 0.16 % and 0.11 % in terms of curvature as the residual stresses increased from 0.5 MPa to 1.5 MPa and 1.5 MPa to 2.5 MPa respectively.

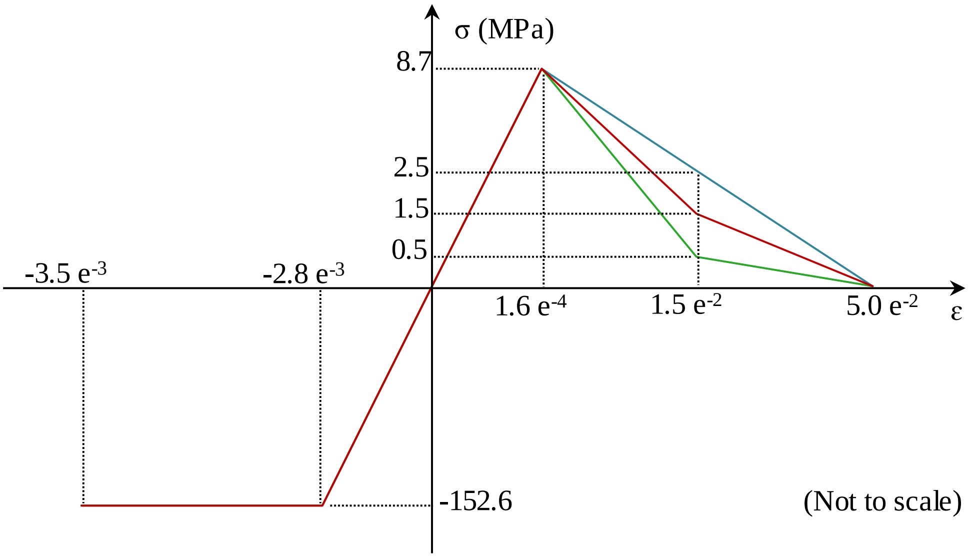

Figure 6-9: Stress-strain curve with changing residual stress

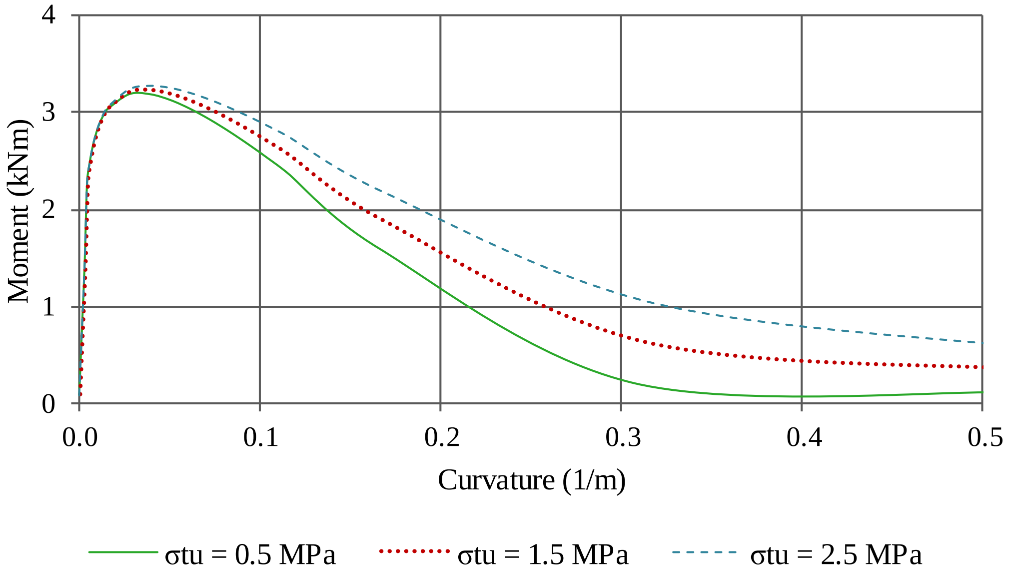

Figure 6-10: Moment-curvature response for a changing residual stress

6.6.4 Effect of changing the residual strain

Figure 6-11 shows the three chosen residual strains and the resulting stress-strain response. All other parameters were kept constant. **Figure 6-12** illustrates the resulting moment-curvature relationship when changing the residual strain. Changing the residual strain result in a slight effect on the peak moment, as well as shifting the position of the peak moment.

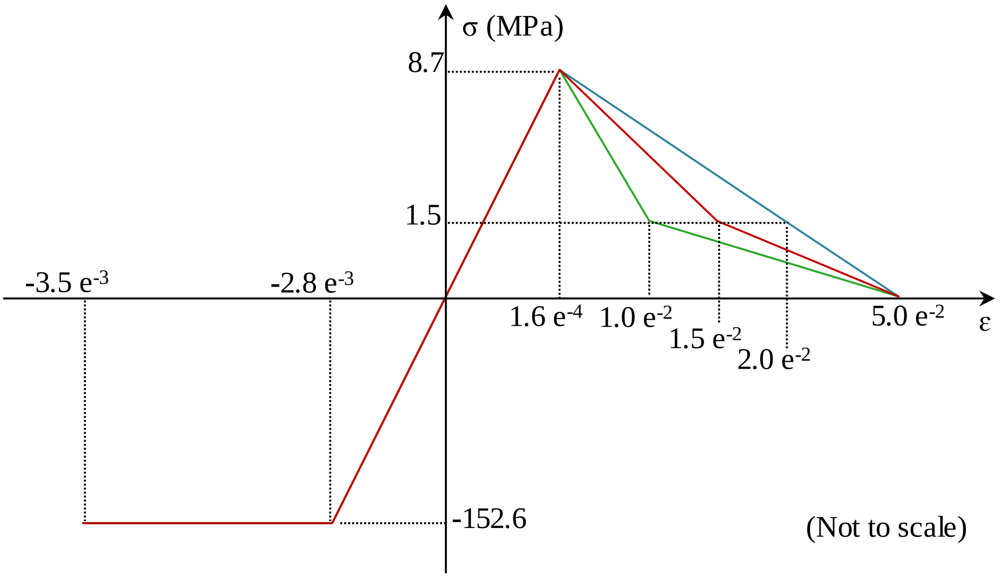

Figure 6-11: Stress-strain curve with changing residual strains

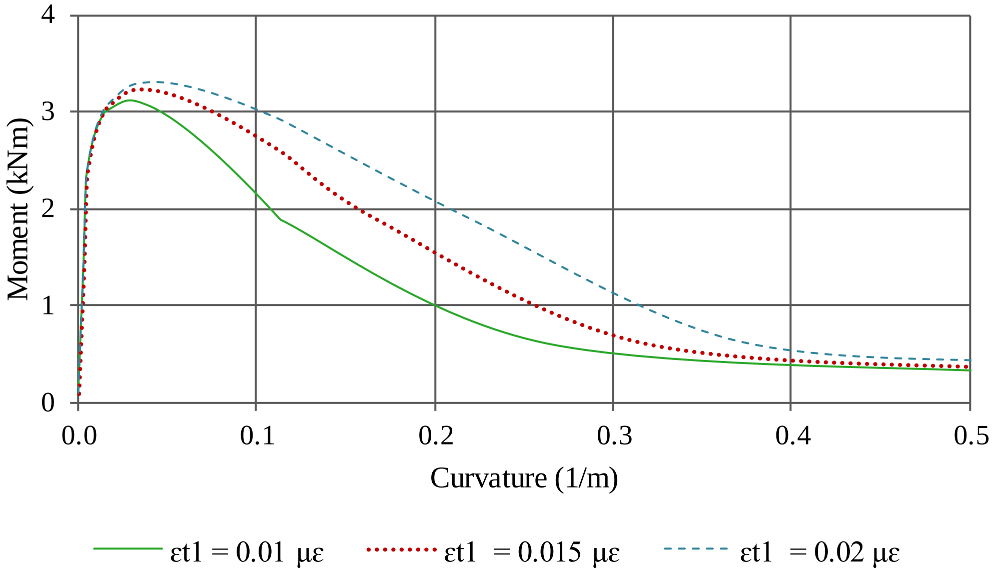

Figure 6-12: Moment-curvature response for a changing residual strain

6.6.5 Effect of changing the ultimate strain

Figure 6-13 shows the three chosen ultimate strains while all other parameters were kept constant. The objective of changing the ultimate strain is to change the response of the tail end of the moment-curvature relationship. **Figure 6-14** illustrates the resulting moment-curvature relationship when changing the ultimate strain. The slope of the tail end of the curve is changed when changing the ultimate strain. The ultimate strain lift or lower the moment-curvature response after the residual stress has been reached. The change in ultimate strain did not influence the peak moment or its position.

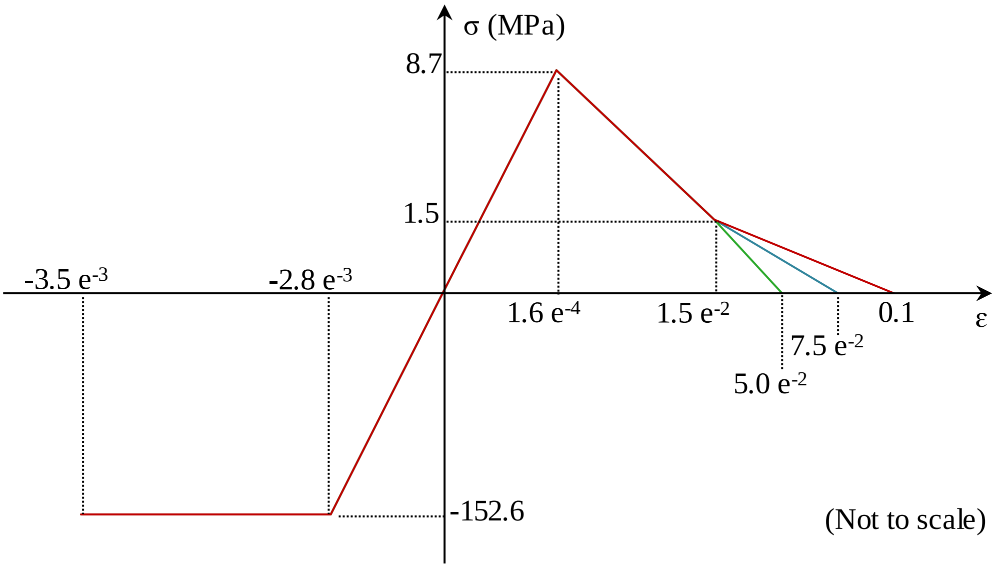

Figure 6-13: Stress-strain curve with changing ultimate strains

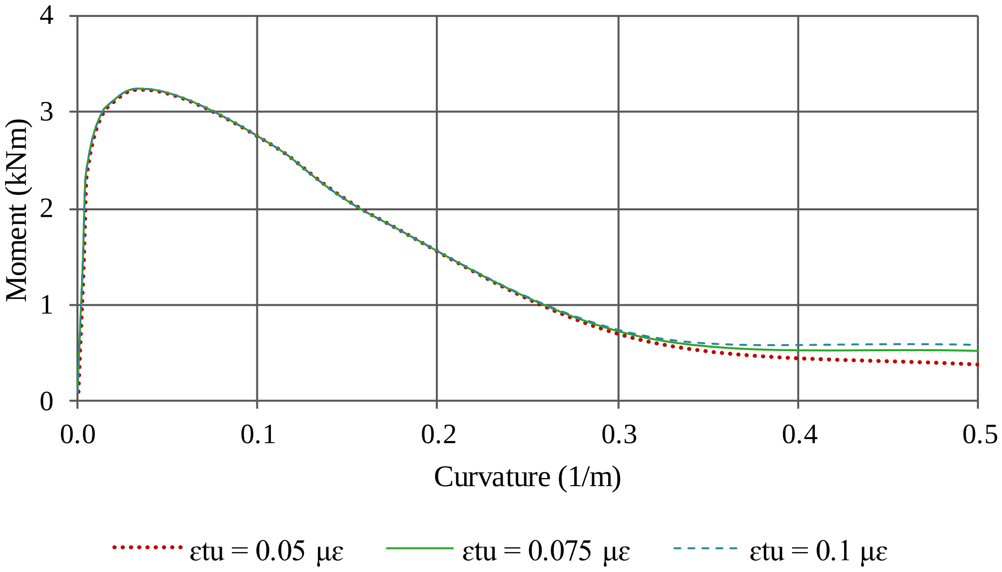

Figure 6-14: Moment-curvature response for a changing ultimate strain

6.7 IMPLEMENTING THE INVERSE ANALYSIS

The inverse analysis method was used to calculate the simplified stress-strain response of the UHPFRC. The experimentally obtained load-displacement results for the 100 x 100 x 500 mm beams (see **Chapter 5.8**) were converted to moment-curvature. The moment-curvature and load-displacement results were then used to calibrate the stress-strain response. The theoretical results are compared to the experimental results and can be seen in **Figure 6-15**. The stress-strain response used to obtain the final theoretical relationship is illustrated in **Figure 6-16**. The calculated moment-curvature and load-displacement relationships show a good correlation to the experimental results. The peak tensile stress was however adjusted accordingly to match the theoretical peak moments to the experimentally obtained results.

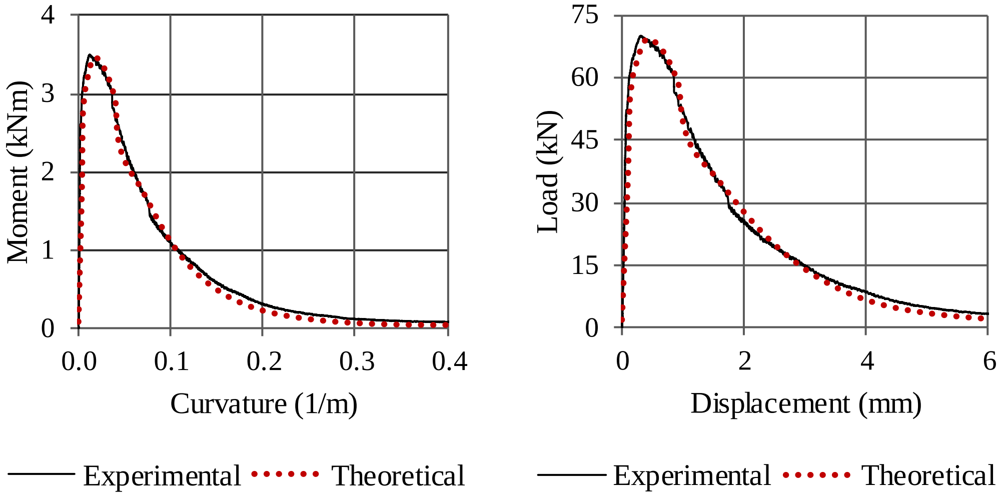

Figure 6-15: Experimental and theoretical moment-curvature and load displacement responses

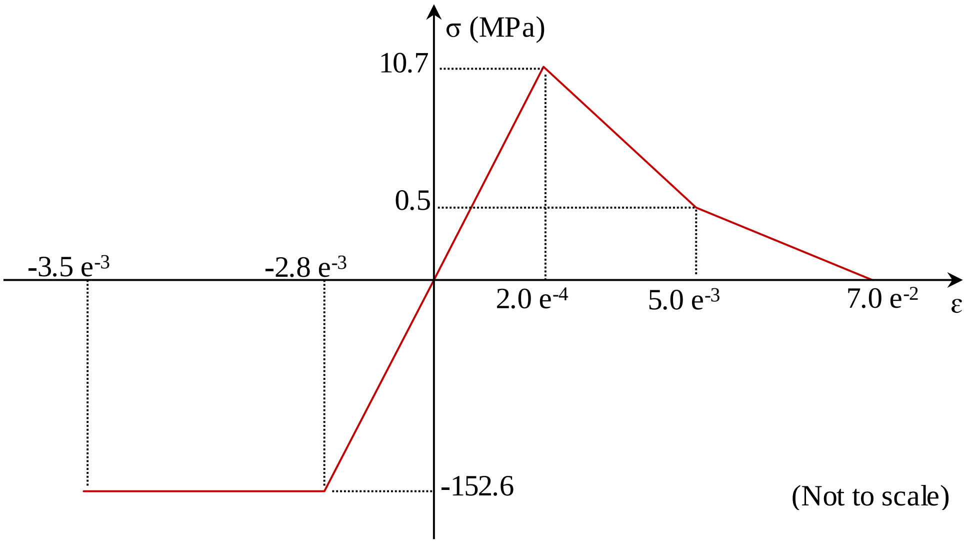

Figure 6-16: Resulting stress-strain response

6.8 IMPROVED ESTIMATION

In **Chapter 6.7**, the peak tensile stress was adjusted accordingly to match the theoretical peak moments to the experimentally obtained results. The strain at this peak stress was therefore not the true cracking strain. This is the results of simplifying the stress-strain response. According to Elsaigh (2007), if only the overall load-displacement behaviour is required, the smeared crack approach is the best choice. Therefore, by reducing the stiffness of the concrete after initial cracking, two additional points on the stress-stain response were added to more accurately reflect the cracking stress and the residual stress. The improved stress-strain response is illustrated in **Figure 6-17**. The moment-curvature and load-displacement curve comparisons is shown in **Figure 6-18**.

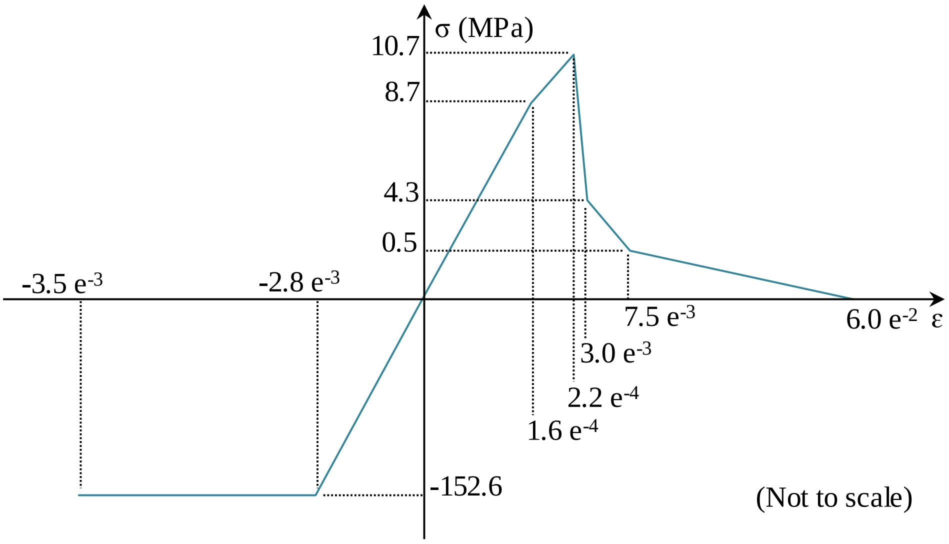

Figure 6-17: Improved stress-strain response

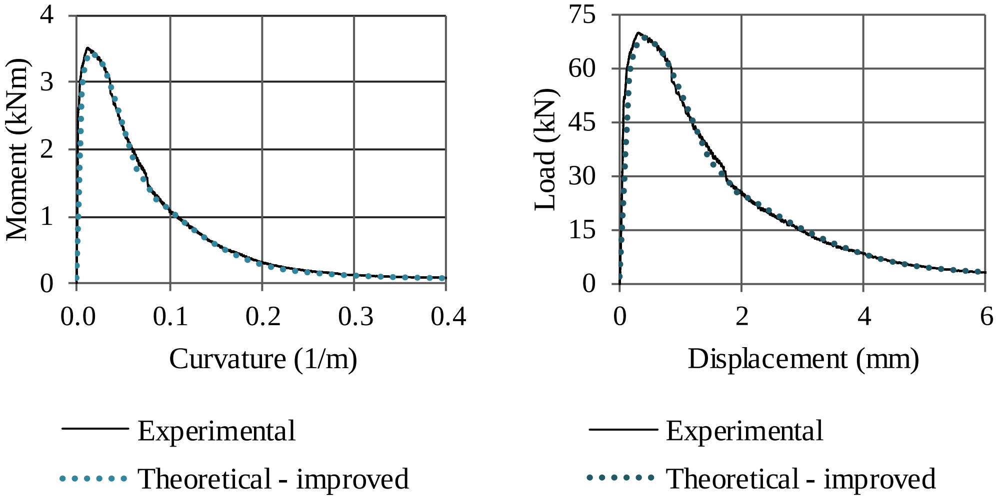

Figure 6-18: Experimental and improved theoretical moment-curvature and load-displacement responses

6.9 SUMMARY

The inverse analysis provided a sufficient stress-strain response that could be used to fit the experimental moment-curvature and load-displacement relationships. The material model was described sufficiently, and the tensile stress-strain properties are considered to be a representation of the material properties that allow accurate modelling. The improved stress-strain response included the initial cracking stress and it better reflected the residual strength due to fibres. This material model can in future be implemented in non-linear finite element analysis to model the behaviour of UHPFRC.

7 CONCLUSIONS AND RECOMMENDATIONS

7.1 CONCLUSIONS

Two of the main objectives of this study were to develop an optimised UHPC matrix, based on optimum particle packing of South African materials and to establish the optimum combined fibre and superplasticiser content for UHPC. The study presents a method to effectively develop optimised UHPFRC by using available South African materials. Working towards an efficient application of binders, superplasticiser and fibres in UHPFRC, the modified Andreasen and Andersen particle packing model and response surface design methodology were utilised. The UHPFRC was appropriately designed, produced and tested. Various changes in mechanical properties resulting from different combinations of steel fibre and superplasticiser contents were investigated. The statistical analysis of the RSM confirms that the designed models can be used to navigate the design space defined by the CCD. The optimum combined fibre and superplasticiser content depend on the required mechanical properties and cost. Using the modified Andreasen and Andersen particle packing model and surface response design methodology, it is possible to efficiently produce a dense UHPFRC with a relatively low binder amount, low fibre content and good workability. This can make UHPFRC more cost-effective and improve the practical application thereof.

One of the main objectives in this study was to develop a material model to determine the tensile stress-strain relationship for UHPFRC. Whereafter the experimental flexural tensile strength results were compared to the theoretically calculated moment-curvature and load-displacement responses. The inverse analysis method used was successful in providing an improved simplified stress-strain response for the UHPFRC. The analysis provided valuable information into the stress-strain, moment-curvature and load-displacement responses of the UHPFRC. Standard material test results were used to theoretically calculate moment-curvature and load-displacement responses and compared to the experimental results obtained. The material model developed can in future be implemented in non-linear finite element analysis to model the behaviour of UHPFRC.

Determining the fresh and mechanical properties of the optimised mix design, which include flowability, compressive strength, tensile strength and modulus of elasticity were one of the secondary objectives of this study. The fresh and mechanical properties of the UHPFRC was established. The concrete can be considered as UHPFRC as the twenty-eight-day compressive strength is greater than 150 MPa. Limited long-term drying shrinkage and creep was observed for the UHPFRC. The state of stress for the splitting tensile strength cylinders is biaxial and this results in the value for the splitting tensile strength being higher than the direct tensile strength (uniaxial tensile strength). The assumption of simple beam-bending theory and linear-elastic stress state to determine the maximum flexural tensile strength (MOR) was assumed even though UHPFRC is a non-linear material and the assumption of linear stress distribution is not valid after cracking. The stress calculated for the flexural tensile strength is higher than the actual value developed in the UHPFRC but allow a comparison between different types of UHPFRC. Therefore, the MOR is also greater than the direct tensile strength.

One of the secondary objectives of this study was to investigate the effect of heat curing on the mechanical properties of UHPFRC. From the results, it can be concluded that heat curing is not recommended when considering the long-term strength development. The predicted strength development (*fib* Model code 2010, 2013) of concrete does not incorporate the detrimental effect of high curing temperatures on long-term strength and therefore overestimate the long-term strengths. The strength estimates for both early and long-term ages can be improved by considering this effect in the strength development functions.

Establishing the effect of specimen size on the compressive and flexural tensile strength of UHPFRC members was one of the secondary objectives of this study. A significant size effect of specimen size on the compressive and flexural LOP of UHPFRC was observed. The assumption of a linear-elastic stress state to determine the flexural tensile strength was assumed even though the stress state in UHPFRC after cracking would be highly nonlinear. The flexural tensile strength value does not reflect the reality but allow a comparison between different types of UHPFRC.

The utilisation of by-products, such as USF and FA, as cement replacement materials makes UHPFRC sustainable, leading to a reduced life-cycle cost. The calculated EE/unit strength and EC/unit strength values for the UHPFRC mixture yield lower values compared to that of the 30 MPa concrete mixture, indicating that the UHPFRC can be used to reduce the environmental footprint of the concrete industry.

7.2 RECOMMENDATIONS FOR FUTURE RESEARCH

The following research aspects should be investigated to provide further insight into the behaviour of UHPFRC:

- The effect of hybrid fibres on the mechanical properties and structural performance of UHPC.
- The effect of various curing regimes namely, air curing, steam curing, conventional water bath curing, heat curing at different temperatures and combinations thereof, on the mechanical properties.
- Establishing an improved maturity function for the prediction of concrete strength development that incorporate the effect of high curing temperatures on long-term strength.
- Early age shrinkage and the effect of self-desiccation should be investigated.
- The effect of different beam geometries and span-to-depth ratios on the flexural tensile strength in order to obtain an optimum beam depth.
- Development of EE and EC values for South African materials.
- Implementation of non-linear finite element analysis to model the behaviour of UHPFRC by using the material model developed.
- Implementation of UHPFRC in thin shells or domes.

8 REFERENCES

Abbas, S., Soliman, A.M. & Nehdi, M.L. (2015). Exploring Mechanical and Durability Properties of Ultra-Hhigh Pperformance Concrete Incorporating Various Steel Fibre Lengths and Dosages. *Construction and Building Materials*, Vol. 75, pp. 429-441.

Abbas, S., Nehdi, M.L. &Saleem, M.A. (2016). Ultra-High Performance Concrete: Mechanical Performance, Durability, Sustainability and Implementation Challenges. *International Journal of Concrete Structures and Materials*, Vol. 10, pp. 271-295.

Afroughsabet, V., Biolzi, L. & Ozbakkaloglu, T. (2016). High-performance fiber-reinforced concrete: a review. *Journal Material Science*, Vol. 51, pp. 6517-6551.

Ahlborn, T.M., Mission, D.L., Peuse, E.J. & Gilbertson, C.G. (2008). Durability and Strength Characteristics of Ultra-High Performance Concrete under Variable Curing Regimes. In *Proceedings of the 2nd International Symposium on Ultra-High-Performance Concrete*, Kassel, Germany, pp. 197-204.

Aïtcin, P. (2000). Cement of yesterday and today- Concrete of tomorrow. *Cement and Concrete Research*, Vol. 30, pp. 1349-1359.

Aldahdooh, M.A.A., Bunnori, N.M. & Johari, M.A.M. (2013). Evaluation of ultra-high-performance-fibre reinforced concrete binder content using the response surface method. *Materials and Design*, Vol. 52, pp. 957-965.

Andreasen A.H.M. & Andersen J. (1930). Über die Beziehungen zwischen Kornabstufungen und Zwischenraum in Produkten aus losen Körnern (miteinigen Experimenten). Kolloid-Zeitschrift, Vol. 50, pp. 217–28.

Aoude, H., Dagenais, F.P., Burrell, R.P. & Saatcioglu, M. (2015). Behaviour of ultra-high performance fibre reinforced concrete columns under blast loading. *International Journal of Impact Engineering*, Vol. 80, pp. 185-202.

Astarlioglu, S. & Krauthammer, T. (2014). Response of normal-strength and ultra-high-performance fibre-reinforced concrete columns to idealized blast loads. *Engineering Structures*, Vol. 61, pp. 1-12.

Bache, H.H. (1981). Densified Cement/Ultra-fine Particle-based Materials. In *Proceedings of the 2nd International Conference on Superplasticizers in Concrete*, Ottawa, Canada, pp. 185-213.

Bayard, O. & Plé, O. (2003). Fracture mechanics of reactive powder concretes: material modelling and experimental investigations. *Engineering Fracture Mechanics*, Vol. 70, pp. 839-851.

Behloul, M. (1996). Les micro-be`tons renforces de fibers. De l'e´prouvevette aux structures, XIVe`mes Journe´es de l'AUGC.

Bhanja, S. & Sengupta, B. (2005). Influence of silica fume on the tensile strength of concrete. *Cement and Concrete Research*, Vol. 35, pp. 743-747.

Binard, J.P. (2017). UHPC: A game-changing material for PCI bridge producers. *PCI Journal*, March-April, pp. 34-46.

Bindiganavile, V., Banthia, N. & Aarup, B. (2002). Impact Response of Ultra-High-Strength Fibre-Reinforced Cement Composite. *ACI Materials Journal*, November-December, pp. 543-548.

Blais, R.Y. & Couture, M. (1999). Precast, Prestressed Pedestrian Bridge – World's First Reactive Powder Concrete Structure. *PCI Journal*, September-October, pp. 60-71.

Bonneau, O., Poulin, C., Dugat, J., Richard, P & Aïtcin, P. (1996). Reactive powder concretes: From theory to practice. Concrete International, Vol. 18, pp. 47-49.

Bonneau, O., Lachemi, M., Dallaire, E., Dugat, J. & Aïtcin, P. (1997). Mechanical properties and durability of two industrial reactive powder concretes. *ACI Materials Journal*, July-August, pp. 286-290.

Bonneau, O., Vernet, C., Moranville, M. & Aïtcin, P. (2000). Characterization of granular packing and percolation threshold of reactive powder concrete. *Cement and Concrete Research*, Vol. 30, pp. 1861-1867.

Bornemann, R. & Faber, S. (2004). UHPC with steel- and non-corroding high-strength polymer fibres under static and cyclic loading. In *Proceedings of the International Symposium on Ultra-High-Performance Concrete*, Kassel, Germany, pp. 673-681.

British Standards. (1999). *BS EN 1015-3:1999, Methods of test for mortar for masonry. Determination of consistence of fresh mortar (by flow table)*. British Standards Institution.

British Standards. (2013). *BS EN 12390-13:2013, Determination of secant modulus of elasticity in compression*. British Standards Institution.

Brouwers, H.J.H., & Radix, H.J. (2005). Self compacting concrete: theoretical and experimental study. *Cement & Concrete. Research*, Vol. 35, pp. 2116–2136.

Brynard, D.J., Hanekom, S.X. & Brynard P.A. (2016). *Introduction to Research*. 3rd edition. Van Schaik, Braamfontein.

Cadoni, E., Forni, D., Bonnet, E. & Bobrusky, S. (2019). Experimental study on direct tensile behaviour of UHPFRC under high strain-rates. *Construction and Building Materials*, Vol. 218, pp. 667-680.

Case, J. & Chilver, A.H. (1971). *Strength of materials and structures*. 2nd Edition. Edward Arnold (Publishers) Limited, London.

Cattaneo S. & Biolzi L. (2009). Assessment of thermal damage in hybrid fiber-reinforced concrete. *Journal of Materials in Civil Engineering*, Vol. 22, pp. 836–845.

Chan, Y. & Chu, S. (2004). Effect of silica fume on steel fibre bond characteristics in reactive powder concrete. *Cement and Concrete Research*, Vol. 34, pp. 1167-1172.

Cheyrezy, M., Maret, V. & Frouin, L. (1995). Microstructural Analysis of RPC (Reactive Powder Concrete). *Cement and Concrete Research*, Vol. 25, pp. 1491-1500.

Collepardi, S., Coppola, L., Troli, R. & Collepardi, M. (1997), Mechanical Properties of Modified Reactive Powder Concrete. *ACI Materials Journal*, Vol. 173, pp. 1-22.

De Larrard, F. (1989). Ultrafine particles for the making of very high strength concretes. *Cement and Concrete Research*, Vol. 19, pp. 161-172.

De Larrard, F. & Sedran, T. (1994). Optimization of Ultra-High-Performance Concrete by use of a packing model. *Cement and Concrete Research*, Vol. 24, pp. 997-1009.

De Larrard, F. & Sedran, T. (2002). Mixture-proportioning of high-performance concrete. *Cement and Concrete Research*, Vol. 32, pp. 1699-1704.

Denneman, E., Kearsley, E.P. & Visser, A.T. (2010). Size-effect in high performance concrete road pavement materials. In G. Van Zijl and W. Boshoff (eds.), *Advances in cement-based materials*. London: CRC Press pp.53-58.

Denneman, E. (2011). Fracture in high performance fibre reinforced concrete pavement materials. PhD Thesis. University of Pretoria, South Africa.

Domone, P. & Illston, J. (2010). *Construction Materials – Their Nature and Behaviour*. 4th Edition. Spon Press, Oxon.

Droll, K. (2004). Influence of additions on ultra high performance concretes – grain size optimisation. In *Proceedings of the International Symposium on Ultra-High-Performance Concrete*, Kassel, Germany, pp. 285-301.

El-Dieb, A.S. (2009). Mechanical, durability and microstructural characteristics of ultra-high-strength self-compacting concrete incorporating steel fibres. *Materials and Design*, Vol. 30, pp. 4286-4292.

Elsaigh, W.A. (2007) Modelling the behaviour of steel fibre reinforced concrete pavements. PhD Thesis. University of Pretoria, South Africa.

European Standard. (2004). *EN 1992-1-1, Eurocode 2: Design of concrete structures – Part 1-1: General rules and rules for buildings*. European Committee for Standardization.

Fehling, E., Bunje, K., Schmidt, M. & Schreiber, W. (2004). UHPC bridge across the River Fulda in Kassel – Conceptual Design Calculations and Invitation to Tender. International Symposium on Ultra High Performance Concrete, Kassel, Germany.

Fehling, E., Schmidt, M., & Stuerwald, S. (Eds.). (2008). Second International Symposium on Ultra High Performance Concrete, Kassel, Germany, pp. 902.

Fennis, S.A.A.M., Walraven, J.C. & Uijl, J. (2009). The use of particle packing models to design ecological concrete. *HERON*, Vol. 54, pp. 185-204.

Fennis, S.A.A.M. & Walraven, J.C. (2012). Using particle packing technology for sustainable concrete mixture design. *HERON*, Vol. 57, pp. 73-101.

FIB (2013). *fib* Model Code for Concrete Structures 2010. *International Federation for Structural Concrete*, Berlin, Ernst & Sohn, Wiley.

Filho, R.D.T., Koenders, E.A.B., Formagini, S. & Fairbairn, E.M.R. (2012). Performance assessment of Ultra High Performance Fibre Reinforced Cementitious Composites in view of sustainability. *Materials and Design*, Vol. 36, pp. 880-888.

Fuller, W.B., & Thompson, S.E. (1907). The laws of proportioning concrete. *Transactions of the American Society of Civil Engineering*, Vol. 33, pp 222–298.

Funk, J.E., & Dinger, D.R. (1994). Predictive Process Control of Crowded Particulate Suspensions, Applied to Ceramic Manufacturing, Kluwer Academic Publishers, Boston, the United States.

Gere, J.M. & Timoshenko, S.P. (1991). *Mechanics of materials*. 3rd SI Edition. Chapman & Hall, United Kingdom.

Ghafari, E., Costa, H. & Júlio, E. (2014). RSM-based model to predict he performance of self-compacting UHPC reinforced with hybrid steel micro-fibres. *Construction and Building Materials*, Vol. 66, pp. 375-383.

Ghafari, E., Bandarabadi, M., Costa, H. & Júlio, E. (2015a). Prediction of Fresh and Hardened State Properties of UHPC: Comparative Study of Statistical Mixture Design and an Artificial Neural Network Model. *Journal of Materials in Civil Engineering*, Vol. 27, pp 1-11.

Ghafari, E., Costa, H. & Júlio, E. (2015b). Statistical mixture design approach for eco-efficient UHPC. *Cement & Concrete Composites*, Vol. 55, pp 17-25.

Ghafari, E., Costa, H. & Júlio, E. (2015c). Critical review on eco-efficient ultra high performance concrete enhanced with nano-materials. *Construction and Building Materials*, Vol. 101, pp. 201-208.

Graybeal, B. & Davis, M. (2008). Cylinder or cube: strength testing of 80 – 200 MPa ultra-high performance fibre-reinforced concrete. *ACI Materials Journal*, Vol. 105, pp 603-609.

Graybeal, B. & Hartmann, J. (2003). Strength and durability of ultra-high performance concrete. *In Concrete Bridge Conference*, pp 20.

Graybeal, B. (2006). Material property characterization of ultra-high performance concrete. *In FHWA-HRT-06-103, U.S. Department of Transportation*, pp 176.

Graybeal, B. (2007). Compressive behaviour of ultra-high-performance fibre-reinforced concrete. *ACI Materials Journal*, Vol. 104, pp 146-152.

Habel, K., Charron, J.P., Braike, S., Hooton, R.D., Gauvreau, P. & Massicotte, B. 2008. Ultra-high-performance fibre reinforced concrete mix design in central Canada. *Canadian Journal of Civil Engineering*, Vol. 35, pp. 217-224.

Habert, G., Denarié, E., Šanja, A. & Rossi, P. (2013). Lowering the global warming impact of ridge rehabilitation by using Ultra High-Performance Fibre Reinforced Concretes. *Cement & Concrete Composites*, Vol. 38, pp. 1-11.

Hammond, G. & Jones, C. (2008). Inventory of carbon and energy (ICE). Vol. 1.6a. University of Bath, United Kingdom.

Hassan, A.M.T., Jones, S.W. & Mahmud, G.H. (2012). Experimental test methods to determine the uniaxial tensile and compressive behaviour of ultra high performance fibre reinforced concrete (UHPFRC). *Construction and Building Materials*, Vol. 37, pp. 874-882.

Heinz, D., Kalde, M., Ludwig, U. &Ruediger, I. (1999). Present State of the Investigation on Damaging Late Ettringite Formation (DLEF) in Motar and Concretes, in Ettringite – the sometimes host of destruction. *ACI International*, Farminton, Hills, Michigan, pp. 1-14.

Heinz, D. & Ludwig, H. (2004) Heat Treatment and the Risk of DEF (Delayed Ettringite Formation) in UHPC. In *Proceedings of the International Symposium on Ultra-High-Performance Concrete*, Kassel, Germany, pp. 717-730.

Hiremath, P.N. & Yaragal, S.C. (2017a). Influence of mixing method, speed and duration on the fresh and hardened properties of reactive powder concrete. *Construction and Building Materials*, Vol. 141, pp. 271-288.

Hiremath, P.N. & Yaragal, S.C. (2017b). Effect of different curing regimes and durations on early strength development of reactive powder concrete. *Construction and Building Materials*, Vol. 154, pp. 72-87.

Hurst, M.K. (2003). *Prestressed Concrete Design.* 2nd edition. E & FN Spon, London.

Hüsken, G. (2010). *A multifunctional design approach for sustainable concrete with application to concrete mass products*. PhD thesis. Eindhoven University of Technology, The Netherlands.

Hwang, J.H., Lee, Deuckhang, L., Kim, K.S., Yun, H.D., Seo, S.Y. & Cho, C.G. (2012). Ductility and Bond Characteristics of Steel Fiber-Reinforced Concrete Members Subjected to Shear. *Journal of Computational and Theoretical Nanoscience*, Vol. 13, pp. 491-494.

Ingo, S., Jurgen, S. & Ollver, M. (2004). Effect of mixing and placement methods on fresh and hardened ultra-high performance concrete. *In Proceeding of Ultra High Performance Concrete*, Kassel, Germany, pp. 575–586.

Japan Society of Civil Engineers. (1984). *JSCE-SF4, Method of tests for flexural strength and flexural toughness of steel fiber reinforced concrete*. Concrete Library of JSCE.

Jun, P., Taek, K., Tae, K. & Wook, K. (2008). Influence of the ingredients on the compressive strength of UHPC as a fundamental study to optimize the mixing proportion. *In Proceedings of* *the 2nd International Symposium on Ultra-High Performance Concrete*, Kassel, Germany, pp.105–112.

Kahanji, C., Ali, F. & Nadjai, A. (2017). Structural performance of ultra-high-performance fibre reinforced concrete beams. *Structural Concrete*, Vol. 18, pp. 249-258.

Kang, S., Lee, Y., Park, Y., & Kim, J. (2010). Tensile fracture properties of an ultra-high performance fiber reinforced concrete (UHPFRC) with steel fibers. *Composite Structures*, Vol. 92, pp. 61–71.

Kang, S., Lee, J., Hong, S. & Moon, J. (2017). Microstructural Investigation of Heat-Treated Ultra-High Performance Concrete for Optimum Production. *Materials Journal*, Vol. 10, pp.1106-1119.

Kazemi, S. & Lubell, A.S. (2012). Influence of Specimen Size and Fibre Content on Mechanical Properties of Ultra-High-Performance Fibre-Reinforced Concrete. *ACI Materials Journal*, November-December, pp. 675-684.

Kim, D.J., Park, S.H., Ryu, G.S. & Koh K.T. (2011) Comparative flexural behavior of Hybrid Ultra High Performance Fiber Reinforced Concrete with different macro fibers. *Construction and Building Materials*, Vol. 25, pp. 4144–4155.

Kim, S., Park, J., Kang, S. & Ryu, G. (2008). Effect of filling method on fibre orientation and dispersion and mechanical properties of UHPC. *In Proceedings of the 2nd International Symposium on Ultra High Performance Concrete*, Kassel, Germany, pp. 185-192.

Küsel, F. (2018). The effect of steel fibres on moment redistribution in high strength reinforced concrete beams. Masters dissertation. University of Pretoria, South Africa.

Li, P.P., Yu, Q.L., Brouwers, H.J.H. & Yu, R. (2016). Fresh behaviour of ultra-high performance concrete. *In Proceedings of the 9th International Concrete Conference, Environment, Efficiency and Economic Challenges for Concrete*, Dundee, Scotland, United Kingdom, pp 635-644.

Li, V.C. & Maalej, M. (1996). *Toughening in cement based composites. Part II: fiber reinforced cementitious composites*. *Cement and Concrete Composites*, Vol. 18, pp. 239–249.

Magureanu, C., Sosa, I., Negrutiu, C. & Heghes, B. (2012). Mechanical properties and durability of ultra-high performance concrete. *ACI Materials Journal*, Vol. 109, pp. 177–183.

Mahmud, G.H., Yang, Z. & Hassan, A.M.T. (2013). Experimental and numerical studies of size effects on Ultra High-Performance Steel Fibre Reinforced Concrete (UHPFRC) beams. *Construction and Building Materials*, Vol. 48, pp. 1027-1034.

Mantel, D.G. (1991). *PPC, The Manufacture, Properties and Applications of Portland Cements, Cement Additives and Blended Cements*. The Penrose Press and Pretoria Portland Cement, Johannesburg.

Mazloom, M., Ramezanianpour, A.A. & Brooks, J.J. (2004). Effect of silica fume on mechanical properties of high-strength concrete. *Cement and Concrete Research*, Vol. 26, pp. 347-357.

Meng, W., Valipour, M. & Khayat., K.H. (2017). Optimization and performance of cost-effective Ultra-High-Performance Concrete. *Materials and Structures*, Vol. 50, pp. 29-45.

Mishra, D.K., Yu, J. & Leung, C.K.Y. (2018). Green Concrete under Normal and Heat Curing with Fly Ash from China and India. *Selected Proceedings of the Thirteenth International Conference on Waste Management and Technology*, pp. 281- 289.

Montgomery, D.C. (2001). Design and Analysis of Experiments. 5th edition, New York, John Wiley & Sons.

Müller, U., Meng, B., Kühne, H., Nemecek, J. & Fontana, P. (2008). Micro texture and mechanical properties of heat treated and autoclaved Ultra High Performance Concrete (UHPC). In *Proceedings of the 2nd International Symposium on Ultra-High-Performance Concrete*, Kassel, Germany, pp. 213-220.

Naaman A.E. (2003). Engineered steel fibers with optimal properties for reinforcement of cement composites. *Journal of Advanced Concrete Technology*, Vol. 1, pp. 241−252.

Neville, A.M. (1995). Properties of concrete. Longman House, Burnt Mil, Harlow, England.

Ngo, D. & Scordelis, A.C. (1967). Finite Element Analysis of Reinforced Concrete Beams. *Journal of American Concrete Institute*, Vol. 64, pp. 152-163.

Nguyen, D.L., Kim, D.J., Ryu, G.S. & Koh, K.T. (2013). Size effect on flexural behaviour of ultra-high-performance hybrid fibre-reinforced concrete. *Composite: Part B*, Vol. 45, pp. 1104-1116.

Okamura, H. & Ozawa, K. (1995). Mix-design for self-compacting concrete. *Concrete Library JSCE*, Vol. 25, pp. 107-120.

Olesen, J.F., Ostergaard, L. & Stang, H. (2006). Nonlinear fracture mechanics and plasticity of the split cylinder test. *Materials and Structures*, Vol. 39, pp. 421-432.

Orgass, M. & Klug, Y. (2004). Fibre Reinforced Ultra-High Strength Concretes. In *Proceedings of the International Symposium on Ultra-High-Performance Concrete*, Kassel, Germany, pp. 637-648.

Park J.J., Kang S.T., Koh K.T. & Kim S.W. (2008). Influence of the ingredients on the compressive strength of UHPC as a fundamental study to optimize the mixing proportion. *Proceedings of the International Symposium on Ultra-High-Performance Concrete, structural materials and engineering series*, Kassel, Germany, pp. 105–12.

Pfeifer, D.W. & Landgren, R. (1982). Energy-efficient accelerated curing of concrete for plant-produced prestressed concrete. *PCI Journal*, March-April, pp. 94-107.

Poon, C.S., Shui, Z.H. & Lam, L. (2004). Compressive behavior of fiber reinforced high-performance concrete subjected to elevated temperatures. *Cement and Concrete Research*, Vol. 34, pp. 2215–2222

Prem, P.R., Bharatkumar, B.H. & Iyer, N.R. (2013). Influence of curing regimes on compressive strength of ultra-high-performance concrete. *Sādhanā,* Vol. 38, No. 6, December, pp. 1421-1431.

Racky, P. (2004). Cost-effectiveness and sustainability of UHPC. *In Proceedings of the International Symposium on UHPC*, Kassel, Germany, pp. 797-805.

Rashid, Y.R. (1968) Ultimate Strength Analysis of Prestressed Concrete Pressure Vessels. *Nuclear Engineering and Design*, Vol. 112, pp. 2628-2645.

Reda, M., Shrive, G. & Gillott, E. (1999). Microstructural investigation of innovative UHPC. *Cement and Concrete Research*, Vol. 29, pp. 323–329.

Reagel, F., & Willis, T. (1931). The effect of dimensions of test specimens on the flexural strength of concrete. *Public roads*, Vol. 12, pp. 37-46.

Richard, P., & Cheyrezy, M. (1994). Reactive powder concretes with high ductility and 200-800 MPa compressive strength. Concrete technology: Past, present and future. *In Proceedings of V. Mohan Malhotra Symposium*, American Concrete Institute, pp. 507-518.

Richard, P., & Cheyrezy, M. (1995). Composition of reactive powder concretes. *Cement and Concrete Research*, Vol. 25, pp. 1501-1511.

Rocco, C., Guinea, G., Plans, J. & Elices, M. (1999). Size effect and boundary conditions in the Brazilian test: theoretical analysis. *Materials and Structures*, Vol. 32, pp. 437-444.

Rossi, P. (2013). Influence of fibre geometry and matrix maturity on the mechanical performance of ultra-high-performance cement-based composites. *Cement and Concrete Composites*, Vol. 37, pp. 246-248.

Roy, D.M., Gouda, G.R. & Bobrowsky, A. (1972). Very High Strength Cement Pastes Prepared by Hot Pressing and Other High Pressure Techniques. *Cement and Concrete Research*, Vol. 2, pp. 349-366.

Savino, V., Lanzoni, L., Tarantino, A.M. & Viviani, M. (2019). An extended model to predict the compressive, tensile and flexural strengths of HPFRC's and UHPFRC's: Definition and experimental validation. *Composite Part B*, Vol. 163, pp. 681-689.

Schmidt, D., Dehn, F. & Urbonas, L. (2004). Fire resistance of ultra-high performance concrete (UHPC) – testing of laboratory samples and columns under load. *In Proceedings of the International Symposium on UHPC*, Kassel, Germany, pp. 703-715.

Schmidt, M., Fehling, E., Teichmann, T., Bunje, K. & Bornemann, R. (2003). Ultra-high-performance concrete: Perspective for the precast concrete industry. *Concrete Precasting Plant Technology*, Vol. 69, pp. 16-29.

Schmidt, M. & Fehling, E. (2005). Ultra-high-performance concrete: research, development and application in Europe. *In 7th International Symposium on Utilization of High Strength High Performance Concrete*, Vol. 1, pp. 51-77.

Schmidt, M., Fehling, E., Glotzbach, C., Frohlich, S. & Piotrowski, S. (Eds.). (2012). *Third International Symposium on UHPC and Nanotechnology for High Performance Construction Materials*, Kassel, Germany, pp. 1036.

Shah, S., & Weiss, W. (1998). Ultra high strength concrete; Looking toward the future. *In ACI Special Proceedings from the Paul Zia Symposium*, Atlanta, GA.

Shi, C., Wu, Z., Xiao, J., Wang, D., Huang, Z. & Fang, Z. (2015). A review on ultra high performance concrete: Part I. Raw materials and mixture design. *Construction and Building Materials*, Vol. 101, pp. 741-751.

Shu-hua, L., Li-hua, L. & Jian-wen, F. (2012). Study on mechanical properties of reactive powder concrete. *Journal of Civil Engineering and Construction*, Vol. 1, pp. 6–11.

Smit, M.S. (2015). *The effect of mixture proportions on the properties of high strength concrete pavements*. Masters dissertation. University of Pretoria, South Africa.

South African National Standard. (2014). *SANS 50450-1:2014, Fly ash for concrete, Part 1: Definitions, specifications and conformity criteria.* SABS Standards Division, Pretoria.

South African National Standard. (2011). *SANS 53263-1:2011, Silica fume for concrete, Part 1: Definitions, requirements and conformity criteria.* SABS Standards Division, Pretoria.

South African National Standard. (2006). *SANS 5862-2:2006, Concrete tests – Consistence of freshly mixed concrete – flow test.* SABS Standards Division, Pretoria.

South African National Standard. (2006). *SANS 5864:2006, Concrete tests - Flexural strength of hardened concrete.* SABS Standards Division, Pretoria.

South African National Standard. (2006). *SANS 6253:2006, Concrete tests – Tensile splitting strength of concrete.* SABS Standards Division, Pretoria.

Steil, T., Karihaloo, B. & Fahling, E. (2004). Effect of casting direction on the mechanical properties of CARDIFRC. *In Proceedings of the International Symposium on Ultra-High Performance Concrete,* Kassel, Germany, pp. 481–493.

Soutsos, M.N., Millard, S. & Karaiskos, K. (2005). Mix design, mechanical properties, and impact resistance of reactive powder concrete (RPC). *In International Workshop on High Performance Fibre-Reinforced Cementitious Composites in Structural Applications,* pp. 549-560.

Soutsos, M.N., Le, T.T. & Lampropoulos, A.P. (2012). Flexural performance of fibre reinforced concrete made with steel and synthetic fibres. *Construction and Building Materials*, Vol. 36, pp. 704-710.

Soutsos, M.N. & Domone, P. (2018). *Construction Materials – Their Nature and Behaviour*. 5th Edition. CRC Press, Taylor & Francis Group, Boca Raton.

Soutsos, M.N. & Kanavaris, F., Hatzitheodorou, A. (2018). Critical analysis of strength estimates from maturity functions. *Case studies in Construction Materials*, Vol. 9.

Soutsos, M.N. & Kanavaris, F. (2018). The modified nurse-saul (MNS) maturity function for improved strength estimates at elevated curing temperatures. *Case studies in Construction Materials*.

Talebinejad, I., Iranmanesh, A., Bassam, S. & Shekarchizadeh, M. (2004). Optimizing mix proportions of normal weight reactive powder concrete with strengths of 200–350 MPa. *In Proceedings of the International Symposium on UHPC*, Kassel, Germany, pp. 133–141.

Tang, C. (2004). High performance concrete-past, present and future. *In Proceedings of the International Symposium on UHPC*, Kassel, Germany, pp. 3-9.

Tracey, S.L., Boyd, S.R. & Connolly, J.D. (2004). Effect of curing temperature and cement chemistry on the potential for concrete expansion due to DEF. *PCI Journal*, January – February, pp. 46-57.

Tue, N., Orgass, M. & Ma, J. (2008). Influence of addition method of superplasticizer on the properties of fresh UHPC. *In Proceedings of the 2nd International Symposium on Ultra-High Performance Concrete*, Kassel, Germany, pp. 93–100.

UNSTATS. (2010). Greenhouse Gas Emissions by Sector (Absolute values). United Nation Statistical Division. Springer.

Van Der Putten, J., Dils, J., Minne, P., Boel, V. & De Schutter, G. (2017). Determination of packing profiles for the verification of the compressible packing model in case of UHPC pastes. *Materials and Structures*, Vol. 50, pp. 118-131.

Vatannia, S. (2018). *Development of practical and economical Ultra High Performance Fibre Reinforced Concrete For Prestressed Beams*. PhD Thesis. University of Pretoria, South Africa.

Vernet, P. (2004). Ultra-durable concretes: Structure at the micro- and nano-scale. *Material Research Society*, 29(5), 324–327.

Vicenzino, E., Culham, G., Perry, V.H., Zakariasen, D. & Chow, T.S. (2005). First use of UHPFRC in think precast concrete roof shell for Canadian LRT station. *PCI Journal*, September-October, pp. 50-67.

Vollpracht, A., Soutsos, M. & Kanavaris, F. (2018). Strength development of GGBS and fly ash concretes and applicability of fib model code's maturity function – A critical review. *Construction and Building Materials*, Vol. 162, pp. 830-846.

Wang, W., Liu, J., Agostini, F., Davy, C., Skoczylas, F. & Corvez, D. (2014). Durability of an ultra high performance fiber reinforced concrete (UHPFRC) under progressive aging. *Cement and Concrete Research*, Vol. 55, pp. 1–13.

Wang, D., Shi, C., Wu, Z., Xiao, J., Huang, Z., & Fang, Z. (2015). A review on ultra high performance concrete: Part II. Hydration, microstructure and properties. *Construction and Building Materials*, Vol. 96, pp. 368–377.

Wille, K., Naaman, A.E. & Parra-Montesinos, G.J. (2011a). Ultra-High-Performance Concrete with Compressive Strength Exceeding 150 MPa (22 ksi): A Simpler Way. *ACI Materials Journal,* January-February, pp. 46-54.

Wille, K., Naaman, A.E. & El-Tawil, S. (2011b). Optimizing Ultra-High-Performance Fibre-Reinforced Concrete. *Concrete International*, September, pp. 35-41.

Wille, K., Naaman, A.E., El-Tawil, S. & Parra-Montesinos, G.J. (2012). Ultra-high-performance concrete and fiber reinforced concrete: achieving strength and ductility without heat curing. *Materials and Structures*, Vol. 45, pp. 309-324.

Wille, K., Tue, N.V. & Parra-Montesinos, G.J. (2014). Fiber distribution and orientation in UHP-FRC beams and their effect on backward anaysis. *Materials and Structures*, Vol. 47, pp. 1825-1838.

Wille, K. & Boisvert-Cotulio, C. (2015). Material efficiency in the design of ultra-high-performance concrete. *Construction and Building Materials*, Vol. 86, pp. 33-43.

Yang, I., Joh, C. & Kim, B. (2010). Structural behaviour of ultra-high performance concrete beams subjected to bending. *Engineering Structures*, Vol. 32, pp. 3478–3487.

Yang, K.H., Jung, Y.B., Cho, M.S. & Tae, S.H. (2015). Effect of supplementary cementitious materials on reduction of CO_2 emissions from concrete. *Journal of Cleaner Production*, Vol. 103, pp, 774-783.

Yang, K.H., Moon, G.D. & Jeon, Y.S. (2016). Implementing ternary supplementary cementing binder for reduction of the heat of hydration of concrete. *Journal of Cleaner Production*, Vol. 112, pp. 845-852.

Yang S.L., Millard S.G., Soutsos M.N., Barnett S.J. & Le T.T. (2009). Influence of aggregate and curing regime on the mechanical properties of ultra-high performance fibre reinforced concrete (UHPFRC). *Construction and Building Materials*, Vol. 23, pp. 2291–2298.

Yazici, H. (2006). The effect of curing conditions on compressive strength of ultra-high strength concrete with high volume mineral admixtures. *Building and Environment*, Vol. 45, pp. 2083-2089.

Yoo, D.Y., Kang, S.T., Lee, J.H. & Yoon, Y.S. (2013). Effect of shrinkage reducing admixture on tensile and flexural behaviors of UHPFRC considering fiber distribution characteristics. *Cement and Concrete Research*, Vol. 54, pp. 180-190.

Yoo, D.Y. & Yoon, Y.S. (2016). A review on structural Behaviour, Design and Application of Ultra-High-Performance Fibre-Reinforced Concrete. *International Journal of Concrete Structures and Materials*, Vol. 10, pp. 125-142.

Yoo, D.Y., Kim, S. & Kim, M. (2018). Comparative shrinkage behaviour of ultra-high-performance fibre-reinforced concrete under ambient and heat curing conditions. *Construction and Building Materials*, Vol. 162, pp. 406-419.

Yu, R., Séesz, P. & Brouwers, H.J.H. (2014). Mix design and properties assessment of Ultra-High-Performance Fibre Reinforced Concrete. *Cement and Concrete Research*, Vol. 56, pp. 29-39.

Yu, R., Spiesz, P., & Brouwers, H.J.H. (2015a). Development of an eco-friendly Ultra-High-Performance Concrete (UHPC) with efficient cement and mineral admixtures uses. *Cement & Concrete Composites*, Vol. 55, pp. 383-394.

Yu, R., Spiesz, P., & Brouwers, H.J.H. (2015b). Development of Ultra-High-Performance Fibre Reinforced Concrete: Towards an efficient utilization of binders and fibres. *Construction and Building Materials*, Vol. 79, pp. 273-282.

Yu, R., Song, Q., Wang, X., Zhang, Z., Shui, Z. & Brouwers, H.J.H. (2017). Sustainable development of Ultra-High-Performance Fibre Reinforced Concrete: Towards to an optimized concrete matrix and efficient fibre application. *Journal of Cleaner Production*, Vol. 162, pp. 220-223.

Yudenfreund, M., Odler, I. & Brunauer, S. (1972a). Hardened Portland Cement Pastes of Low Porosity I. Materials and Experimental Methods. *Cement and Concrete Research*, Vol.2, pp. 313-330.

Yudenfreund, M., Hanna, K.M. & Skalny, J. (1972b). Hardened Portland Cement Pastes of Low Porosity V. Compressive strength. *Cement and Concrete Research*, Vol.2, pp. 731-743.

Zain, M.F.M., Safiuddin, Md. & Mahmud, H. Development of high performance concrete using silica fume at relatively high water-binder ratios. *Cement and Concrete Research*, Vol. 30, pp. 1501-1505.

Zheng, H. (2009). Concrete for Sustainability. SCCT *Annual Concrete Seminars*. Standing Committee on Concrete Technology (SCCT), The Government of the Hong Kong SAR.

Zhou, B. & Uchida, Y. (2017). Influence of flowability, casting time and formwork geometry on fibre orientation and mechanical properties of UHPFRC. *Cement and Concrete Research*, Vol. 95, pp. 164-177.

APPENDIX A

LOAD-DISPLACEMENT CURVES FOR THE MODIFIED MOR BEAMS

The typical load-displacement curves for the modified MOR beams are illustrated below.

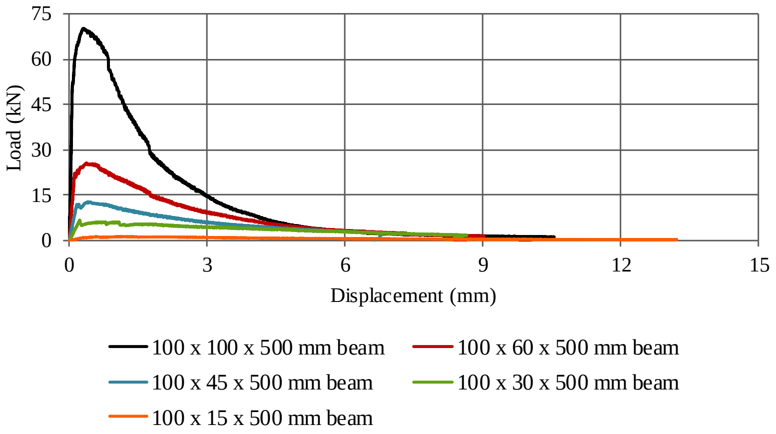

Figure A-1: Specimens size effect

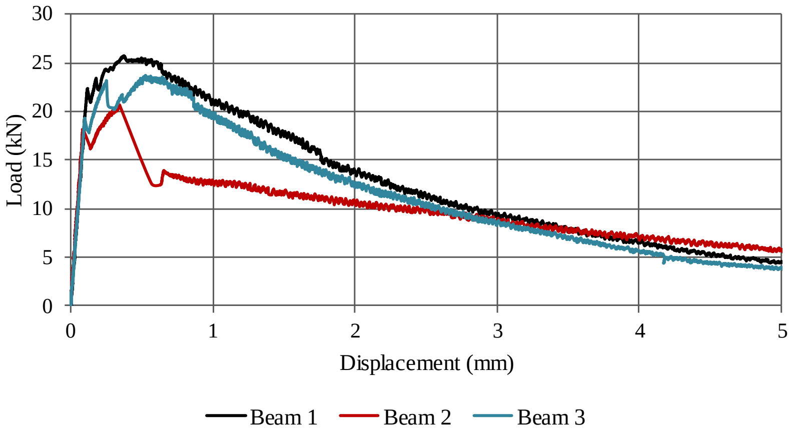

Figure A-2: 100 x 60 x 500 mm beams

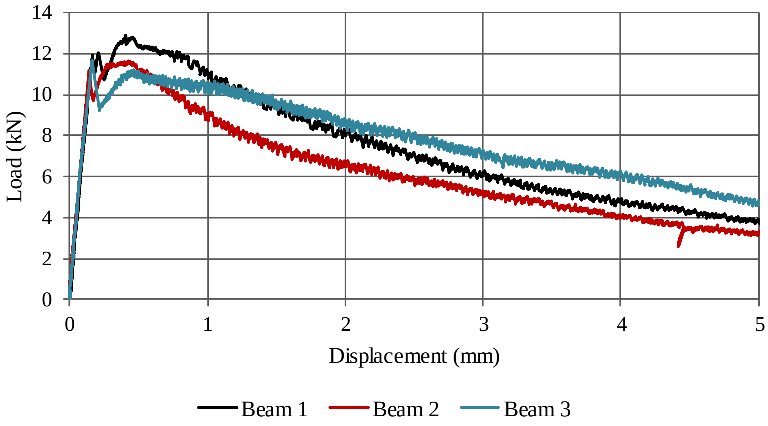

Figure A-3: 100 x 45 x 500 mm beams

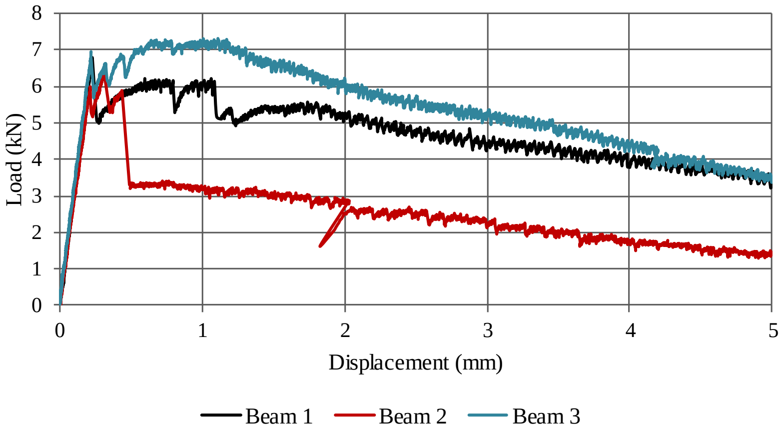

Figure A-4: 100 x 30 x 500 mm beams

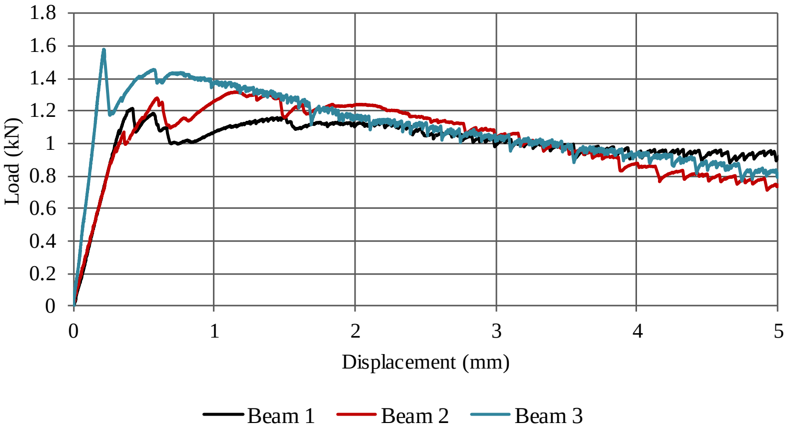

Figure A-5: 100 x 15 x 500 mm beam